

INORGANIC COLLOIDAL NANOCRYSTALS: SYNTHESIS AND BIOAPPLICATIONS

By

HUIMENG WU

A DISSERTATION PRESENTED TO THE GRADUATE SCHOOL
OF THE UNIVERSITY OF FLORIDA IN PARTIAL FULFILLMENT
OF THE REQUIREMENTS FOR THE DEGREE OF
DOCTOR OF PHILOSOPHY

UNIVERSITY OF FLORIDA

2008

© 2008 Huimeng Wu

To my husband, Xiaoyong Zhao; my Daughter, Ashley Zhao; and my parents.

ACKNOWLEDGMENTS

I would first like to thank my adviser, Dr. Charles Y. Cao for providing interesting and important projects, encouraging me to continue the project when things didnot work so well. I would also like to thank my committee members (Prof. Charles Martin, Prof. Weihong Tan, Prof. Ben Smith, Prof. Paul Holloway and Prof. Ronald Castellano) for helping me apply awards and fellowships. Especially I am grateful to Prof. Weihong Tan for allowing me to work in his group before I officially started my Ph.D. training here.

For the material characterization, I am thankful to Dr. Kathryn Williams for the thermogravimetry analysis (TGA) and many other instruments and help revising my dissertation. Dr. Williams also helped me apply for the Lockhart Dissertation Fellowship. Also I would like to thank Ms. Kerry Siebein in the Major Analytical Instrumentation Center (MAIC) for HRTEM measurements. I appreciate valuable help from my colleagues in Prof. Cao's group. I especially thank Dr. Jiaqi Zhuang for helpful discussions.

Finally, I want to thank my husband for his encouragement and support. I want to deeply and sincerely express my appreciation to my parents for taking care of my daughter and letting me have more time to work on the projects.

TABLE OF CONTENTS

	<u>page</u>
ACKNOWLEDGMENTS	4
LIST OF TABLES	8
LIST OF FIGURES	9
ABSTRACT	13
CHAPTER	
1 INTRODUCTION	15
1.1 Synthetic Strategies	17
1.2 Properties of NCs	22
1.2.1 Optical and Electronic Properties	23
1.2.2 Magnetic Properties	27
1.2.3 Thermal Properties	28
1.2.4 Catalytic Properties	29
1.2.5 Mechanical Properties	29
1.3 Bio-Applications of NCs	30
1.3.1 Fluorescent Detection	30
1.3.2 Colorimetric Detection	31
1.3.3 Surface Enhanced Raman Scattering (SERS)	32
1.3.4 Summary of the Present Research	32
2 GENERAL SYNTHESIS AND CHARACTERIZATION OF NANOCRYSTALS	41
2.1 Synthesis of Nanocrystals	41
2.1.1 Semiconductor Nanocrystals	41
2.1.2 Metal Nanocrystals	43
2.1.3 Metal Oxide Nanocrystals	45
2.2 Characterization of Nanocrystals	46
2.2.1 Transmission Electron Microscopy (TEM)	46
2.2.2 Powder X-Ray Diffraction (XRD)	48
2.2.3 Dynamic Light Scattering (DLS)	49
3 SYNTHESIS OF URANIUM-DIOXIDE NANOCRYSTALS	56
3.1 Introduction	56
3.2 Experimental Section	56
3.2.1 Chemicals	56
3.2.2 Synthesis of Spherical Uranium-oxide Nanocrystals	57
3.2.3 Synthesis of Octahedral UO ₂ NCs by a Multiple-injection Method	58

3.2.4	The Effect of Additional Mixture of OA and OAm with a Molar Ratio of 1:1	58
3.2.5	The Effect of Water.....	58
3.2.6	The Amide Effect.....	59
3.2.6.1	Syntheses of Amides.....	59
3.2.7	Characterization of UO ₂ NCs.....	60
3.2.7.1	XRD Measurements of UO ₂ NCs.....	60
3.2.7.2	IR Measurements.....	61
3.2.7.3	¹ H-NMR Measurements.....	61
3.2.7.4	TEM Measurements.....	61
3.3	Results and Discussion.....	61
3.3.1	Synthesis and Characterization of UO ₂ NCs.....	61
3.3.2	Size Control of UO ₂ Nanocrystals.....	62
3.3.3	Shape Control of UO ₂ Nanocrystals.....	63
3.3.3.1	Multiple-injection.....	63
3.3.3.2	Ligand Effect.....	64
3.3.3.3	Self-assembly of UO ₂ NCs.....	64
3.3.3	Mechanistic Study of UO ₂ NC Formation.....	65
4	WATER-SOLUBLE NANOCRYSTALS THROUGH DUAL-INTERACTION LIGANDS.....	78
4.1	Introduction.....	78
4.2	Experimental Section.....	80
4.2.1	Chemicals.....	80
4.2.2	Synthesis of Tween-derivatives (TDs).....	81
4.2.2.1	Dihydropolipoic Acid-functionalized Tweens (TD _N -L).....	81
4.2.2.2	Dopamine-functionalized Tweens (TD _N -D).....	83
4.2.2.3	Carboxyl-group-functionalized TD ₂₀ -L (TD ₂₀ -LC).....	86
4.2.3	Gold, Fe ₃ O ₄ and CdSe/ZnS Nanocrystal Synthesis.....	87
4.2.4	Preparation of TD-capped Water-soluble NCs.....	88
4.2.5	Antibody-functionalized CdSe/ZnS Nanocrystals.....	88
4.2.6	Immunoassay Tests.....	89
4.2.7	Stability Tests.....	90
4.2.8	Other Measurements.....	90
4.2.8.1	¹ H-NMR Measurements.....	90
4.2.8.2	Determination of Fluorescence Quantum Yields (QY).....	90
4.2.8.3	DLS Measurements.....	91
4.2.8.4	TEM Measurements.....	91
4.3	Results and Discussion.....	91
4.4	Conclusion.....	95
5	GOLD NANOCRYSTAL-BASED ASSAY FOR THE DETECTION OF β -GALACTOSIDASE.....	106
5.1	Introduction.....	106
5.2	Experimental Section.....	108

5.2.1	Chemicals.....	108
5.2.2	Synthesis of LT β -gal.....	108
5.2.3	Detection of β -galactosidase	111
5.2.4	Measurements	112
5.2.4.1	¹ H-NMR Measurements	112
5.2.4.2	UV/Vis Spectra.....	112
5.2.4.3	DLS Measurements	112
5.2.4.4	TEM Measurements.....	112
5.3	Results and Discussion.....	112
6	SYNTHESIS OF HYBRID NANOCRYSTALS	118
6.1	Introduction.....	118
6.2	Experimental Section	119
6.2.1	Chemicals.....	119
6.2.2	Synthesis of FePt Nanocrystals.....	120
6.2.3	Synthesis of UO ₂ Nanocrystals.....	120
6.2.5	Synthesis of Corn-seed-shaped FePt/In ₂ O ₃ Hybrid Nanocrystals.....	121
6.2.6	Synthesis of Peanut-shaped UO ₂ /In ₂ O ₃ Hybrid Nanocrystals.	121
6.2.7	TEM Measurements	121
6.3	Results and Discussion.....	122
6.3.1	Synthesis and Characterization of FePt/In ₂ O ₃ Hybrid Nanocrystals	122
6.3.2	Synthesis and Characterization of UO ₂ /In ₂ O ₃ Hybrid Nanocrystals	124
7	CONCLUSIONS	131
7.1	Summary of This Research.....	131
7.2	Perspectives.....	132
APPENDIX		
A	XDR MEASUREMENT OF URANIUMOXIDE NANOCRYSTALS.....	134
B	¹ H-NMR SPECTRUM.....	135
C	MS SPECTRUM OF LT β -GAL.....	146
LIST OF REFERENCES.....		147
BIOGRAPHICAL SKETCH		157

LIST OF TABLES

<u>Table</u>		<u>page</u>
1-1	Electron and hole masses, exciton Bohr radii and band-gap energies for various semiconductor materials	39
4-1	Stability test of CdSe/ZnS NCs capped with different ligands.....	105

LIST OF FIGURES

<u>Figure</u>	<u>page</u>
1-1 Structure of a typical nanocrystal: the crystalline inorganic core, capped by organic ligands.....	35
1-2 LaMer curve.....	35
1-3 Schematic illustration of the electronic structure.....	36
1-4 Idealized density of states for one band of a semiconductor structure of “3d”, “2d”, “1d”, and “0d” materials.....	36
1-5 The color of CdSe NCs depends on NC sizes.....	37
1-6 UV/Vis absorption spectra of different size Au NCs: 9 nm, 22 nm, 48 nm and 99 nm Au NCs in water.....	38
1-7 The emission wavelengths from representative QD core materials and representative areas of biological interest.....	38
1-8 <i>In vivo</i> cancer targeting and imaging of QD-antibody conjugates in living mice.....	39
1-9 The target DNA induces aggregation of oligonucleotide-modified Au NCs.....	39
1-10 Scheme for the SERS detection of DNA fragments.....	40
2-1 Injection method for synthesis of monodisperse semiconductor NCs.....	51
2-2 TEM images of polyhedral metal nanocrystals.....	52
2-3 The electron-optical system of a TEM.....	53
2-4 The relationship of the spacing (R) between diffraction spots and camera length (L).....	54
2-5 The TEM images of star-shaped Fe ₃ O ₄ NCs.....	55
3-1 Characterization of UO ₂ NCs.....	70
3-2 TEM images of UO ₂ NCs.....	71
3-3 Multiple-injection method for preparing octahedral UO ₂ nanocrystals.....	72
3-4 The particle growth with multiple-injection of the precursor solutions.....	72
3-5 A typical TEM image of branched UO ₂ NCs. The inset is the HRTEM image.....	73
3-6 TEM images of self-assembled UO ₂ nanocrystals.....	73

3-7	TEM images of assemblies of 9.1 nm octahedral UO ₂ nanocrystals.....	74
3-8	IR and ¹ H-NMR spectra of reaction mixture.....	75
3-9	TEM measurement of the water effect.....	76
3-10	IR spectra of purified UO ₂ NCs and OOA	76
3-11	TEM measurement of the amide effect.....	77
4-1	Schematic illustration of the Tween-derivatives (TDs) dual interaction.....	97
4-2	Synthesis of dual-interaction TD ligands.....	98
4-3	¹ H-NMR of compound TD ₂₀ -a.....	99
4-4	¹ H-NMR of compound TD ₂₀ -L.....	99
4-5	DLS data for TD ₂₀ -L-functionalized 6.6-nm Au NCs from five parallel thermal-stability-test experiments.	100
4-6	TEM images of hydrophobic NCs	100
4-7	Gas-chromatography mass spectrometry (GC-MS).....	101
4-8	UV-Vis spectra for the stability tests of TD ₂₀ -L-functionalized Au NCs.....	102
4-9	Stability tests of TD ₂₀ -L-functionalized 6.6-nm Au NCs monitored with DLS and UV-Vis spectra.....	102
4-10	TEM images of TD ₂₀ -D-capped Fe ₃ O ₄ NCs from aqueous solutions at pH 7 and pH 2 for 2h.....	103
4-11	TD ₂₀ -L capped CdSe/ZnS NCs with different sizes in aqueous solution.....	103
4-12	Stability tests of TD _N -L-functionalized 5.6-nm CdSe/ZnS NCs as a function of the fatty-acid chain on these TD ligands	104
4-13	Immunofluorescence tests of NS5A-containing FCA1 cells using TD-functionalized CdSe/ZnS core/shell nanocrystal QD.	104
5-1	β -galactosidase assay based on Au-NCs.....	116
5-2	Detection of β -galactosidase.....	116
5-3	Kinetics studies of the enzyme-induced Au-NC aggregation.....	117
6-1	TEM images of FePt seeds and the nanocrystals extracted from the FePt reaction mixture before the injection of the indium stock solution	126

6-2	STEM images of FePt/In ₂ O ₃ hybrid nanocrystals	126
6-3	TEM image of the FePt-Iron oxide core-shell NCs obtained from the control experiment.....	127
6-4	HRTEM studies of an individual FePt/In ₂ O ₃ hybrid nanocrystal.....	128
6-5	TEM images of UO ₂ /In ₂ O ₃ hybrid nanocrystals.....	129
6-6	HRTEM images of an individual UO ₂ /In ₂ O ₃ hybrid nanocrystal.....	130
A-1	XRD measurement of UO ₂ Nanocrystals.	134
B-1	¹ H-NMR of compound TD ₂₀ -a.....	135
B-2	¹ H-NMR of compound TD ₂₀ -L.....	135
B-3	¹ H-NMR of compound TD ₄₀ -a.....	136
B-4	¹ H-NMR of compound TD ₄₀ -L.....	136
B-5	¹ H-NMR of compound TD ₆₀ -a.....	137
B-6	¹ H-NMR of compound TD ₆₀ -L.....	137
B-7	¹ H-NMR of compound TD ₈₀ -a.....	138
B-8	¹ H-NMR of compound TD ₈₀ -L.....	138
B-9	¹ H-NMR of compound TD ₂₀ -b	139
B-10	¹ H-NMR of compound TD ₂₀ -c.....	139
B-11	¹ H-NMR of compound TD ₂₀ -D	140
B-12	¹ H-NMR of compound TD ₄₀ -b	140
B-13	¹ H-NMR of compound TD ₄₀ -c.....	141
B-14	¹ H-NMR of compound TD ₄₀ -D	141
B-15	¹ H-NMR of compound TD ₆₀ -b	142
B-16	¹ H-NMR of compound TD ₆₀ -c.....	142
B-17	¹ H-NMR of compound TD ₆₀ -D	143
B-18	¹ H-NMR of compound TD ₈₀ -b	143
B-19	¹ H-NMR of compound TD ₈₀ -c.....	144

B-20	¹ H-NMR of compound TD ₈₀ -D	144
B-21	¹ H-NMR of compound TD ₂₀ -e.....	145
B-22	¹ H-NMR of compound TD ₂₀ -LC	145
C-1	MS spectrum of LTβ-gal.	146
LIST OF REFERENCES		147

Abstract of Dissertation Presented to the Graduate School
of the University of Florida in Partial Fulfillment of the
Requirements for the Degree of Doctor of Philosophy

INORGANIC COLLOIDAL NANOCRYSTALS: SYNTHESIS AND
BIOAPPLICATIONS

By

Huimeng Wu

December 2008

Chair: Charles Y. Cao
Major: Chemistry

Nanocrystals (NCs) are very small particles, which contain from a few hundred to thousands of atoms depending on the size of NCs. Because of their special properties compared with the bulk materials, NCs have found many promising applications in areas, such as biomedical diagnosis, catalysis, plasmonics, high-density data storage and solar energy conversion. This dissertation presents studies on the syntheses of metal oxide NCs and hybrid NCs, the surface functionalization of NCs by dual-interaction ligands, and gold-NC-based assay for the detection of β -galactosidase.

Monodisperse colloidal uranium dioxide NCs (UO₂ NCs) were synthesized by decomposition of uranyl acetylacetonate. By changing the amount of added surfactant, the sizes of the NCs could vary from 2 ~ 8 nm. Mechanistic studies of the formation of UO₂ NCs showed that the condensation product (amide) of oleic acid and oleylamine plays an important role in controlling the particle size.

Normally, high-quality NCs are synthesized in organic phase, but most of NC-based bio-applications require water-soluble NCs. To convert these hydrophobic NCs to hydrophilic particles, surface modification is employed. Here dual interaction ligands based on the Tween-derivatives (TDs) were synthesized. Stability tests on TD-capped NCs showed that these dual

interaction ligands can significantly increase the stability of NCs compared to single interaction ligands. Further, These TD-capped QDs were further tested as fluorescent labels to detect virus-protein expression in cells.

To exploit bio-applications of nanocrystals, gold nanocrystal-based assay to detect enzyme activity was designed. The optical properties of Au-NCs are not only dependent on the particle sizes and shapes, but also the distances between the particles. Here, Lipoic acid-tyramine- β -galactopyranosyl (LT β -gal) was synthesized, as ligands, to cap Au-NCs; and the resultant LT β -gal-capped Au-NCs could disperse in water. After the hydrolysis of the ligands with β -galactosidase, these Au-NCs become to aggregate, which exhibit a red-shift in the absorption spectrum of the Au-NC suspension. The detection of β -galactosidase was further studies by varying the amounts of β -galactosidase.

Hybrid nanocrystals (HNCs) are attractive candidates for advanced nanomaterials because they contain two or more different nanoscale functionalities, which are expected to possess novel physical and chemical properties. Two kinds of heterodimers (FePt/In₂O₃ and UO₂/In₂O₃) were prepared using a similar procedure and the synthesized HNCs exhibited different shapes. The studies of high-resolution transmission electron microscopy (HRTEM) indicate that the shapes of these two dimers were controlled by the interfacial structures. The amorphous iron oxide layers on the FePt NC surfaces act as glue to interconnect the FePt with the indium oxide parts and led to a core-seed-shaped heterodimer. Using completely crystalline UO₂ NCs as seeds resulted in a peanut-shaped HNC.

CHAPTER 1 INTRODUCTION

Nanoscience and technology, which are among the most exciting research areas in modern science, involve studies of matter at the nanoscale level to discover new properties and applications. Nanocrystals (NCs), which are important building blocks for the development of nanoscience and technology, are very small particles (1 nm~100 nm), which contain from a few hundred atoms to thousands of atoms depending on the particle size. The surfaces of NCs are usually capped by organic or inorganic molecules to avoid aggregation and to stabilize NCs in solvents (Figure 1-1).

The crystal structures of NCs are the same as those of the corresponding bulk materials, but the nano-sized particles exhibit special properties, including unique optical, magnetic, catalytic, biological and mechanical properties. For example, semiconductor NCs show size-dependent absorption and emission spectra because of quantum confinement effects.^[1,2] Noble-metal NC solutions exhibit different colors, depending on their sizes and shapes, due to surface plasmon polaritons.^[3] Magnetic NCs show size-dependent magnetization transition-temperatures, and Coercivity (H_c) and the remanence to saturation magnetization ratio (M_r/M_s) are also related to particle size. Tetrahedral platinum NCs with high-index facets exhibit enhanced catalytic activity (up to 400%) compared to equivalent Pt surface areas for electro-oxidation of small organic fuels, such as formic acid and ethanol.^[4] CdS semiconductor nanoparticles, enfolded by the chaperonin proteins GroEL and *T.th* cpn are high thermal and chemical stability in aqueous media and can be readily released from the protein cavities by the action of ATP, analogous to the biological function of the chaperonins.^[5] Gold-nanowires exhibit a Young's modulus which is essentially independent of diameter, whereas the yield strength is largest for the smallest diameter wires, with strengths up to 100 times that of bulk materials.^[6]

The investigation of these new properties and applications is important for both the understanding of these materials at the fundamental level and the development of novel techniques and applications, in areas such as biological labeling,^[2,7-10] solar energy,^[11-13] LED development,^[14-18] catalyzing,^[19,20] and high-density data storage.^[21] However, these promising applications can not be fully realized until existing fundamental questions are answered.

First, methods must be developed to synthesize high-quality NCs on a large scale with controlled sizes and shapes. To date, the most successful and widely used method to synthesize nanocrystals relies on rapid precursor injection.^[22] Unfortunately, due to rapid injection and reaction kinetics, nanocrystal formation is rather like ‘black magic’ with the nanocrystal size, size distribution, and shape being very sensitive to subtle differences in the injection process (injection time, speed, etc). Furthermore, it is difficult to scale up the method for nanocrystal synthesis in large quantities. Therefore, there is a need to develop easily controllable methods for nanocrystal synthesis. Studies of the mechanisms of nanocrystal nucleation and growth can provide better understanding of how particle size and shape can be controlled.

Second, surface engineering of nanocrystals is key to the nanocrystal-based applications. New functionalization methods need to be designed for various applications. Previous research indicates that the properties are very sensitive to the surfaces of NCs. Modification of nanocrystal surfaces directly improves their stability and solubility, as well as their chemical and physical properties. Since NCs have exhibited a number of potential bioapplications, one goal of surface engineering is to achieve robust and biocompatible nanocrystals with special properties.

The following portion of this introduction includes a brief description of synthesis strategies, size-dependent properties and potential applications of NCs, as well as a brief summary of the present research work.

1.1 Synthetic Strategies

Based on the reaction media, preparation of nanocrystals can be classified as gas phase, liquid phase or solid phase syntheses. Solid-phase syntheses have been employed to alter the crystalline structures of NCs^[23] or create hollow structured NCs^[24] by annealing NCs at high temperature. Most NCs have been synthesized in either the gas phase or liquid phases.

Gas-phase synthesis is a well-known chemical manufacturing technique for ultra-thin coating of particles, such as carbon black and pyrogenic silica, using flame, plasma, or laser reactors.^[25] The products of gas-phase syntheses usually are bare particles with a wide size distribution. Since no ligands stabilize the particles, these particles tend to form aggregates in solution. A chemical vapor deposition (CVD) method has been successfully employed for preparation of multiwall or single-wall carbon nanotubes (MWNTs)^[26] Recently, gas phase syntheses have been exploited for preparation of various nanomaterials, such as metal^[27,28], metal oxide^[29] and semiconductor NCs,^[30] and FeSi nanowires.^[31] Gas phase synthesis of NCs provides a high throughput method for preparation of nanomaterials, but further investigation need to be performed to improve size distribution, crystallinity, and surface passivation of these nanomaterials.

The advances in quantum dot science and technology have been made possible by liquid-phase synthetic methods, which allow investigation of the special optical properties of NCs and their potential biomedical applications, such as fluorescent labels^[2] and cell trackers.^[32] Liquid phase synthesis can be performed within structured media acting as templates, such as reverse micelles,^[33] microemulsions^[34,35] and nanoporous membranes^[36]. Membrane template synthesis of nanomaterials was developed by Martin's group. Depending on the material and the chemistry of the membrane, the resulting nanomaterial may be either solid (nanowires) or hollow (nanotubes). Martin's group has also investigated applications of nanotube-containing

membranes for separations of DNA, proteins and drugs.^[37,38] Template-free syntheses have been performed in both aqueous and organic solvents for preparation of metal,^[39] metal oxide^[40] and semiconductor NCs,^[41] such as Au NCs,^[42,43] Ag nanoprisms^[44] and CdTe nanowires.^[41,45] Aqueous-phase syntheses are usually simple, fast and relatively inexpensive, but few high-quality NCs have been reported by these methods.

Recently, great progress has been made in organic-phase synthesis for colloidal inorganic nanocrystals.^[46] Numerous monodisperse, size- and shape-controllable nanocrystals have been synthesized using organic-phases.^[47,48] Although a general approach to the fabrication in a precisely controlled manner is not available yet, it is widely accepted that the presence of organic surfactants can be key to determining the sizes and shapes of the NCs. Since most of the present research has utilized organic-phase syntheses, these methods will be described in greater detail.

Organic-phase nanocrystal synthesis involves three important steps: nucleation, growth, and passivation. Synthesis of high-quality colloidal nanocrystals with different sizes and shapes can be achieved by manipulating these three steps. LaMer's curve is well-known for describing the formation of precipitates, and it can also be used to understand the formation of NCs from homogeneous, supersaturated media,^[49] as shown in Figure 1-2.

In a typical synthesis, precursors, ligands and solvents are heated to a certain temperature, at which the precursors react with each other or with the ligands to form active atoms or molecules, called monomers. At the very beginning, the reaction medium is saturated with the monomers without the formation of any particles (i.e., nuclei). When the concentration exceeds a critical limit, called the critical limiting super-saturation, nucleation occurs. The nuclei start to grow and consume the active monomers, thereby depleting the concentration of monomers. When the concentration of active monomer decreases, no further nucleation occurs and the

existing particles grow. The growth rate is controlled by both diffusion and reaction kinetics. Finally, the growth of particles is terminated by passivation of the NC surface using organic ligands to coordinate or bind to the nanocrystal surfaces. These ligands prevent agglomeration and fusing of particles, and they make the particles soluble in certain solvents.

A prerequisite for achieving monodisperse NCs is decoupling of nucleation event from the growth step. One method involves shortening the time period of nucleation in comparison to the growth period. That way, all nuclei will undergo a similar growth period, resulting in a narrow size distribution, as shown in Figure 1-2. If the nucleation period is long and concurrent with the growth process, the final particle size and shape will be poly-disperse.

Currently, the most successful and widely-used NC syntheses have relied on the rapid injection method, first demonstrated by Murray and Bawendi in 1993.^[22] In this injection method, precursors are swiftly injected into a hot reaction system with rapid stirring. After injection, fast nucleation occurs, and this is followed by a relatively long growth period. Upon nucleation, the concentration of reactant in solution drops below the critical concentration for nucleation, and further material can only add to the existing nuclei. Growth rate is controlled by the rate of diffusion of reactant to the particles and/or by the reaction rate. Ultimately, the growth will be balanced by the solubility. Since the nucleation time is determined by the rates of both injection and diffusion, injection-based syntheses have poor reproducibility and are unsuitable for large scale production, making these methods unsuitable for industrial use. Consequently, non-injection methods are needed to enable the development of nanotechnologies.

In organic phase syntheses, most the formation of NCs occurs at high-temperature (> 200 °C). In the one-pot method, the precursors are mixed at room temperature or relatively low temperature before the reaction mixture reaches the reaction temperature. The heating from room

temperature to a high temperature often results in undesired nucleation concurrent with growth. This factor poses a major challenge in the preparation of monodisperse NCs using non-injection methods. To overcome this problem and separate the nucleation and growth steps, different methods have been tested. Recently, our group has reported non-injection syntheses of CdS NCs using nucleation initiators,^[50] and CdSe and CdTe NCs by choosing precursors with suitable reactivity.^[51] The addition of seed particles to the reaction mixture is another way to separate the nucleation and growth processes.^[52]

As described in LaMer's curve, when the active monomer concentration drops below the critical concentration of supersaturation, nucleation ends and the growth progress of NC can be controlled by the diffusion process. But in actuality, the reaction system is much more complicated than indicated by LaMer's model. The growth of NCs can be described by the diffusion of monomer towards the surface of the growing NCs, followed by dissociation rate of the surface capping ligands from the particle surface, and the subsequent reaction of diffusing particles or atoms assimilated onto the growing NCs. Thus, any parameters which can affect the diffusion rate or the interaction between the ligands and the NC surfaces (e.g. solvents, ligands, reaction temperature, pressure, reaction time and concentration of precursors) all play an important role in dictating the final particle size and shape.

The difference of the chemical potential at the solid/liquid interface also affects the size distribution of NCs. The chemical potential of a small particle is higher than that of a larger particle. Therefore, the equilibrium solute concentration of a small particle is much greater than that for a large particle. The gradients of solute concentration between small particles and large particles result in the mass transport from small particles to large particle, called Ostwald

ripening or the coarsening effect.^[53-55] At equilibrium, there is a balance between dissolving and growth of the NCs.

The sizes and shapes of NCs can be controlled by tuning the number of nuclei and the chemical potentials of the components of the reaction system. This is usually realized by varying the reaction parameters: types and concentrations of precursors and ligands, reaction temperature, time and pressure, heating and stirring rates. Since the detailed chemical mechanisms of nanocrystal synthesis are not completely clear, there are no universal rules which can be applied to all nanocrystal growth. But there are some points which are useful. To obtain larger particles, a straightforward way is to increase the reaction time.^[56] Based on Gibbs' law, a particle in equilibrium with its surroundings should have the minimum surface energy. Normally, the surface energy of spherical NCs is lower than that of nonspherical particles (e.g. cubes, tetrahedral pyramids and triangular prisms). The surface chemical potentials on the individual facets are different.^[57] Thus, for shape control, the surface chemical potential must be considered.

To stabilize the NCs, special organic ligands are employed. These organic ligands contain the electron-rich capping group, e.g. a phosphine, phosphine oxide, amine, carboxylate or thiolate, can coordinate to the electron-poor metal ions, such as Cd^{2+} , Zn^{2+} and Fe^{3+} , or to elemental metals, e.g. Au and Ag. The other end group of the ligand imparts solubility to the NCs. For example, hydrophobic ends, such as alkyl groups, make NCs soluble in low-polarity solvents (e.g. toluene, hexane or chloroform), and hydrophilic ends make NCs water-soluble. The strength of ligand bonding to the nanocrystals affects the stability of the NCs. Weak bonds between the ligands and the particle surface will result in unstable NCs. Once the NCs lose the ligands on their surfaces, the particles will aggregate and precipitate. However, very strong

bonds will block the growth of NCs and result in very tiny particles. In most cases, the interactions between the ligands and the nanocrystal surfaces are not very strong. Therefore, surface modification, also called surface engineering, by ligand exchange after the initial synthesis is complete allows controlling the solubility, stability and other properties of NCs.

Another way to enhance the stability of NCs is growth of an additional inorganic shell on the core nanocrystal. Passivation by organic capping ligands is not perfect. For example, in trioctylphosphine oxide (TOPO) capped CdSe NCs, TOPO preferentially binds to cationic cadmium sites on the surface, leaving anionic selenium dangling bonds. This, as well as the steric hindrance that the bulky TOPO ligands impose on neighboring nanocrystal surface sites, leaves cadmium dangling bonds. These dangling bonds on the NC surface act as trap sites, which provide pathways for non-radiative decay of the nanocrystal excited states, and result in reduced photoluminescence in semiconductor NCs.^[58] Epitaxial growth of an inorganic shell can passivate these dangling bonds and remove trap sites. Thus, the optical properties of NCs can be enhanced by addition of an inorganic shell. The first successful preparation of core-shell NCs was synthesis of CdSe/ZnS NCs by Guyot-Sionnest and co-workers.^[59] With the addition of the wider bandgap ZnS shell, high emitting NCs were achieved. The quality of core/shell NCs is dependent on the lattice mismatch between the core and shell materials, and usually shell materials with less lattice mismatch are easier to add.

1.2 Properties of NCs

Reducing the size of bulk materials to nano-scale dimensions significantly changes the magnitude of chemical and physical properties, including optical, electrical and magnetic properties, melting temperature,^[1,60] catalytic capabilities and mechanical properties. These special properties come from quantum confinement effects and surface effects.

1.2.1 Optical and Electronic Properties

Figure 1-3 describes the changes in the electronic structure with a decrease of particle size in metals and semiconductors.^[1] In both cases, the decrease in crystal size results in discrete energies at the band edges. In a metal, the Fermi level is at the centre of a band, where the energy states do not significantly vary with decreasing particle size, and the relevant discreteness of the energy levels is very small. Only for very small particles (tens or hundreds of atoms) at very low temperature (close to absolute zero degree), is this discreteness greater than the thermal energy and measurable. The average spacing in consecutive energy levels is known as the Kubo gap.^[61] In a semiconductor, the Fermi level is between two bands, i.e., in the band gap, which is the spacing between band edges. The discreteness at the band edges results in changes in transition energies as one or more dimensions of the crystals decrease to nano-scale.

Figure 1-4 shows the change in the density of states from the completely unconfined state (3-dimensional bulk material) to the completely confined state (0-dimensional Quantum dots). In the bulk state, the energy levels are nearly continuous. But for the NC structure where the material has been spatially confined in all three directions, the energy levels are restricted to a specific set of completely quantized states. The changes in the energy states result in the size-dependent optical and electrical properties in semiconductor NCs.

One example of quantum confinement in semiconductor NCs is the size-dependent absorption and emission spectra; i.e., the color of NCs depends on their size, as shown in Figure 1-5. For example, by changing the diameter of CdSe NCs from 2.3 nm to 5.5 nm, the energy gap of this material varies from 2.7 eV to 1.9 eV, encompassing almost the entire visible region of the optical spectrum.^[62]

Semiconductor electronic properties can be described by molecular orbital (MO) theory. Theoretical analysis, based on the effective mass approximation (EMA)^[63], shows that the

electronic energy states of NCs strongly depend on the ratio of the nanocrystal radius, R , to the exciton Bohr radius, $a_B = \hbar^2 \kappa / \mu^* e^2$, where μ^* is the exciton reduced mass, \hbar is Planck's constant divided by 2π , and κ is dielectric constant of the crystal. When $R \gg a_B$, there is little or no confinement (called infinite hole mass). The Coulomb force dominates and the exciton acts as a single particle, so that: $\mu^* = m_e^* + m_h^*$, where m_e^* and m_h^* are the effective electron and hole masses, respectively. However, when $R \sim a_B$, a weak confinement occurs. The bandgap shift relative to the bulk band gap is given by:^[64]

$$\Delta E_g = \frac{\hbar^2 \pi^2}{2\mu^* R^2} - E_{Ry}^* \quad (1-1)$$

where E_{Ry}^* is the bulk exciton binding energy, called the Rydberg energy, $E_{Ry}^* = \frac{\mu^* e^4}{2\kappa^2 \hbar^2}$. When $R < a_B$, a strong confinement occurs, and the electron and hole are decoupled by the dominant quantization effect. The effective reduced mass μ^* is given by: $1/\mu^* = 1/m_e^* + 1/m_h^*$. And the bandgap shift becomes:^[64]

$$\Delta E_g = \frac{\hbar^2 \pi^2}{2\mu^* R^2} - \frac{1.786e^2}{\epsilon R} - 0.248E_{Ry}^* \quad (1-2)$$

In equation 1-2, the first term represents the quantum energy of localization, which increases as the reciprocal of R^2 for both electron and hole.^[63] The second term represents the Columbic attraction,^[63] which is negligible in the strong confinement regime. The third term is the remnant of the exciton effect.^[64] Table 1-1 lists the electron and hole effective masses, exciton Bohr radii (a_B) and band-gap energies for various semiconductors. Since the value of R is material-dependent, the relative shift of energy can vary with both the size and the composition of the material.

Compared with bulk materials, the number of surface atoms in NCs is a large fraction of the total. The surface atoms play a critical role in the surface energy and control the solubilities, stabilities, and properties of the NCs. The surface effect also influences the electronic energy levels of semiconductor NCs. The explanation of quantum confinement, based on the EMA model, ignores the atomic detail on the surface. This assumption is only correct when the NCs are capped with a higher bandgap material of sufficient thickness. However, in most cases, dangling bonds, strain defects, and partial passivation of the surface have critical effects on the lowest energy states of the nanocrystal. The shift of energy states due to surface effects can be as large as the shift due to confinement.

An atomistic tight-binding (TB) theory^[65,66] has been proposed to account for these surface effects in semiconductor nanocrystals. Recently, a realistic TB approach has provided a more accurate description for the bandgap variation with size, based on the equation:^[67]

$$\Delta E_g = \frac{I}{aD^2 + bD + c} \quad (1-3)$$

where D is the diameter of the NCs, and a , b and c are material-dependent parameters, which can be evaluated by fitting the variation of the bandgap for the different group II-VI semiconductors using equation (1-3).^[67] By growing a shell with a large bandgap on the core NC, the surface effect can be reduced. For example, capping the CdS dot with ZnS reduces the effect of the surface on the internal electronic states and optical properties. Based on the TB model, six monolayers of ZnS are needed to eliminate the influence of any surface states.^[68]

Noble metal NC solutions normally display a special color which is absent in the bulk material or the individual atoms. But unlike semiconductor NCs, where the absorption spectrum is due to excitonic transitions from the ground state to excited states, the absorption in metal NC solutions is due to the surface plasmon band. When light irradiates a metal nanocrystal, such as a

gold or silver nanocrystal, the electromagnetic field causes oscillation of the conduction electrons. If the collective oscillation of the electrons has the same frequency as that of the incident photons, localized surface plasma resonance (LSPR) occurs, resulting in unique absorption in the visible or near-infrared regions. In semiconductors, there are very few free electrons and the plasmon absorption occurs in the infrared region.

The position of the band peak of gold NCs is size-dependent. Figure 1-6 shows the absorption spectra of 9, 22, 48 and 99 nm gold NCs in water.^[69] The position of the band peak also depends on the density of electron states on the particle surface, the particle shape, and the surrounding environment, e.g. temperature and solvent.^[70] The logarithms of the extinction coefficients of gold NCs are linearly related to the core diameters and are independent of the capping ligands on the particle surfaces and the solvents used.^[71] The aggregation of Au NCs in chloroform results in a red-shift in the absorption spectra. The high-sensitivity of SPR to small environmental changes has been clearly demonstrated, and applications based on the change of the surface plasmon resonance (SPR) have been widely investigated.

Gustav Mie was the first to provide a quantitative description of SPR by solving Maxwell's equations with the appropriate boundary conditions for spherical particles.^[72] In Mie's model, the total extinction cross-section, σ_{ext} , is the sum of the absorption and scattering cross-sections of the NCs over all electric and magnetic multipole oscillations.^[73] When the particle size is less than the wavelength of the incident light, the scattering part of particles and higher order extinction terms can be neglected, and Mie's model can be simplified to the dipolar excitation mode.^[74]

$$\sigma_{ext} = \frac{6\pi^2 D^2 \epsilon_m^{3/2}}{\lambda} \frac{\epsilon_2}{(\epsilon_1 + 2\epsilon_m)^2 + \epsilon_2^2} \quad (1-4)$$

where D is the diameter of the spherical particle, λ the wavelength of light, ε_m the dielectric constant of the surrounding medium (frequency independent), and $\varepsilon_1, \varepsilon_2$ are the real and imaginary parts of the frequency-dependent dielectric constant of the substance (particles). The values of ε_1 and ε_2 can be obtained from experiment or theoretical estimation.^[75] When $\varepsilon_1 = -2\varepsilon_m$, σ_{ext} reaches the maximum. Thus, the SPR of the NCs depends highly on the particle diameter and the dielectric constant of the surrounding medium.

Mie's theory, which was derived for spherical particles, has been used in evaluating experimental results. Recent advances in the synthesis of high quality NCs with well defined shapes, such as rods, cubes, triangular prisms, multipods and polyhedra,^[76] demonstrate that the shapes of NCs also affects the SPR. Spherical Au NCs exhibit only a single peak, whereas non-spherical gold NCs exhibit multiple scattering peaks in the visible and near-infrared regions due to localized surface plasmons. For example, Au nanorods exhibit two absorption peaks, corresponding to transverse and longitudinal surface plasmons. The transverse band is around 520 nm, whereas the longitudinal band depends on the aspect ratios of the nanorods, and the intensity of these two bands depends on the alignment of the rods.^[77] In most cases, gold rods are randomly oriented in solution because of Brownian motion.

1.2.2 Magnetic Properties

Magnetic NCs, such as cobalt, nickel, iron oxide, and mixed NCs, show size-, shape- and composition-dependent properties. Coercivity (H_c) and the remanence to saturation magnetization ratio (M_r/M_s) of magnetic particles have the maximum values when the particles reach the critical sizes, which are around a few to tens of nanometers in diameter, depending on the chemical composition and crystalline structure of the particles.^[23,78,79] For the CoNi alloy system, the highest H_c can be achieved when the nanocrystal size is in the range of 20-40 nm.

Domain structure exists in particles larger than the critical size and is responsible for the decrease of coercivity and remanent magnetization. Magnetic studies of these particles have also shown that the magnetic properties are affected by the particles' surface environment,^[80] because defects on the particle surfaces change the saturation magnetization. The particle shape effect was investigated by comparing spherical and cubic cobalt ferrite, CoFe_2O_4 , nanocrystals having the same volume. The results showed that saturation and remnant magnetization of nanocrystals are determined solely by the size, regardless of the shape (spherical or cubic). However, the shape of the nanocrystals is a dominating factor for the coercivity of nanocrystals due to the effect of surface anisotropy.^[81]

The transition temperatures are also affected by the reduction of particles size. For example, the magnetic transition temperature (called the Curie temperature in ferromagnets (T_c) and the Néel temperature (T_N) in antiferromagnets) decreases with the decrease in particle size.

1.2.3 Thermal Properties

As mentioned above, the transition temperature from solid to liquid phase decreases with decreasing size of the NCs. The size-dependent melting temperature of CdS NCs decreases over 55 % when the particle size is less than 15 nm.^[60] This special property can be explained by the decrease of the energy barrier for atomic motion. Melting is a process in which the interactions between atoms, ions or molecules are broken throughout the structure. Compared to the interior atoms in the NCs, the surface atoms have surface energy, so they require less energy to disrupt the interactions with neighboring atoms and are free to move. The movement of surface atoms causes the surface to be minimized, thus reducing the surface energy. As particle size decreases, the fraction of the surface atoms relative to the total increases. Thus, less energy is required to transform the material from the solid to liquid phase.

1.2.4 Catalytic Properties

By decreasing the particle sizes of catalysts, a tremendous increase in the total surface area can be achieved. Thus, nanosized catalysts possess more active sites, which significantly influence the activity of the nanocrystal catalyst. For example, gold particles can be used as a catalyst for CO oxidation.^[82] The catalytic activity depends on the size of the gold particles, the interactions with the support material, the particle preparation method, and the activation procedure. The activity of gold catalysts is approximately proportional to the number of low-coordinated atoms at the corners of the gold particles.^[83] Palladium is the most important catalyst for carbon-carbon bond formation.^[84,85] Bawendi's group has investigated the catalytic ability of water-dispersible Pd NCs on the Suzuki coupling reaction.^[86] When 4-iodotoluene and phenylboronic acid were reacted in the presence of 2 mol % water-dispersed Pd NCs, a 97% yield of the product was obtained. In the second recycle reaction, the yield decreased to 65%, which is comparable to the reactivity of the second recycle reaction in an organic solvent (71%).

The surface structures of nanocrystals also affect the catalytic activity because of the different bonding abilities on the different crystallographic faces.^[4] For example, catalytic hydrogenation of benzene using the (100) surface of platinum yields only cyclohexane, but using the (111) surface, both cyclohexane and cyclohexene are produced.^[87]

1.2.5 Mechanical Properties

Defect-free silicon spherical NCs are four times harder than bulk silicon.^[88] These special mechanical properties of NCs can also be attributed to surface effects. Recently, a montmorillonite (MTM) / poly(vinyl alcohol) (PVA) nanocomposite was prepared by layer-by-layer assembly. MTM is composed of a 2~1 layered smectite clay mineral with a plated structure. These multilayer nanocomposites are as hard as ceramic materials, but the processing temperature is much lower^[89] than those materials. A high level of ordering of the nanoscale

building blocks, combined with dense covalent and hydrogen bonding and stiffening of the polymer chains, leads to highly effective load transfer between nanosheets and the polymer.^[90]

1.3 Bio-Applications of NCs

Optical detection based on NCs is the most widely studied and promising application of NCs. The ultimate goal of optical detection is to enable single-molecule detection *in vivo*.^[91] So far, there are three kinds of applications: semiconductor QDs as labels in fluorescent detection, Au-NC-based colorimetric detection, and surface enhanced Raman scattering. Application based on the Förster resonance energy transfer (FRET) or the other properties of NCs, such as use in magnetic separation and detection, solar cells and light emission diodes (LED)^[15], are not covered in this chapter.

1.3.1 Fluorescent Detection

Compared with traditional organic dyes, semiconductor NCs are highly photostable and have tunable, narrow and symmetric emission spectra. In addition, multicolour emission can be obtained by a single excitation wavelength. The emission wavelengths from colloidal QDs made of ZnS, CdS, ZnSe, CdTe and PbSe cover the UV to the infrared region (Figure 1-7), with most bio-applications falling in the visible and near infrared regions. Thus, semiconductor NCs present very promising applications in biological and biomedical areas. .

Advances in the synthesis of the NCs make it possible to prepare gram quantities of high quality NCs. By surface modifications, (e.g. ligand exchange^[7], or coating with silica or amphiphilic polymers^[2,32,93]) the NCs can be made water-soluble. Conjugation with protein, DNA and other biological molecules presents ways to use QDs for biosensors or in diagnosis. *In vivo* and *in vitro* tests have been carried out using QDs as fluorescent probes in a variety of biological investigations. For example, QDs capped with phospholipid micelles were injected into *Xenopus* embryos. The studies showed that QD-micelles were stable, cell autonomous, and

slow to photo-bleach, and they had low toxicity. Nanocrystal fluorescence could be followed to the tadpole stage, allowing lineage-tracing experiments in embryogenesis.^[32] Further modification of water-soluble QDs by biological molecules, such as biotin, DNA and antibodies, results in multifunctional QD-conjugates, which can be used as sensors for cancer detection^[93,94] Figure 1-8 depicts spectral imaging of QD-antibody conjugates in living mice harboring tumor cells. QD-antibody conjugates were injected into the tail vein of a control mouse (the left one, no tumor) and a tumor-bearing mouse (the right one). The autofluorescence background was separated from the QD signal using spectral mixing algorithms. The composite image clearly shows the whole-bodies of both mice and the tumor site.^[93]

The advantages of QDs make it possible to provide both long-term stability and simultaneous detection of multiple signals. But there are still many problems and challenges in the application of QDs; for example, the stability of QDs in water. High quality QDs are usually synthesized in organic phases. However, after transfer to an aqueous phase by ligand exchange, the QDs lose their high stability and also some of their optical properties.^[95] So new methods and/or more robust ligands need to be developed. Also non-specific bonding and toxicity issues need to be resolved.

1.3.2 Colorimetric Detection

Colorimetric sensors based on gold nanocrystal (Au-NC) have become an attractive research area.^[96] The bands of SPR peaks of Au-NCs are dependent not only on the size and shape of Au NCs, but also on the distances between the particles.

Oligonucleotide-functionalized gold NCs tend to aggregate in the presence of the complementary target DNA, as shown in Figure 1-9A and the color of the solution changes from red to blue (Figure 1-9B). The SPR change of Au-NCs can be measured from the adsorption spectra of Au-NP solutions or it can be observed visually. In addition, these Au-NCs demonstrate

high stability and easy surface modification. The molar extinction coefficients of Au-NP aqueous solution ($\sim 2 \times 10^8 \text{ M}^{-1} \text{ cm}^{-1}$ per particle)^[97] are much higher than those of most organic dyes.

Thus, Au NCs provide promising detection sensitivities. When bound to metal particles, DNA fragments melt over a much narrower temperature range than fragments bound to conventional organic dyes (Figure 1-9C).^[3] Based on these properties, Mirkin's group has developed many colorimetric detection methods based on Au NCs, such as detection of DNA mismatch,^[3] protein activities,^[98,99] special metal ions^[100] or other small organic molecules.^[101]

1.3.3 Surface Enhanced Raman Scattering (SERS)

The surface plasmons induce a localized electromagnetic field on the surface of the NCs. The intensity of Raman scattering is proportional to the square of the magnitude of any electromagnetic fields incident on the analyte. When analyte molecules are absorbed on metal nanocrystals, the surface provides an extra intense field and enhances the Raman signal intensity of the analyte by 10^3 - 10^{14} , depending on the size and material of the particles.^[102] This technology is called surface enhanced Raman scattering (SERS), which is a very sensitive diagnostic tool, especially when silver-coated particles are used.

Figure 1-10 illustrates that SERS of NCs functionalized with Raman-dye-labeled oligonucleotides can be used to detect oligonucleotide targets. The choice of Raman labels permits multiplexed detection of analytes. The presence of the target is confirmed by silver staining. The SERS method is very selective, and the limit of detection (LOD)^[10] is several orders of magnitude lower than the LODs of analogous molecular fluorescence based approaches.

1.3.4 Summary of the Present Research

This research was undertaken to design and improve one-pot syntheses for making high-quality metal oxide nanocrystals, to investigate the methods to synthesize hybrid nanocrystals

and to explore surface functionalization of nanocrystals by dual-interaction ligands and nanocrystal-based assay for detection of enzyme activities.

First, syntheses of NCs and their characterization in general will be described in Chapter 2, followed by syntheses of monodisperse colloidal uranium dioxide NCs (Chapter 3). By changing the amount of added surfactant, UO_2 NC sizes from 2 to 8 nm can be obtained. Mechanistic studies of the formation of UO_2 NCs show that the condensation product (amide) of oleic acid and oleylamine plays an important role in controlling the particle size. Further, octahedral UO_2 nanocrystals can be obtained by multiple addition of the precursor solution. Two kinds of heterodimers ($\text{FePt}/\text{In}_2\text{O}_3$ and $\text{UO}_2/\text{In}_2\text{O}_3$) can be prepared using a similar procedure and the synthesized HNCs exhibited different shapes (Chapter 6). High-resolution transmission electron microscopy (HRTEM) studies indicate that the shapes of these two dimers were controlled by the interfacial structures. The amorphous iron oxide layers on the FePt NC surfaces act as “glue” to interconnect the FePt with the In_2O_3 parts and led to a core-seed-shaped heterodimer. Using completely crystalline UO_2 NCs as seeds results in a peanut-shaped HNC.

Second, surface functionalization of NCs by dual interaction ligands will be described in Chapter 4. Usually, high-quality NCs are synthesized in an organic phase, but most of NC-based bio-applications require water-soluble NCs. To convert the surfaces from hydrophobic to hydrophilic, surface modification of NCs is employed. For this purpose, dual interaction ligands based on Tween-Derivatives (TDs) were synthesized. Stability tests on these TD-capped NCs show that these dual interaction ligands can significantly increase the stability of NCs compared to single interaction ligands. Further, these TD-capped QDs can be bound with a fluorescent label to monitor virus-protein expression in cells.

Third, gold nanocrystal-based assay for the detection of β -galactosidase enzyme activity will be described in Chapter 5. The optical properties of Au-NCs are not only dependent on the particle sizes and shapes, but also the distances between the particles. Here, lipoic acid-tyramine- β -galactopyranosyl (LT β -gal) was synthesized, as ligands, to cap Au-NCs; and the resultant LT β -gal-capped Au-NCs could disperse in water. After the hydrolysis of the ligands with β -galactosidase, these Au-NCs become to aggregate, which exhibit a red-shift in the absorption spectrum of the Au-NC suspension. The detection of β -galactosidase was further studies by varying the amounts of β -galactosidase.

Finally Chapter presents concluding remarks and suggestions for future studies in the synthesis and application of inorganic nanocrystals.

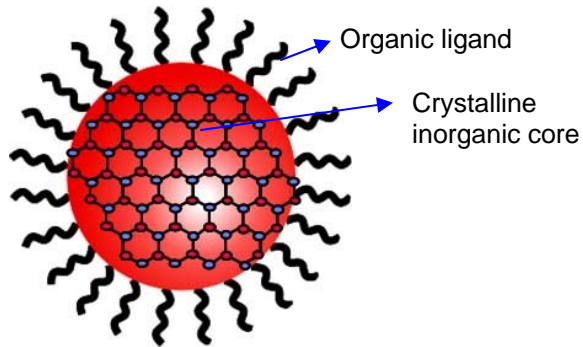


Figure 1-1. Structure of a typical nanocrystal: the crystalline inorganic core, capped by organic ligands

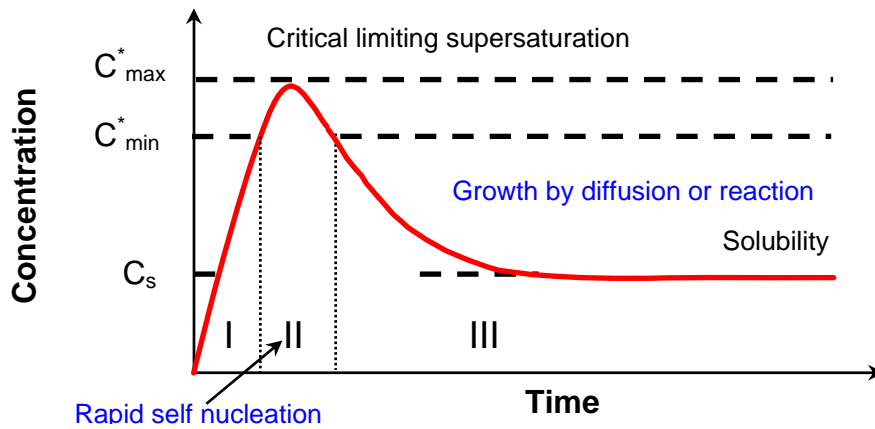


Figure 1-2. LaMer curve. In phase I, no nucleation or growth occurs; in phase II, rapid nucleation occurs and this is followed by particle growth in phase III. (Reprinted with permission from ref 49)

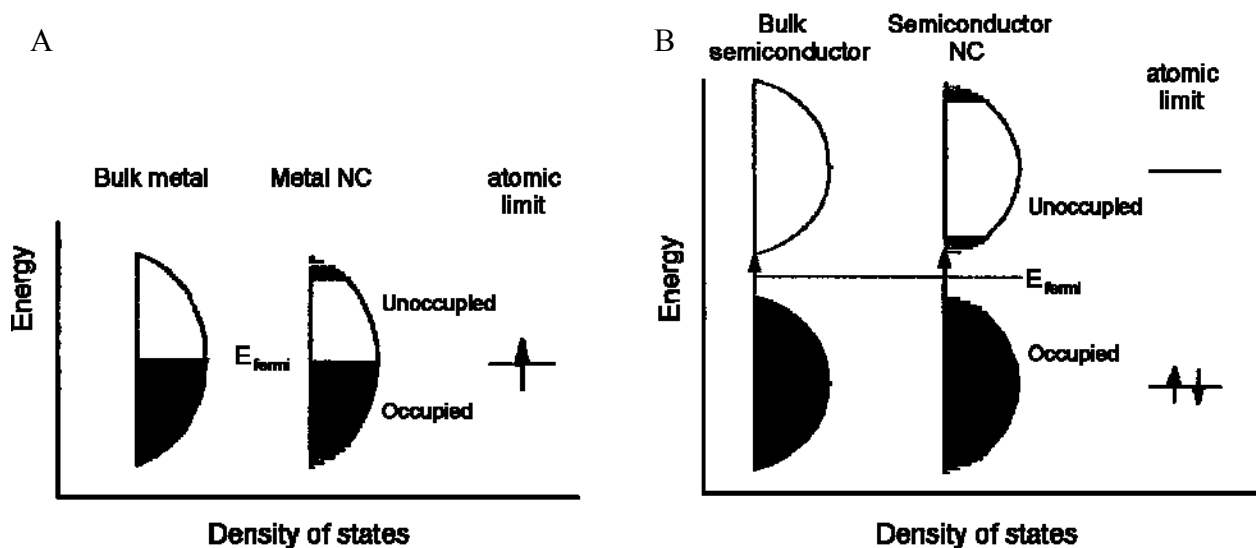


Figure 1-3. Schematic illustration of the electronic structure in A) a metal and B) a semiconductor. The density of states shows quantum size effect in a semiconductor. The HOMO-LUMO separation in the molecule becomes the bandgap of the bulk semiconductors. The energy gap of NCs depends strongly on the size of the nanocrystal. (Reprinted with permission from ref 1)

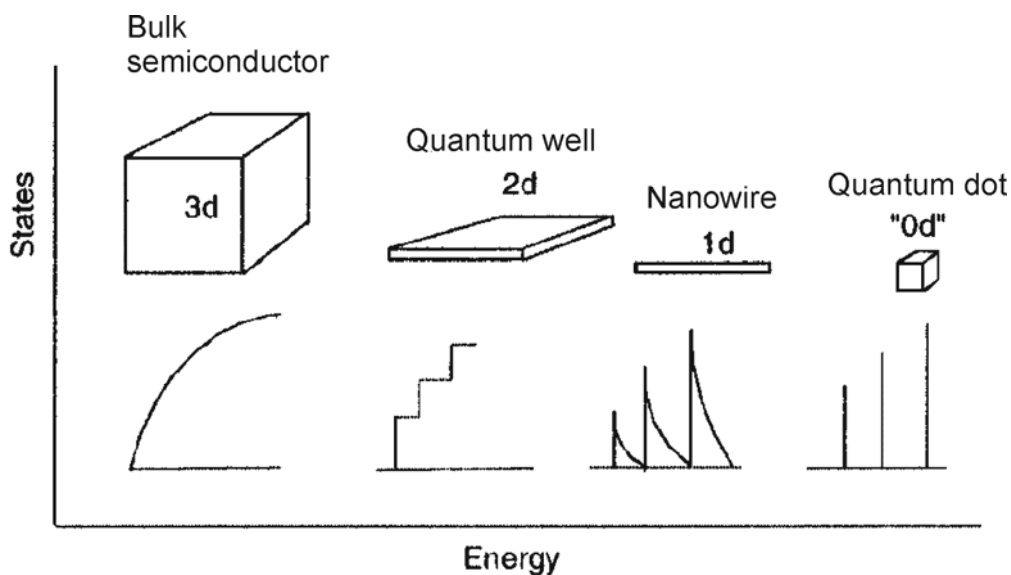


Figure 1-4. Idealized density of states for one band of a semiconductor structure of "3d", "2d", "1d", and "0d" materials. In the "3d" case the energy levels are continuous, while in the "0d" or atomic limit the levels are discrete. (Reprinted with permission from ref 1).

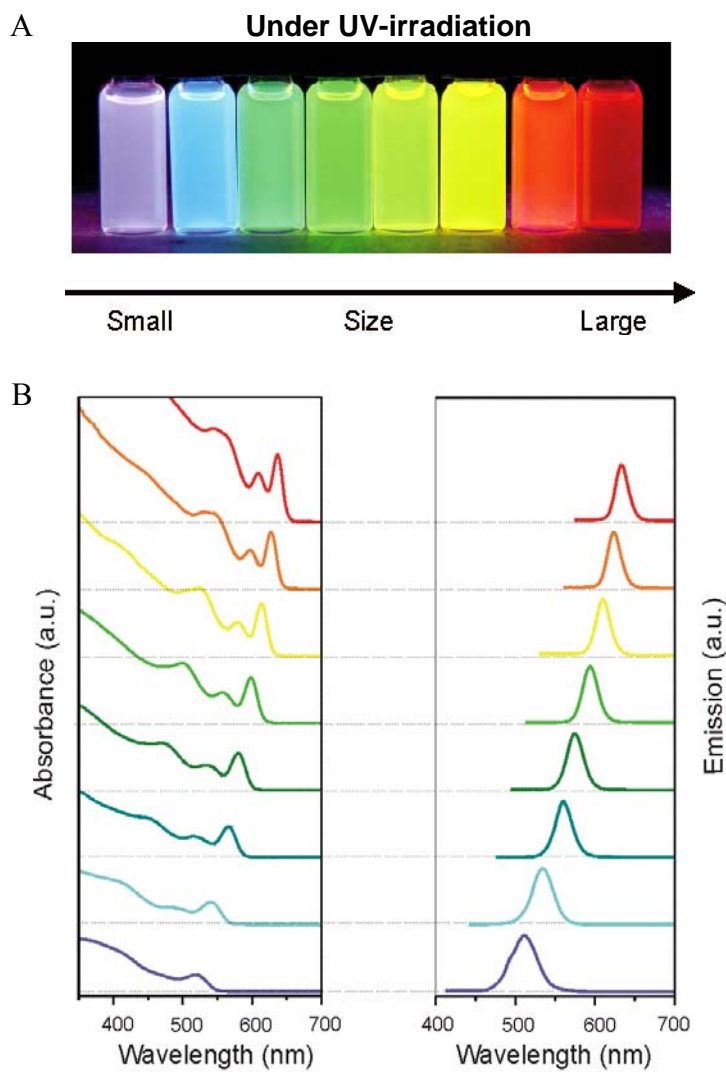


Figure 1-5. The color of CdSe NCs depends on NC sizes. A) Photo image of CdSe NCs under UV-irradiation; B) absorption spectra (left) and emission spectra (right) of CdSe NCs

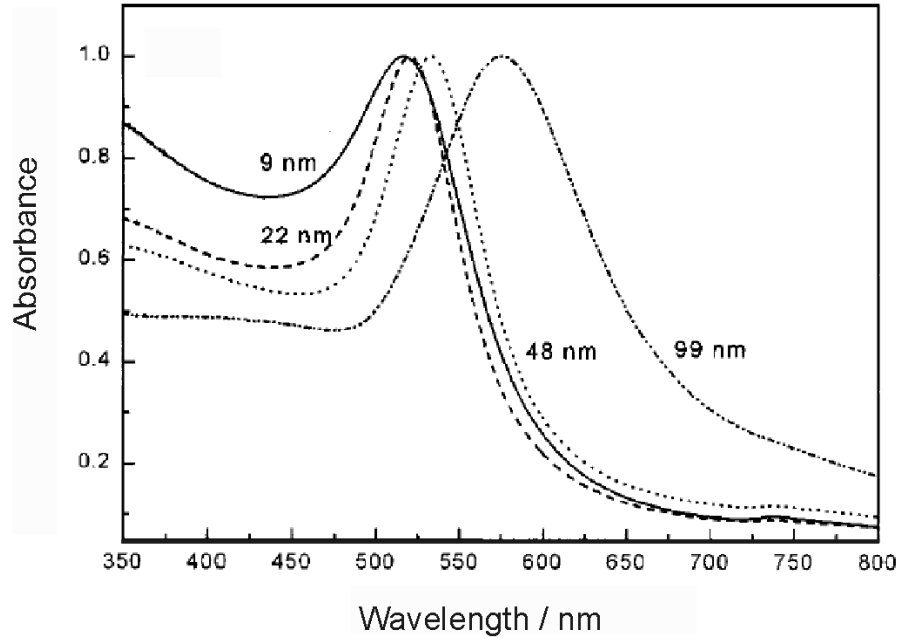


Figure 1-6. UV/Vis absorption spectra of different size Au NCs: 9 nm, 22 nm, 48 nm and 99 nm Au NCs in water (Reprinted with permission from ref. of 69)

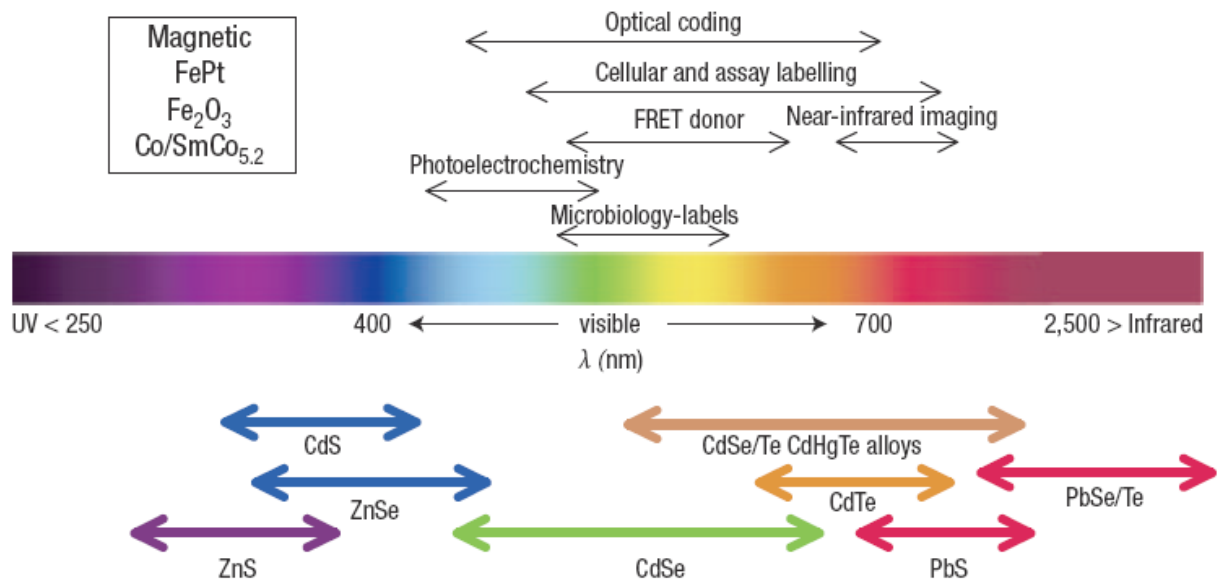


Figure 1-7. The emission wavelengths from representative QD core materials and representative areas of biological interest. (The boxed insert lists materials used for creating magnetic NCs). (Reprinted with permission from ref 92)

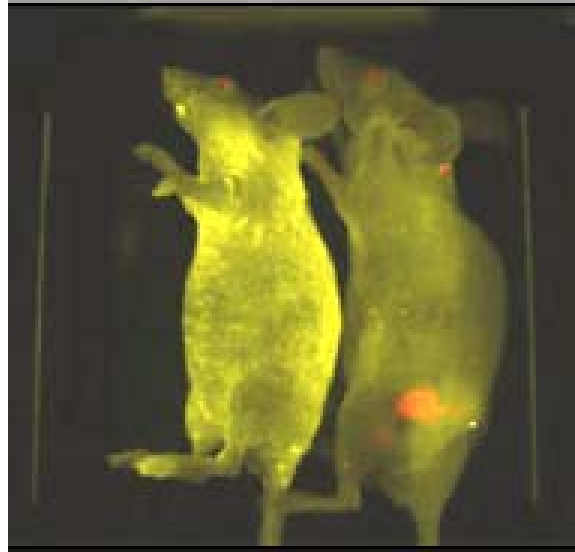


Figure 1-8. *In vivo* cancer targeting and imaging of QD-antibody conjugates in living mice. The left mouse is a control (no tumor) and the right one bears a prostate tumor (Reprinted with permission from ref 93)

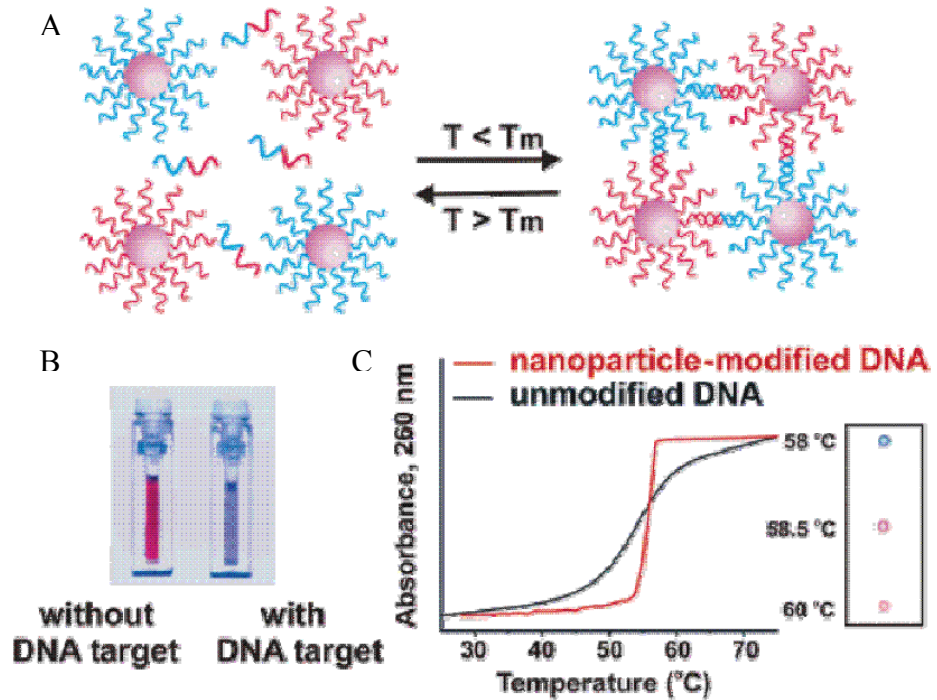


Figure 1-9. The target DNA induces aggregation of oligonucleotide-modified Au NCs. A) the scheme; B) the color change of Au NC solutions; C) the narrow temperature range of DNA fragments bound to Au NCs, compared to DNA bound to conventional organic dyes. (Reprinted with permission from ref 3).

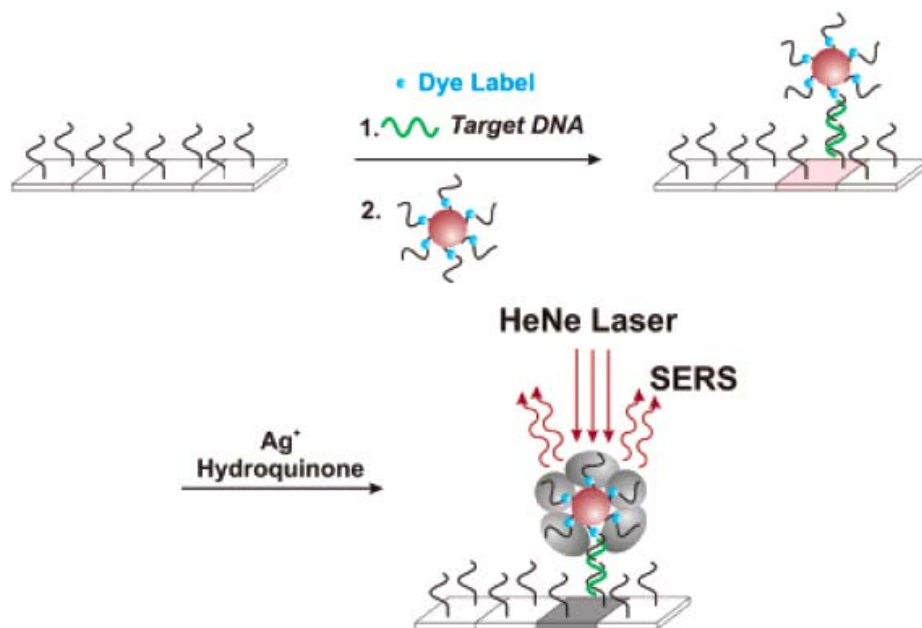


Figure 1-10. Scheme for the SERS detection of DNA fragments (Reprinted with permission from ref 10)

Table 1-1. Electron and hole masses, exciton Bohr radii and band-gap energies for various semiconductor materials

Semiconductor	m_e^*	m_h^*	Exciton Bohr Radius (\AA)	Band-gap Energy (eV)
CdS	0.2	0.9	56	2.53
CdSe	0.13	0.8	106	1.74
CdTe	0.11	0.35	150	1.50
GaAs	0.07	0.5	280	1.43
Si	longitudinal	0.52	37	1.11
	Transverse		90	
Ge	Longitudinal	0.3	50	0.67
	Transverse		200	
PbS	0.1	0.1	400	0.41

CHAPTER 2 GENERAL SYNTHESIS AND CHARACTERIZATION OF NANOCRYSTALS

Nanocrystals are important building blocks for the development of nanotechnology. The ability to synthesize NCs with controlled size, shape, composition and crystal structure is not only of technological concern, but also of importance for exploring novel properties and applications of NCs. In this chapter, the development of NC synthesis is outlined. The instruments, used for characterization of NCs, mainly include: UV/Vis spectrophotometry, fluorimetry, transmission electron microscopy (TEM), powder x-ray diffraction (XRD) and dynamic light scattering (DLS). In this chapter, the theory and operation about TEM, XRD and DLS will also be described.

2.1 Synthesis of Nanocrystals

A typical nanocrystal synthetic system contains precursors, capping ligands and solvents, and, sometimes reducing agents (e.g. NaBH_4 in gold NP synthesis) or oxidant agents (e.g. trimethylamine *N*-oxide in In_2O_3 NC synthesis^[103]). The reactions can be performed at room temperature or by heating up 300 °C (or even higher), depending on the precursor reactivity and the boiling temperature of the solvent. The choice of precursors, ligands and solvents varies for different types of NCs. The following section gives a brief review of synthetic methods for three kinds of NCs: semiconductor, metal and metal oxide nanocrystals.

2.1.1 Semiconductor Nanocrystals

Spherical semiconductor NCs, also called quantum dots (QDs), have attracted increasing interest because of their size-dependent optical and electronic properties and potential bio-applications. The first successful method for controlling the growth of group II-VI and III-V semiconductor NCs was developed by M. L. Steigerwald and L. E. Brus in the mid of 1980s to early 1990s.^[104-108] The reaction was carried out by mixing metal- and chalcogen-organic

compounds in organic coordinating solvents and heating to reflux.^[107] To obtain highly crystalline NCs with a narrow size distribution, M. Bawendi et. al. developed the injection method (Figure 2-1) by rapid injection of the precursor solution into preheated hot reaction medium: dimethyl cadmium ($\text{Cd}(\text{CH}_3)_2$) (as the cadmium precursor) mixed with trioctylphosphine (TOP) and trioctylphosphine oxide (TOPO) (as solvents and also capping ligands.)^[22] This method resulted in rapid nucleation and separation of the nucleation and growth stages, as described in chapter 1.

Detailed studies of the temporal evolution of NCs, by P. Alivisatos et.al., showed that the monomer concentration plays a key role in controlling the size distribution^[109] and also the shapes of nanocrystals.^[47] By introducing additional ligands, such as hexylphosphonic acid and trioctylphosphine oxide, rod-, arrow-, teardrop- and tetrapod-shaped CdSe NCs were obtained.^[48] Considering the toxicity and flammability of $\text{Cd}(\text{CH}_3)_2$, cadmium oxide (CdO)^[110] and cadmium carboxylates (e.g. cadmium myristate and stearate)^[111] have been successfully substituted as Cadmium precursors.

Recently, complex nanoheterostructures^[112] have been reported to improve the performance of semiconductor NCs. Growth of a shell of a higher band gap material on the core nanocrystal can increase the photoluminescence and also the stability of the initial core NCs,^[58,59,113] as described in chapter 1. Using CdSe nanocrystals with wurtzite and zinc blende structures as seeds to grow CdS nanorods, CdSe/CdS nanorods and nanotetrapods were obtained.^[114] Both of these structures showed excellent luminescent properties (QY > 80% and > 50% for nanorods and nanotetrapods, respectively) because of efficient energy transfer from the CdS arms into the emitting CdSe core.^[114]

2.1.2 Metal Nanocrystals

Metal (e.g. Au, Ag, Pt, Cu, Fe and Co) NCs provide promising applications in the areas of optoelectronics, catalysis, data storage and bio-sensors. Among them, gold colloids (Au NCs) are among the most stable and fascinating metal NCs, due to their special surface plasma resonance (SPR) properties and applications. Various methods have been investigated to prepare Au NCs. Convenient synthesis methods include the two-phase Brust-Schiffrin method^[115] and chemical reduction by trisodium citrate.

In the Brust-Schiffrin method, HAu(III)Cl_4 is used as a gold precursor. It is dissolved in toluene in the presence of tetraoctylammonium bromide (TOAB), as a phase-transfer reagent, and NaBH_4 as the reducing agent. Thiol ligands (e.g. dodecanethiol) are used to stabilize these Au NCs. The size of Au NCs can be adjusted from 1.5 nm to 5.2 nm by changing thiol/gold mole ratios. However, this is a two-phase synthesis and the evaporation of toluene by heating can cause Au NCs aggregation. Also the size distribution of Au NCs made by this method is broad. To improve the quality of colloidal Au NCs, single-phase syntheses have been developed.

Citrate reduction of HAuCl_4 in boiling aqueous solution (also called Frens's synthesis) is another popular method for preparing relatively large and water-soluble Au NCs (≥ 10 nm). Trisodium citrate acts as both a reducing agent and a capping ligand to form a citrate ion layer on the particle surface to stabilize the Au NCs. Gold NCs in the size range from 20 to 40 nm can be obtained by simply varying the solution pH with fixed concentrations of HAuCl_4 and citrate.^[116]

Other precursors, such as gold(III) chloride (AuCl_3), silver(I) acetate ($\text{Ag}(\text{CH}_3\text{COO})$), anhydrous, copper(II) acetate ($\text{Cu}(\text{CH}_3\text{COO})_2$), or platinum(IV) chloride (PtCl_4) were used as precursors for synthesis of different metal NCs.^[117] Toluene was the solvent with decyldimethylammonium bromide (DDAB) as a surfactant. Tetrabutylammonium borohydride

(TBAB) or hydrazine was used as the reducing agent, and fatty acids or aliphatic amines were added as ligands. Although this strategy can provide nearly monodisperse Au NCs ranging from 1-15 nm in diameter, the challenge remains of obtaining monodisperse NCs on a large scale. Using gold(I) chloro(triphenylphosphine) (AuPPh_3Cl)^[118] as a gold precursor instead of AuCl_3 , gram quantities of nearly monodisperse Au NCs (< 10 nm in diameter) can be synthesized by a single step.

Recently, increased emphasis has been placed on the synthesis of nonspherical metal NCs because of their shape-dependent chemical and physical properties. C. J. Murphy developed a seed-mediated growth method to prepare gold nanorods with various aspect ratios at room temperature.^[52,119,120] Gold NCs in the 3~4-nm range were prepared by addition of a strong reducing agent (NaBH_4) into an aqueous solution of HAuCl_4 and cetyltrimethylammonium bromide (CTAB). The seed solution was then mixed with the growth solution, composed of HAuCl_4 , a weak reducing agent (ascorbic acid), surfactant and silver nitrate. The amount of silver nitrate added determined the aspect ratio of the Au nanorods.^[52] Y N. Xia^[121,122] and P.D. Yang^[87,123-125] developed a polyol process to prepare polyhedral Au, Ag, Pt nanocrystals by employing the poly(vinyl pyrrolidone) (PVP) as a surface-capping agent. A metal salt is dissolved in a polyol liquid, which acts as both the reducing agent and solvent, and the mixture is heated to near-reflux temperatures. Figure 2-2 shows TEM images of polyhedral metal nanocrystals. Different shapes of nanocrystals can be obtained by adjusting the metal salt concentration, the amount of PVP, the choice of polyols and the reaction time. Polyhedral metal nanocrystals are almost entirely bound by the fcc {100} and {111} planes. The similarity between these noble metals suggests a general nucleation and growth mechanism, in which

stabilization of the {111} facets relative to the {100} facets can be used to tune final nanocrystal shape.^[87]

Cobalt, iron and iron platinum nanocrystals are also very important because of their special magnetic properties. Size- and shape-controllable Co NCs have been prepared by P. Alivisatos et.al., using rapid injection of organometallic reagents (cobalt pentacarbonyl $\text{Co}(\text{CO})_5$) into a hot coordinating solvent.^[39] C.B. Murray and S. H. Sun have reported a series of studies about the synthesis of Fe and FePt NCs.^[21,126-128]

2.1.3 Metal Oxide Nanocrystals

Nanocrystals of many metal oxides, including ZnO, SnO_2 , In_3O_4 , Fe_3O_4 , FeO, NiO, MnO and CoO, are important building blocks for materials because of their special properties, e.g. catalyst capability and magnetic properties. The ability to control the size, shape, composition, crystal structure, and surface properties facilitate their promising application.

The metal oxide NCs can be synthesized by both non-aqueous and aqueous processes.^[129] Normally, synthesis performed in organic systems provides better control over particle size, size distribution, shape, crystal structure and composition, because of the slower reaction rates compared to aqueous solutions. The choice of suitable precursor compounds is very important. The precursors employed in preparing high-quality metal oxide NCs are organometallic compounds. e.g. iron (III) acetylacetonate ($\text{Fe}(\text{acac})_3$)^[130], iron (III) acetate, iron pentacarbonyl ($\text{Fe}(\text{CO})_5$)^[131] and iron (III) oleate,^[56,132] which decompose in organic solvents to yield highly uniform and crystalline iron oxide NCs. The ligands on the surface of metal oxide NCs normally are alkyl carboxylic acids or alkyl amines. Sometimes, the ligands also serve as the solvent. The common solvents are alcohols, 1-octadecene (ODE), dioctyl ether (DOE), diphenyl ether (DPE) and toluene. Adjusting the reflux temperature of reaction mixture by varying the solvent allows the synthesis of metal oxide NCs with different sizes,^[56] and the reaction temperature also

controls their shapes. Because of the different surface energy of each crystal faces, the final geometry of metal oxide NCs is determined by balancing the relative growth rates among the crystallographic faces.^[133]

2.2 Characterization of Nanocrystals

The characterization of NCs includes the identification of the crystal morphology, the crystalline structure and the composition of the particles, and also the measurement of optical or other properties. This chapter will focus on the mechanisms of transmission electron microscopy (TEM), powder x-ray diffraction (XRD), dynamic light scattering (DLS), which are three important techniques used in this research,

2.2.1 Transmission Electron Microscopy (TEM)

Transmission Electron Microscopy (TEM) provides a direct measure of the morphology of NCs, including the size, the size distribution and the shape of the particles, as well as their crystal lattice spacing. From the image, the sizes of the particles can be determined by comparison to the scale bar; and the size distribution is evaluated from the statistical measurement of hundreds of particles.

The resolution of a TEM is defined by the Rayleigh criterion:

$$\delta = \frac{0.61\lambda}{\mu \sin \beta} \quad (2-1)$$

where λ is the wavelength of the radiation, μ is the refractive index of the viewing medium and β is the semi-angle of collection of the magnifying lens. For TEM, the refractive index and semi-angle are fixed; thus, the resolution is mainly dependent on the wavelength of the radiation source. The electron wavelength is related to the electron energy, described as:

$$\lambda \sim \frac{1.22}{E^{1/2}} \quad (2-2)$$

For example, for a 100 keV electron, the wavelength is 0.004 nm. Thus, the higher energy electrons have a smaller wavelength and a higher resolution.

Figure 2-3 illustrates the basic electron-optical system of a TEM. An electron beam passes from the gun through the specimen to the screen. The parts above the specimen (not shown in Figure 2-3) belong to illumination system and the parts below the specimen constitute the imaging system. There are two major modes in the TEM measurement, which are controlled by adjusting the imaging system lens. If the back focus plane of objective lens acts as the object plane for the intermediate lens, then the diffraction pattern will be obtained on the screen. If the image plane of the objective lens acts as the object plane of the intermediate lens, an image will be projected onto the screen.

The diffraction pattern obtained from the whole area of the specimen, as depicted in Figure 2-3A, is normally buckled, and the direct beam is so intense that it damages the viewing screen. Therefore, selective area diffraction is performed by inserting an aperture above the specimen to reduce the intensity of the pattern falling on the screen and also to select a special area of the specimen to contribute to the diffraction pattern. From the diffraction pattern, the d -spacing can be calculated by the following equation:

$$Rd = \lambda L \quad (2-3)$$

where R is the distance between the diffracted beam and the direction beam at a certain camera length (L), d the lattice spacing, and λ the wavelength of electron beam. Figure 2-4 illustrates the relationship between the spacing (R) of diffraction spots and camera length (L). Since the wavelength of the electron beam is determined by the electron energy, Rd is constant for a given camera length. To calibrate the length, a standard sample with known crystal spacing, such as polycrystalline NiO or Au, is measured. And R is obtained from the diffraction pattern. Once R

has been evaluated, the electron beam wavelength and known d of the standard can be used to calculate L .

High Resolution Transmission Electron Microscopy (HRTEM) is an imaging mode, which provides a tool to image crystallographic structure of a sample at an atomic scale. The image is formed by the interference of the diffracted beams with the direct beam (phase contrast). To obtain HRTEM, the point resolution of the microscope should be sufficiently high and also the orientation of the specimen should be along a zone axis. From the image of HRTEM, the d-spacing can be measured from the fringes. Figure 2-5 shows an example of TEM measurement of Star-shaped Fe_3O_4 NCs. A typical low resolution TEM image is shown in Figure 2-5A. From this image, the shape and size of the sample (Fe_3O_4 NCs) can be estimated. Figure 2-5B is a HRTEM image and the insert is the diffraction pattern; both show the crystal morphology of the nanostars. The lattice fringes in HRTEM have an interplanar distance of 0.19 nm, corresponding to the lattice spacing of $\{400\}$ planes in Fe_3O_4 nanoparticles.

Since the TEM images are obtained by the direct electron beam, the sample must be made sufficiently thin to allow electron transparency. All the TEM specimens for this research were prepared by evaporating one drop of nanocrystal solution on carbon-coated copper grids. The TEM micrographs were obtained using Jeol 2000cx and Jeol 2010F transmission electron microscopes operating at 200 kV. 2.2.2 Powder X-Ray Diffraction (XRD)

X-ray diffraction (XRD) provides information about the identity of the sample and the sizes of the particles. The diffraction peak positions of NCs are the same as the lattice reflections of the bulk materials, but the width of a diffraction peak is dependent on the sizes of the particles. From the size broadening, the domain size (D) of the NCs can be calculated by the Debye-Scherrer equation:

$$D = \frac{1.2\lambda}{\Delta\theta \cos \theta} \quad (2-2)$$

where θ is the observed diffraction angle, $\Delta\theta$ is the full-width at half-maximum of the peak, and λ is the wavelength of the radiation (CuK α , $\lambda=1.54 \text{ \AA}$). The average particle size is obtained by averaging D for different peaks. This equation is valid for spherical particles and more complicated equations are required for other particle shapes.

2.2.3 Dynamic Light Scattering (DLS)

Both TEM and DLS are employed for the measurement of nanocrystal size. TEM is based on the scattering and diffraction of electrons when the electron beam passes through the sample, which must be conductive or semi-conductive material and in the solid state. Thus, only the electron-dense inorganic core can be observed by TEM, and the organic ligands can not be seen. In dynamic light scattering (DLS), organic ligands also affect the diffusion of the particles, and are included in the measured radius. Thus, by using both TEM and DLS, the hydrodynamic size, nanocrystal shape, thickness of capping ligands on the particle surface, and the aggregation format in the solution can be determined.

DLS is based on the fluctuations of scattered light intensity by particles. When the particles are dispersed in a solution at a very low concentration, they move randomly due to the Brownian motion. When light passes through the solution, it is scattered by the particles. The intensity of the scattered light varies because the different phases undergo constructive and destructive interference. As the particles move over distances equal to the wavelength of the light, the phases of the scattered waves and the intensity variation (or speckle) are dramatically changed. The fluctuations of intensity of the scattered light passing through a small pinhole (smaller than the size of the speckle) are related to the diffusion time, which

depends on the particle size and shape, because small particles move faster than large particles.

Particles with a broad size distribution give broadened DLS peaks, but even in perfectly monodisperse particle solutions, effects such as interparticle interactions, orientation dynamics of asymmetric particles, and conformational dynamics or deformations of flexible particles lead to a much more complicated correlation functions. These effects are usually insignificant for scattering by particles smaller than the wavelength of the light but become important, and are often overwhelming, for larger particles.

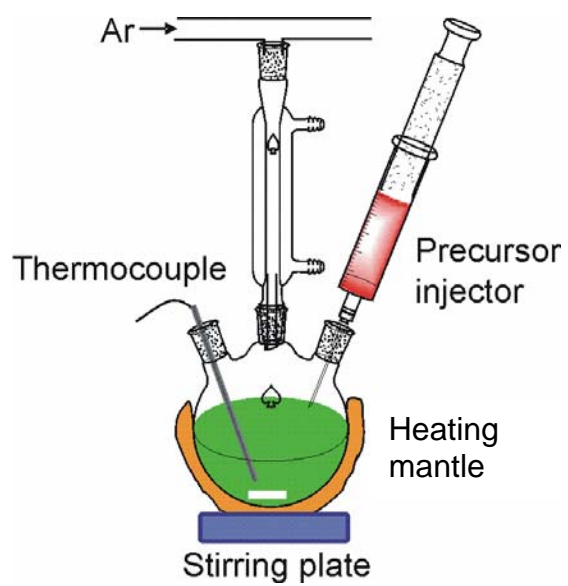


Figure 2-1. Injection method for synthesis of monodisperse semiconductor NCs

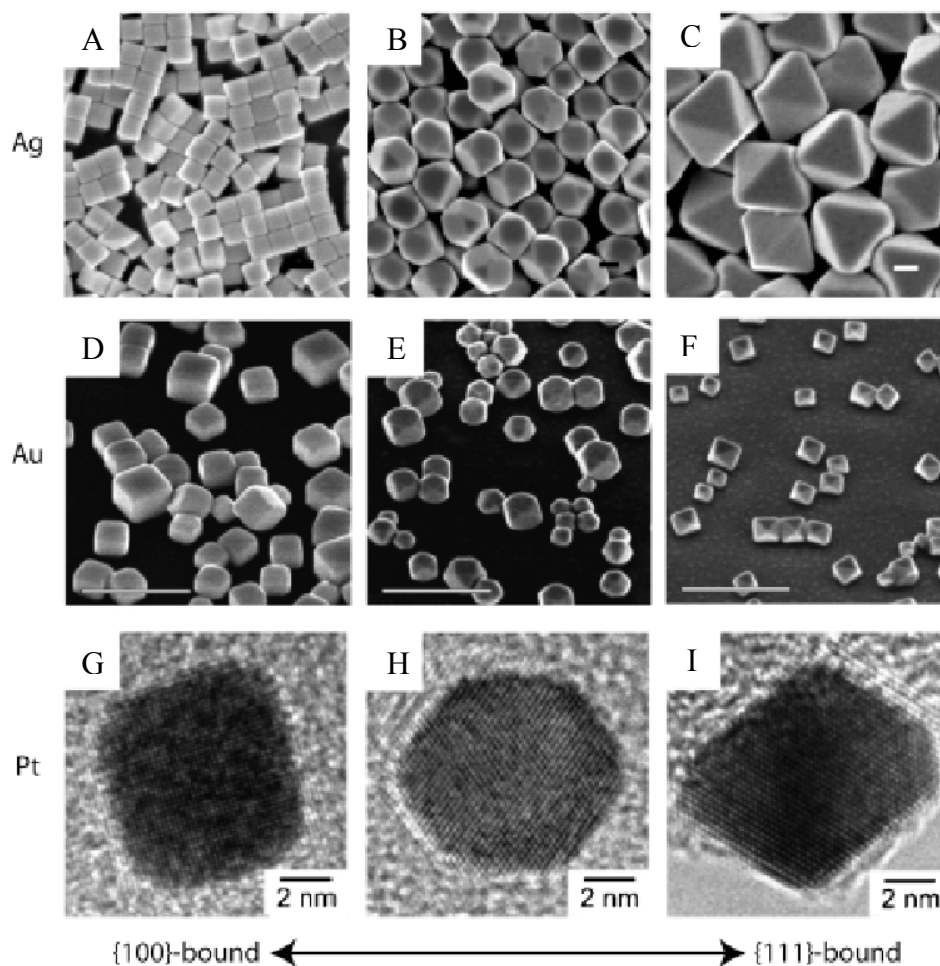


Figure 2-2. TEM images of polyhedral metal nanocrystals. Cubes, cuboctahedra, and octahedra have been obtained for silver (A-C, scale bar = 100 nm), gold (D-F, scale bar=1 μ m), and platinum (G-I, scale bar = 2 nm). (Reprinted with permission from ref 87)

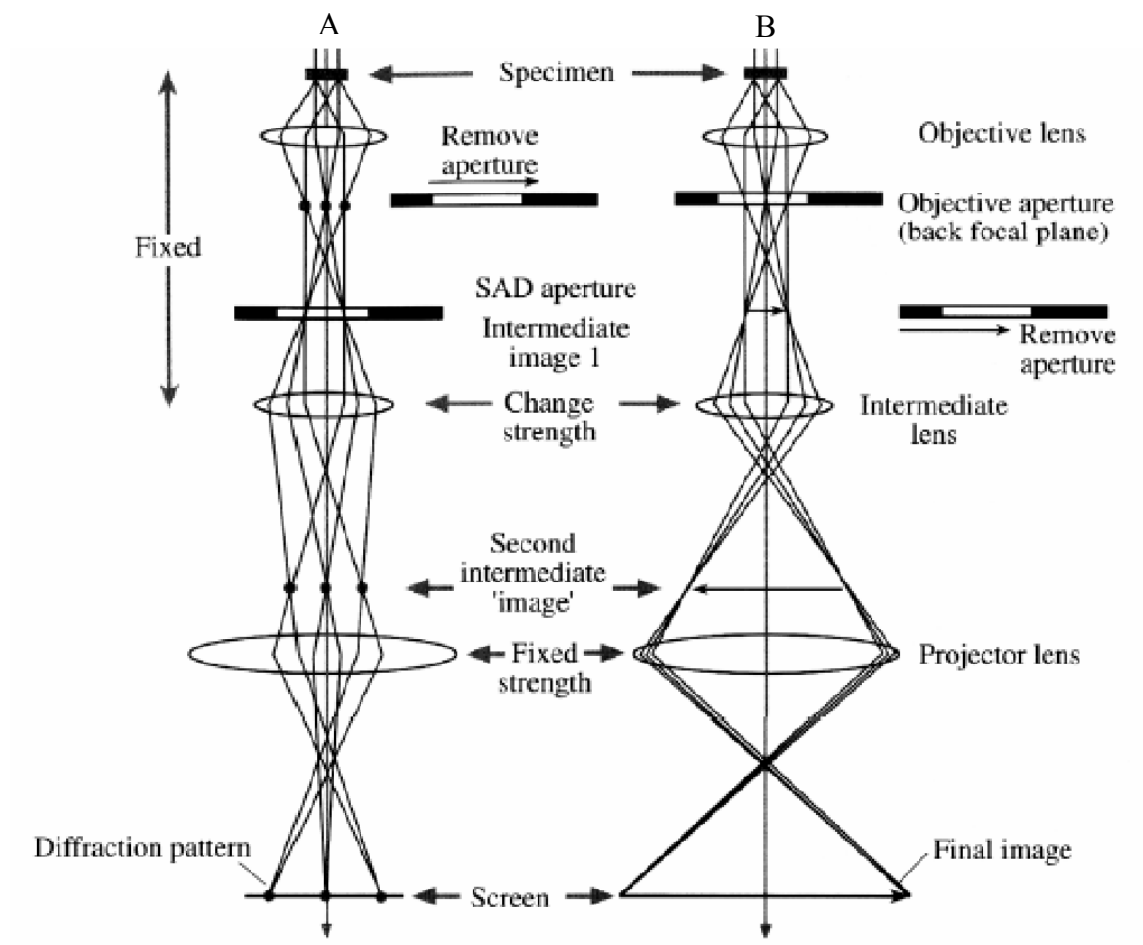


Figure 2-3. The electron-optical system of a TEM. A) in diffraction model, in which the diffraction pattern I is projected onto the viewing screen; B) in the image model. An image is projected onto the viewing screen. In each case, the intermediate lens selects either the back focal plane or the image plane of the objective lens as its object. (Reprinted with permission from ref 134)

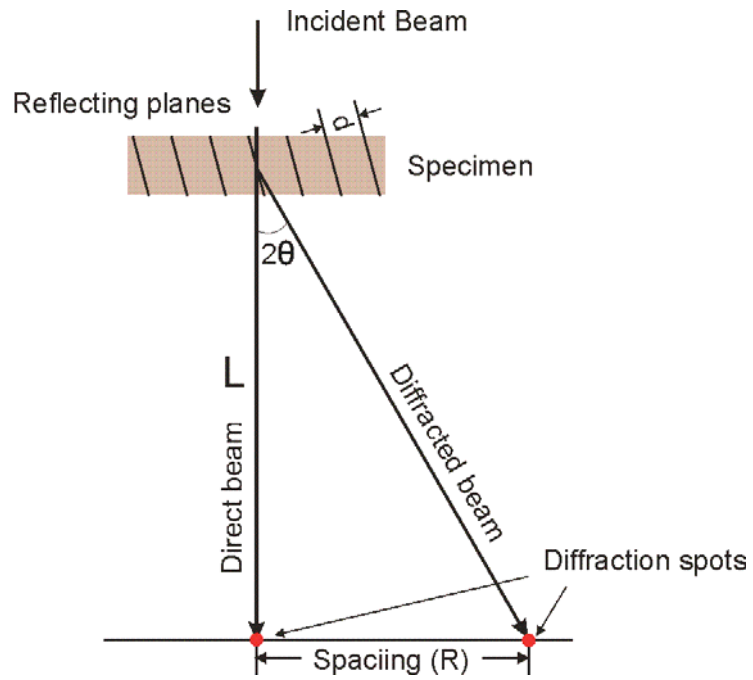


Figure 2-4. The relationship of the spacing (R) between diffraction spots and camera length (L)
(Reprinted with permission from ref 134)

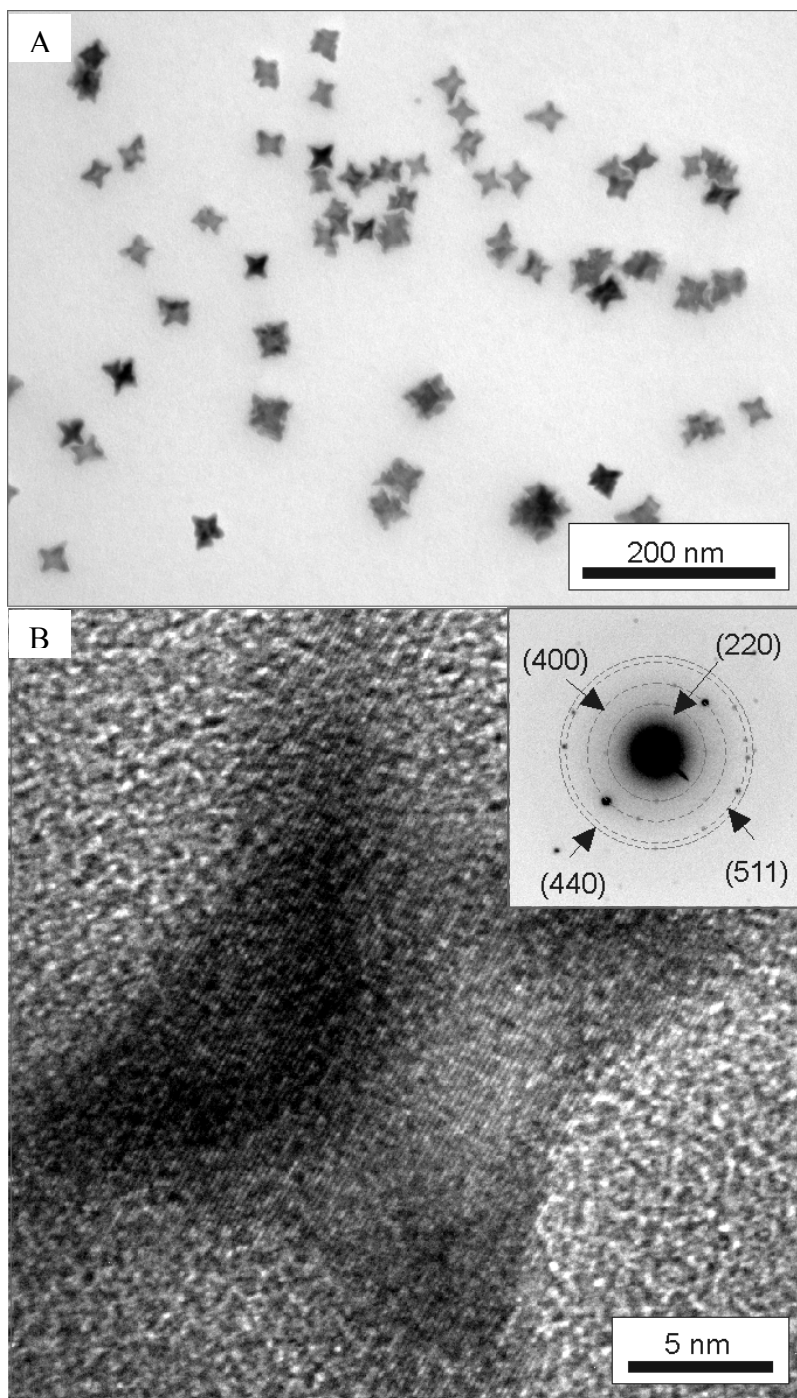


Figure 2-5. The TEM images of star-shaped Fe_3O_4 NCs. A) The low resolution TEM image; B) high resolution TEM image. The diffraction pattern of star-shaped Fe_3O_4 NCs is shown in the insert.

CHAPTER 3 SYNTHESIS OF URANIUM-DIOXIDE NANOCRYSTALS

3.1 Introduction

This chapter describes the one-pot synthesis of high-quality uranium dioxide (UO₂) nanocrystals in an organic phase. Uranium oxides are important materials for technological applications. Enriched uranium dioxide is the major component of the fuel materials for nuclear reactors.^[135] Depleted uranium oxides can be used for radiation shielding,^[135] and they are also highly efficient and stable catalysts for the destruction of chlorine-containing organic pollutants at moderate temperatures.^[136,137] In addition, uranium dioxide is a material with a high seebeck coefficient,^[138] which could be important in thermopower applications. Because nanomaterials can exhibit solution processability, as well as size-dependent physical and chemical properties,^[139] the ability to synthesize high-quality, colloidal uranium-oxide NCs would create a new opportunity to facilitate uranium-oxide-based applications. However, there has been little previous research on the synthesis of colloidal uranium-oxide NCs of high quality.^[140] Herein, we report a successful organic-phase synthesis for producing monodisperse uranium-dioxide NCs. Also, because of the high contrast of UO₂ NCs in TEM imaging, it can be used as a model system to study the mechanism of the nanocrystal formation.

3.2 Experimental Section

3.2.1 Chemicals

Uranyl(VI) acetylacetonate (UAA, 99%) was purchased from STREM Chemicals. 1-octadecene (ODE, 90%), oleic acid (OA, 90%), oleylamine (OAm, 70%), dioctylamine (98%), N-methyl-N-hexadecyl amine, oleamide (OAP, 99%), hexadecane-1,2-diol (98%), 4-dimethylaminopyridine (DMAP, 99%), *p*-toluenesulfonic acid monohydrate (TA, 98%), and 1,3-

diisopropyl carbodiimide (DIPC, 99%) were purchased from Aldrich. All the other reagents were purchased from Fisher Scientific International Inc.

4-(*N,N*-dimethylamino)pyridinium-4-toluenesulfonate (DPTS) was prepared by mixing THF solutions of 4-dimethylaminopyridine (2 M, 50 mL) and *p*-toluenesulfonic acid monohydrate (2 M, 50 mL) at room temperature with stirring. The resulting precipitate was filtered and dried under vacuum.^[141]

3.2.2 Synthesis of Spherical Uranium-oxide Nanocrystals

The uranium-oxide NCs were synthesized by thermal decomposition of uranyl acetylacetonate (UAA) in a solution of oleic acid (OA), oleylamine (OAm) and octadecene (ODE). In a typical synthesis, UAA (186 mg, 0.4 mmol) was dissolved in a solution of OA (1.0 g) and ODE (1.0 g) at 150 °C. After the solution was cooled to room temperature, OAm (1.0 g) was added, and then the resulting mixture was degassed under vacuum (~20 mtorr) at 100 °C for 10 min. Under Ar flow, the reaction solution was heated to 295 °C over about 8 min, aged at the same temperature for 5 min, and subsequently cooled to room temperature. The NCs were precipitated from the reaction solution by adding acetone and further purified by adding a mixture of hexane and acetone (1:4). The black nanocrystal precipitate was easily redispersed in non-polar organic solvents such as hexane or toluene. The typical reaction yield was about 78%.

The reaction yield (Y) of UO_2 nanocrystal synthesis was determined by $Y = P / R$, where P is the mole number of UO_2 in the total nanocrystal products and R is the mole number of UAA.

The moles of UO_2 in the total nanocrystal products (P) were calculated using formula $P = \frac{W \times Q}{MW}$,

where W is the total weight of nanocrystal product, Q is the weight percentage of UO_2 in the NCs, and MW is the formula weight of UO_2 . Q was determined by thermogravimetric analysis (TGA) by measuring the weight change due to loss of organic ligands on the nanocrystal surface.

To monitor this reaction, aliquots were taken from the reaction mixture at different temperatures during heating from room temperature to the refluxing temperature. These aliquots were diluted with toluene and then directly dropped onto TEM grids without any purification.

3.2.3 Synthesis of Octahedral UO₂ NCs by a Multiple-injection Method

Seed uranium dioxide NCs (5.4 nm) were synthesized as above, purified once by addition of acetone and dried under vacuum. Seed UO₂ NCs (17 mg) was mixed with OA (0.75 g), OAm (0.75 g), and ODE (5 g), and heated to 300 °C. The precursor solution (growth solution) was pre-made by dissolving UAA (186 mg, 0.4 mmol) in a mixture of OA (0.92 g) and ODE (8.0g) at 150 °C, and the solution was stored at room temperature. At 300 °C, 1 mL of the precursor solution was injected into the seed solution every 10 min. Prior to each injection, a 0.2 mL of aliquot was removed from the reaction solution for monitoring the growth. The NCs were precipitated from the aliquot by adding acetone, and the black NCs were re-dispersed in hexane, and then directly dropped to TEM grids.

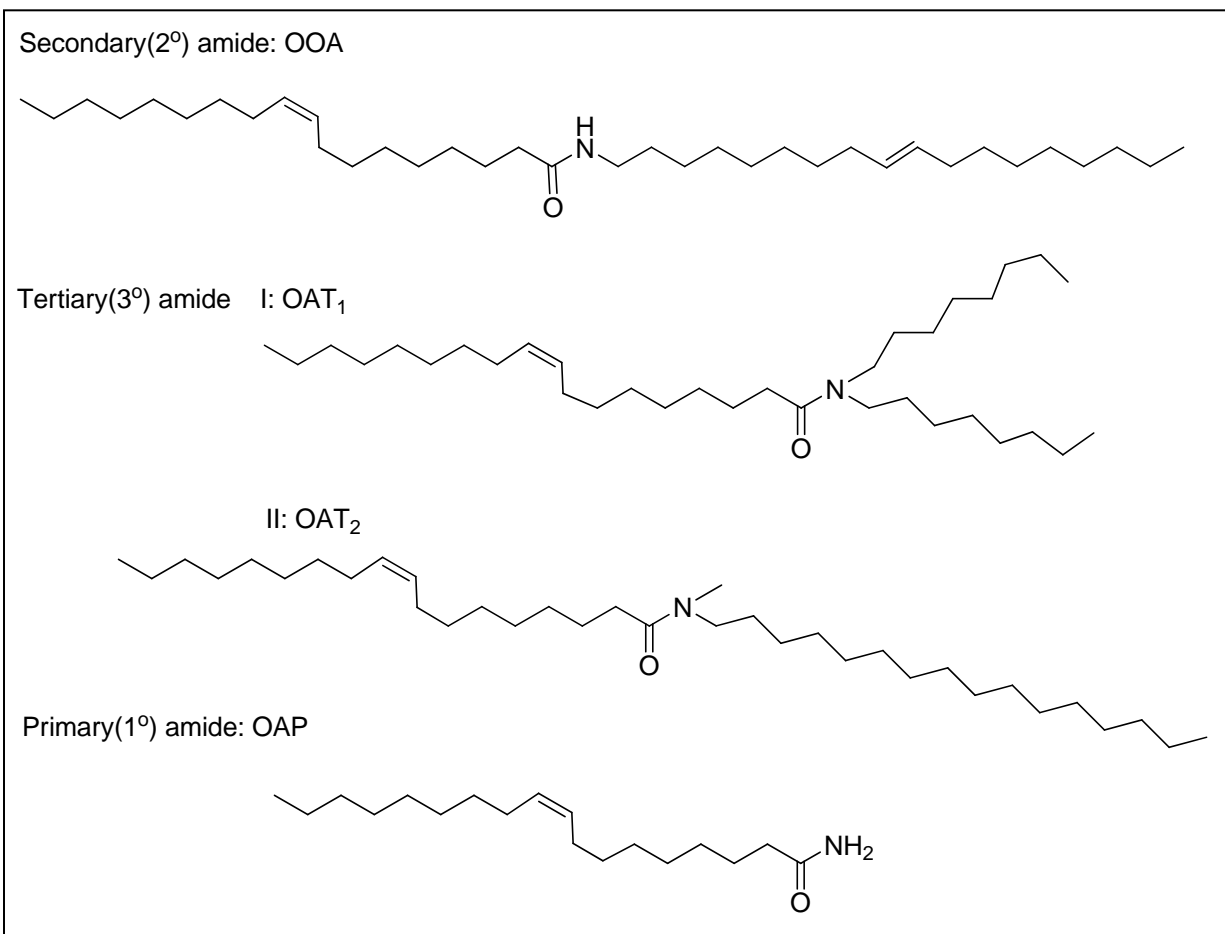
3.2.4 The Effect of Additional Mixture of OA and OAm with a Molar Ratio of 1:1

To explore the effect of additional OA and OAm, a series of syntheses were carried out, in which various amounts of a 1:1 mole ratio OA/OAm mixture were added to the UO₂ synthesis solution (UAA, 0.4 mmol; OA, 1.0g; and OAm, 1.0g). These synthetic experiments were carried out according to the procedure described in section 3.2.2.

3.2.5 The Effect of Water

To examine the effect of water, a synthesis was carried out according to the protocol described in section 3.2.2. In addition, water (1.0 mL) was slowly (over a 10 min period) added to the reaction solution after the temperature reached 200 °C during the heating stage. After the water was added, the reaction temperature was about 260 °C, and subsequently it was continuously heated to 295 °C.

3.2.6 The Amide Effect



Scheme 3-1. The molecular structures of three types of amides.

3.2.6.1 Syntheses of Amides

Synthesis of N-(*cis*-9-octadecenyl)-oleamide (OOA). Two synthetic routes were used for synthesis of OOA. Route 1: OA (3.1 g, 0.011 mol), OAm (2.7 g, 0.010 mol), and DPTS (3.7 g, 0.013 mol) were added to a flask with CH₂Cl₂ (25 mL) at room temperature under stirring. After 10 min, 1,3-diisopropyl carbodiimide (1.9 g, 0.015 mol) was added, and the reaction solution was further stirred for 5 hours. Then the reaction solution was diluted with CH₂Cl₂ (30 mL) and extracted with water (50 mL) three times to remove DPTS. The crude product was purified by flash chromatography. Yield: 70%. Route 2: OA (2.8 g, 0.01mol) and OAm (2.7g, 0.01mol) were heated to 300 °C and kept at that temperature for 1 hr. Yield: 100 %. These two

methods both led to the same product (OOA). $^1\text{H-NMR}$ (300-MHz, CDCl_3): δ (ppm) 0.89 (t, $J=6.6$ Hz, 6H), 1.27 (m, 42H), 1.49 (m, $J=6.6$ Hz, 2H), 1.63 (m, 2H), 2.01(m, 8H), 2.15 (t, $J=7.5$ Hz, 2H), 3.24 (m, 2H), 5.35 (m, 4H).

Synthesis of other amides. OA was mixed with other amines (dioctylamine, *N*-methyl-*N*-hexadecyl amine in a 1:1 molar ratio) and the mixture was heated to 300°C and kept at that temperature for 1 hr. The products were named *N,N*-dioctyloleamide (OAT_1 , Scheme 3-1) and *N*-hexadecyl-*N*-methyloleamide (OAT_2 Scheme 3-1).

$^1\text{H-NMR}$ of OAT_1 (300-MHz, CDCl_3): δ (ppm) 0.89 (9H), 1.27 (m, 42H), 1.52 (m, 2H), 1.63 (m, 4H), 2.01(m, 4H), 2.24 (m, 2H), 2.76 (t, 2H), 3.24 (m, 2H), 5.35 (m, 2H).

$^1\text{H-NMR}$ of OAT_2 (300-MHz, CDCl_3): δ (ppm) 0.87 (7H), 1.27 (m, 46H), 1.51 (m, 2H), 1.62 (m, 2H), 2.01(m, 4H), 2.28 (m, 2H), 2.93 (d, 3H), 3.30 (m, 2H), 5.35 (m, 2H).

The OOA effect. To explore the effect of adding OOA to the reaction mixture, we carried out a series of syntheses in which various amounts of OOA were added to the system described in section 3.2.2.

Other amide effects. To explore the effects of different amides, syntheses were performed as in section 3.2.2, but 4g of one of the amides, shown in Scheme 3-1 (OAT_1 , OAT_2 or OAP) was added to the reaction system.

3.2.7 Characterization of UO_2 NCs

3.2.7.1 XRD Measurements of UO_2 NCs

Powder X-ray diffraction patterns were measured on a Philips PW 3720 X-ray diffractometer with $\text{Cu-K}\alpha$ radiation. Approximately 20 mg of NCs was dispersed in 0.5 ml of toluene. Then the solution was deposited onto a low-scattering quartz plate, and the toluene was evaporated under air overnight. The Bragg diffractions of the uranium-oxide NCs can be indexed

to nearly all of those of the standard bulk face-centered cubic UO_2 , which are quite distinguishable from the Bragg diffractions of bulk UO_3 or U_3O_8 structures (Appendix A).

3.2.7.2 IR Measurements

IR spectra were obtained using a Perkin-Elmer 1600 FT-IR spectrometer. The specimens were prepared by directly loading aliquots (0.1 mL) of a hot reaction mixture onto a NaCl window.

3.2.7.3 $^1\text{H-NMR}$ Measurements

$^1\text{H-NMR}$ spectra were recorded using a Varian Mercury NMR Spectrometer (300 MHz). The samples were prepared by adding aliquots (~ 0.02 mL) of reaction mixtures to deuterated chloroform (CDCl_3 , ~ 0.8 mL).

$^1\text{H-NMR}$ measurements were used to examine the condensation reaction of OA and OAm in a modified UO_2 synthesis (section 3.2.2) The aliquots were taken from the reaction system and mixed with CDCl_3 . The protons close to the amide functional group ($\text{CH}_2\text{-NH-CO-}$) were used as probes to monitor the condensation reaction.

3.2.7.4 TEM Measurements

TEM measurements were performed on a JEOL 200CX operated at 200 kV. To prepare the specimens, a particle solution (10 μL) was dropped onto a 200-mesh copper grid and dried overnight at ambient conditions.

3.3 Results and Discussion

3.3.1 Synthesis and Characterization of UO_2 NCs

Spherical UO_2 NCs were characterized by TEM and XRD. The TEM image (Figure 3-1A) shows that the uranium-oxide NCs are nearly monodisperse, spherical particles with a diameter of 5.4 nm and RSD of 3 %. The XRD pattern shown in Figure 3-1B indicates that the NCs consist of uranium dioxide. The XRD pattern of the nanocrystal sample exhibits the highly

crystalline peaks that can be indexed to nearly all the Bragg reflections corresponding to the standard and phase pure face-centered cubic (fcc, rock salt) structure of UO_2 ($Fm\bar{3}m$, $a = 0.5468$ nm). These Bragg reflections are quite distinguishable from those of the typical crystal structures of other uranium oxides such as U_3O_8 and UO_3 (Appendix A). Moreover, this structural assignment is consistent with the high-resolution TEM (HRTEM) image (Figure 3-1, inset), which shows the characteristic cross-fringe pattern of the fcc-crystal structure viewed along the $\langle 011 \rangle$ zone axis. The ordered distance of 0.32 nm shown in the high-resolution image, corresponding to the lattice spacing of the $\{111\}$ faces in the fcc UO_2 , is in good agreement with the result from the XRD measurement.

3.3.2 Size Control of UO_2 Nanocrystals

In the synthesis of UO_2 NCs, two kinds of ligands were employed: oleic acid (OA) and oleylamine (OAm). To understand the functions of OA and OAm in the formation process, we systematically investigated how the molar ratio between OA and OAm affects the size of final NCs (Figure 3-2A–C and E). A series of synthesis experiments was carried out with nine different OA/OAm mole ratios, but with the same total solvent amount ($\text{OA} + \text{OAm} = 4.0$ g), ODE (1.0 g), and with constant amount of UAA (0.4 mmol). With increasing OA/OAm mole ratio, the size of the final NCs increased, and a maximum size was obtained when the ratio was 1:1. Then the size of final NCs decreased with a further increase of the molar ratio, shown in Figure 3-2E. However, the reaction yield was not significantly changed with the increase of the OA/OAm ratio. Taken together, these results indicate that a minimum number of stable nuclei were formed at the OA/OAm mole ratio of 1:1, and the increase of either OA or OAm led to an increase in the number of nuclei, and a decrease in final nanocrystal size.

Moreover, the size of NCs from the synthesis with OA/OAm ratio of 1:1 was larger than that of the final particles from the original synthesis (6.2 nm vs. 5.4 nm). The only difference between these two syntheses is the total amount of OA plus OAm (4.0 g vs. 2.0 g). This result may indicate that increasing the amount of 1:1 OA: OAm mixture can lead to larger final NCs. To examine the generality of this conclusion, we carried out five further UO₂ NC syntheses with various total amounts of the 1:1 OA/OAm mixture. Indeed, the size of the final NCs increased with the increasing total OA/OAm amount, as shown in Figure 3-2D. The largest diameter was 8 nm, corresponding to OA+OAm =18 g, as shown in Figure 3-2F. Further increasing the amount of the 1:1 OA/OAm mixture resulted in the decrease of particle size. Figure 3-2F also shows that increasing the amount of ODE solvent (OA+OAm constant at 2.0 g) decreases the NC size.

3.3.3 Shape Control of UO₂ Nanocrystals

3.3.3.1 Multiple-injection

Multiple-injection of the precursor solution (called growth solution) into the hot seed UO₂ NCs mixture was employed to synthesize octahedral UO₂ NCs. Figure 3-3A describes the process of multiple injection, and Figure 3-3B-D are TEM images of spherical seed UO₂ NCs, multishaped UO₂ NCs, and octahedral UO₂ NCs, respectively. After multiple-injection of the growth solution, UO₂ NCs gradually changed from 5.4 nm spherical NCs to 9.1 nm octahedra.

Since the volume of growth solution was the same for each injection, it was expected that the total particle volume would increase linearly with injection number. Figure 3-4 is a plot of volume (relative to the volume of 5.4 nm seed particles) versus the injection number. For the first three injections, the relative volume of the particles increased linearly. However, after the fourth injection, the particle volume leveled off and the remaining injections resulted in only slow growth of particles. This can be explained through the formation of additional UO₂ nuclei after the fifth injection. According to the LaMer model (see Figure 1-2), nucleation occurs only when

the active monomer concentration exceeds a critical limit (super-saturation). In the presence of seed NCs, the injected precursor solution resulted in growth on the seed NCs for the first several injections. However, with the growth of NCs, the reaction mixture gradually changed from a clear solution to a cloudy mixture, due to the decreased solubility of UO_2 NCs with increasing particle size. Thus, the growth rate of NCs decreased, and the precursor concentration began to accumulate. Eventually, the critical concentration was exceeded and more nuclei formed.

Also, a high concentration of active monomer is key to formation of octahedral UO_2 NCs. Non-spherical particles usually have a higher surface energy than spherical ones.^[123] Therefore, making non-spherical particles requires growth conditions with a high chemical potential, which can be achieved by increasing the per-particle concentration of precursors.^[51]

3.3.3.2 Ligand Effect

The functional groups of the ligands play a significant role in the NC synthesis. For example, when hexadecane-1,2-diol (HDD) was used instead of OAm, branched NCs of UO_2 were obtained. Figure 3-5 shows the TEM image of the branched NCs of UO_2 and the insert HRTEM image shows that these particles are highly crystalline with a fringe distance of 0.32 nm, corresponding to the lattice spacing of the $\{111\}$ planes in fcc UO_2 .

3.3.3.3 Self-assembly of UO_2 NCs

As described above, high-quality monodisperse UO_2 NCs can be obtained by organic-phase syntheses, which are easily adjusted for gram-scale synthesis. Since the size distribution of UO_2 NCs is very narrow, these NCs easily form self-assembled ordered monolayers (2-dimensional assembly) and multilayer 3-dimensional assemblies. Figure 3-6A shows the double-layer self-assembled pattern formed by monodisperse 5.4 nm spherical UO_2 NCs; Figure 3-6B shows monolayer self-assemble pattern formed by two sizes of spherical UO_2 NCs. The NC systems with hexagonal arrangements were created by simple self-assembly on hydrophobic

surfaces, formed by deposition of a hexane dispersion of the UO₂ NCs on an amorphous carbon-coated copper grid under toluene vapor, followed by evaporation of the solvent. By controlling the concentration of UO₂ NC solution, 2-dimensional and 3-dimensional assemblies can be obtained.

3.3.3 Mechanistic Study of UO₂ NC Formation

The formation of uranium dioxide from a uranyl precursor indicates that reduction of U(VI) to U(IV) is included in the nanocrystal synthesis. In this system, oleylamine may act as the reducing agent, with the reaction yield of a typical nanocrystal synthesis is about 78%. In addition, the synthesis is highly reproducible. Among replicate experiments, the typical deviations of experimental data (in terms of final nanocrystal size and size distribution) are less than 3%. Such a highly reproducible synthesis allows a detailed mechanistic analysis of nanocrystal formation by comparing experimental data obtained using different reaction conditions.

In the growth process, oleic acid and oleylamine ratios and total amounts significantly affect the particle size, as shown Figure 3-2 previously. The size of UO₂ NCs obtained from 1:1 OA: OAm mixtures are larger than those obtained from other ratios. Increasing the total solvent amount (OA + OAm mixture) at the 1:1 ratio can lead to further size increase, as shown in Figure 3-2F, with maximum size of 8 nm, obtained when the total amount was 18 g. Thus, a fundamental question is raised as to how the amount of the OA/OAm mixture affects the final particle size.

IR analyses (Figure 3-8A) show that UO₂-nanocrystal formation is accompanied by the formation of *N*-(*cis*-9-octadecenyl)-oleamide (OOA), due to the condensation reaction of OA and OAm. This result suggests that the OA+OAm condensation reaction may affect UO₂ nanocrystal synthesis. ¹H-NMR analyses (Figure 3-8B) further indicate that the condensation reaction was

nearly complete before the nucleation of UO_2 NCs. Therefore, the products of the condensation reaction may play significant roles in controlling the formation of UO_2 NCs.

The two major products of the condensation reaction are water and OOA. To test the effect of added water, we carried out UO_2 synthesis while adding water during the heating stage. Figure 3-9A shows the TEM image of UO_2 NCs with addition of water, and Figure 3-9B is a typical TEM image of 5.4 nm UO_2 NCs without the addition of water. It is obvious that water does not significantly affect the size of the final products, thus indicating that OOA is important in the formation of UO_2 NCs.

To examine the effect of OOA in more detail, we first synthesized OOA according to a literature method. Then, six UO_2 -synthesis experiments were carried out based on the original synthesis (UAA, 0.4 mmol; OA, 1.0g; OAm, 1.0g and ODE, 1.0 g) but with various amounts of OOA added. The results from these experiments show that the sizes of final particles increase with the amount of additional OOA (Figure 3-2F), and that the NCs reach their maximum size of 7.8 nm when the additional OOA is 18 g. Significantly, the effect of OOA almost perfectly matches that of the 1:1 OA/OAm mixture (up-triangles in Figure 3-2F). These results provide unambiguous evidence that it is OOA—not the mixture of OA and OAm—that plays the major role in controlling the formation of UO_2 NCs. Furthermore, to determine whether the amide functional group or the hydrocarbon chain on OOA generates the effect on UO_2 -nanocrystal formation, we carried out five syntheses based on the conditions used in the original synthesis but with different amounts of octadecene (ODE). The results show that additional ODE leads to the opposite effect on UO_2 nanocrystal formation: the size of the final products decreases as the amount of ODE increases (Figure 3-2F). Therefore, it is likely that the amide functional group on OOA generates the major effect on the formation of UO_2 NCs.

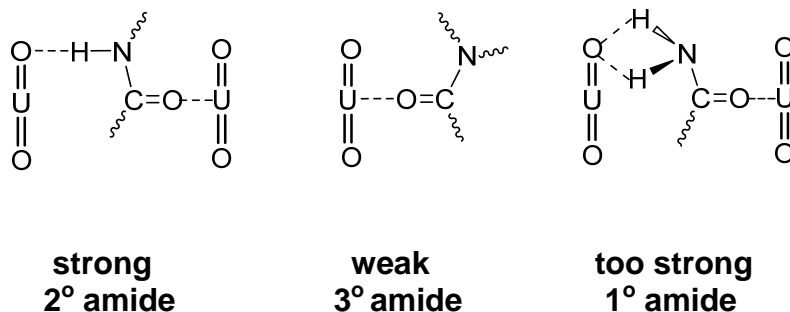
Interestingly, IR analysis of purified UO₂ NCs shows conclusive evidence that OOA is not on the nanocrystal surface, but that the NCs are passivated by OA through a chelating bidentate interaction (Figure 3-10). In the IR spectrum of the UO₂ NCs, the peak at 1531 cm⁻¹ comes from the asymmetric vibration band of C=O, and the peak at 1456 cm⁻¹ is the symmetric vibration band of C=O. The wavenumber separation between the asymmetric and symmetric bands is 75 cm⁻¹. Such a small wavenumber separation indicates that oleate anions are bonded to the UO₂ nanocrystals through chelating bidentate interaction.^[143,144] Moreover, the IR spectrum of UO₂ nanocrystals is quite distinguishable from the IR spectrum of OOA. This result clearly shows that OOA is not on the surface of UO₂ nanocrystals.

These results indicate that the effect of OOA on the nanocrystal synthesis is likely achieved via tuning the reactivity of the intermediate states (or active monomers) in the formation of UO₂ particles. The product yields for these reactions are similar and independent of the final particle size. Thus, the size of NCs is controlled by the number of nuclei formed, with particle size decreasing as the number of nuclei increases. This indicates that the amide affects the growth of NCs by blocking nucleation via an interaction between the amide and the surface of NCs.

To check the effect of the amide functional group on the activity of the intermediate states in the formation of UO₂ particles, four types of amides were studied. The molecular structures of these amides are shown in Scheme 3-1: oleamide (OAP) is a primary amide; *N*-(*cis*-9-octadecenyl)-oleamide (OOA) is secondary amide, *N,N*-dioctyloleamide (OAT₁) and *N*-hexadecyl-*N*-methyloleamide (OAT₂) are both tertiary amides, differing in the lengths of the carbon chains on the amide nitrogen. In OAT₁ there are two C-8 chains; and in OAT₂, one carbon chain is C-1 and the other is C-15. Figure 3-11 shows the TEM images of UO₂ NCs,

obtained by the addition of the different amides. The UO_2 NCs generated from OOA system have 6.5 nm diameters with RSD around 5%. The diameters of UO_2 NCs from the OAT_1 and OAT_2 systems are 5.7 nm with RSD around 5% and 5.1 nm with RSD around 8%, respectively. The OAP system produced UO_2 NCs with a very broad size range of 1-4.5 nm.

Since the reaction mixtures are the same, and the only difference is the type of additional amide, the particle size must be affected by the amide. The intermediate states of the formation of UO_2 NC are free UO_2 units and very small UO_2 clusters, both having an interaction with amides. As the concentration of amide group in the reaction mixture increases, the amide- UO_2 interaction becomes more favorable, resulting in fewer nuclei being formed. Thus, increasing the amount of OOA results in large UO_2 NCs. The strength of the interaction between amide functional groups with the intermediate states also affects the nucleation. Scheme 3-2 illustrates the hydrogen-bonding between amides and UO_2 . The tertiary amides: OAT_1 and OAT_2 have weaker interaction with UO_2 than the secondary amide OOA. Therefore, more nuclei are generated in the OAT_1 and OAT_2 systems and smaller UO_2 NCs are obtained. The steric hindrance effect in OAT_2 is weaker than that in OAT_1 . Thus the interaction of OAT_1 with the intermediate stage is a little stronger than that of OAT_2 , and fewer nuclei are formed in OAT_1 , compared to OAT_2 system.



Scheme 3-2. Schematic illustration of the interaction between amides and UO_2 molecules

The interaction between the primary amide OAP and the intermediate states is so strong that the growth of nuclei is blocked. Thus smaller NCs with a very broad size distribution are obtained. In this case, the product yield of the reaction was only 46% compared to 78% in a typical synthesis.

In conclusion, we have developed an organic-phase synthesis for making high-quality, colloidal UO_2 NCs. By multi-addition of the uranium precursor solution, octahedral UO_2 NCs were obtained. Second, we have mapped out the functions of the solvents (OA, OAm, and ODE) in the synthesis, and have found that OOA—a product of the condensation of OA and OAm—can substantially affect the formation of UO_2 NCs. Importantly, these results provide fundamental insight into the mechanism of UO_2 nanocrystal synthesis. In addition, because a mixture of OA and OAm has been widely used in preparation a variety of high quality metal or metal-oxide NCs,^[21,145] the results herein should also be important for understanding the detailed mechanisms of those syntheses.

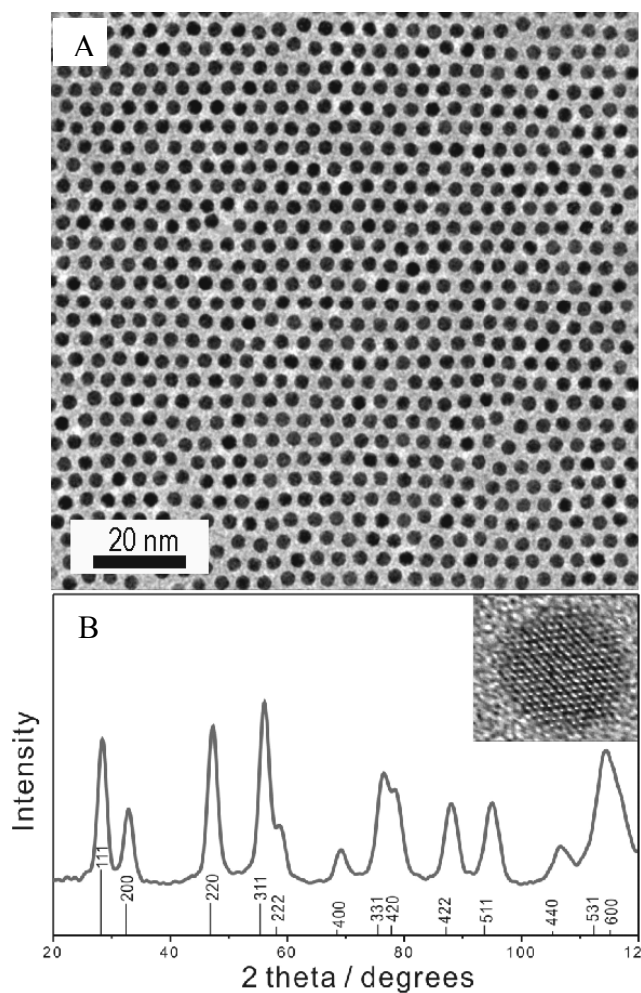


Figure 3-1. Characterization of UO₂ NCs. A) A TEM image of UO₂ NCs made in the typical synthesis; B) XRD pattern of the UO₂ nanocrystals. The standard diffraction peak positions and relative intensities of bulk cubic UO₂ are indicated. The inset shows a HRTEM image (6.5 nm × 6.5 nm) of the nanocrystal sample. (Reprinted with permission from ref 142)

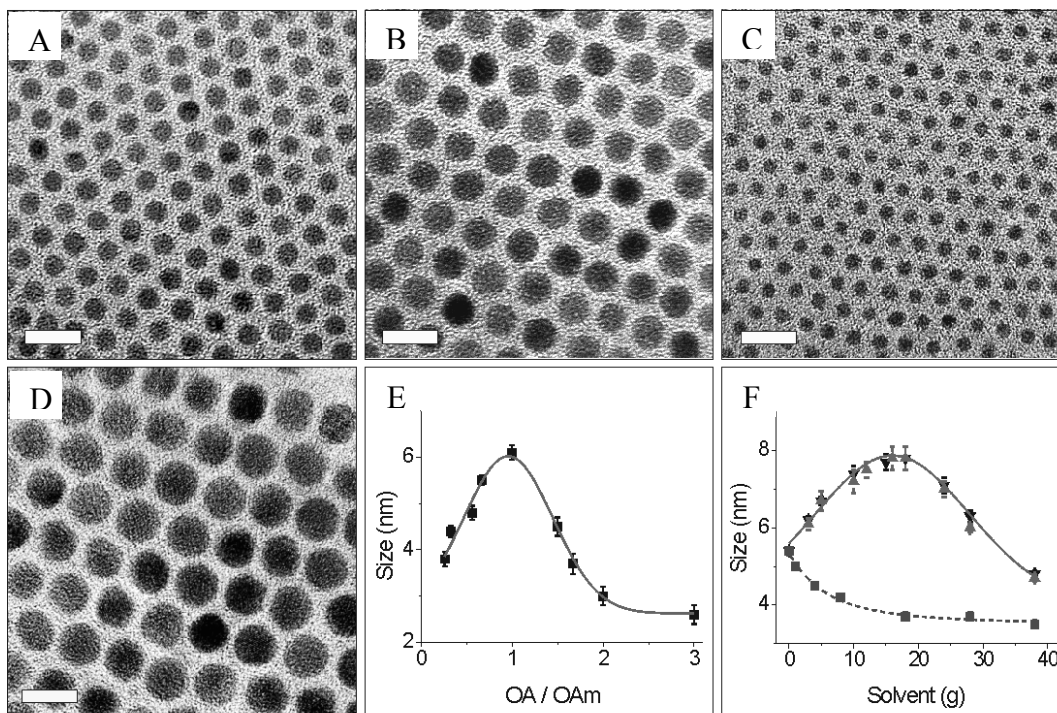


Figure 3-2. TEM images of UO_2 NCs A), B) and C) from synthesis with OA/OAm ratio of 1:3, 1:1, and 3:1, respectively. D) A TEM image of the NCs from a synthesis with UAA (0.4 mmol), ODE (1.0 g), OA (10 g) and OAm (10 g). The scale bar is 10 nm.^[142] Plots of nanocrystal diameter E) as a function of OA/OAm molar ratio from various syntheses; F) as a function of the amount of additional solvents added to the original reaction mixture: up-triangles for the mixture of OA and OAm at a molar ratio of 1:1, down-triangles for OOA, and black squares for ODE.

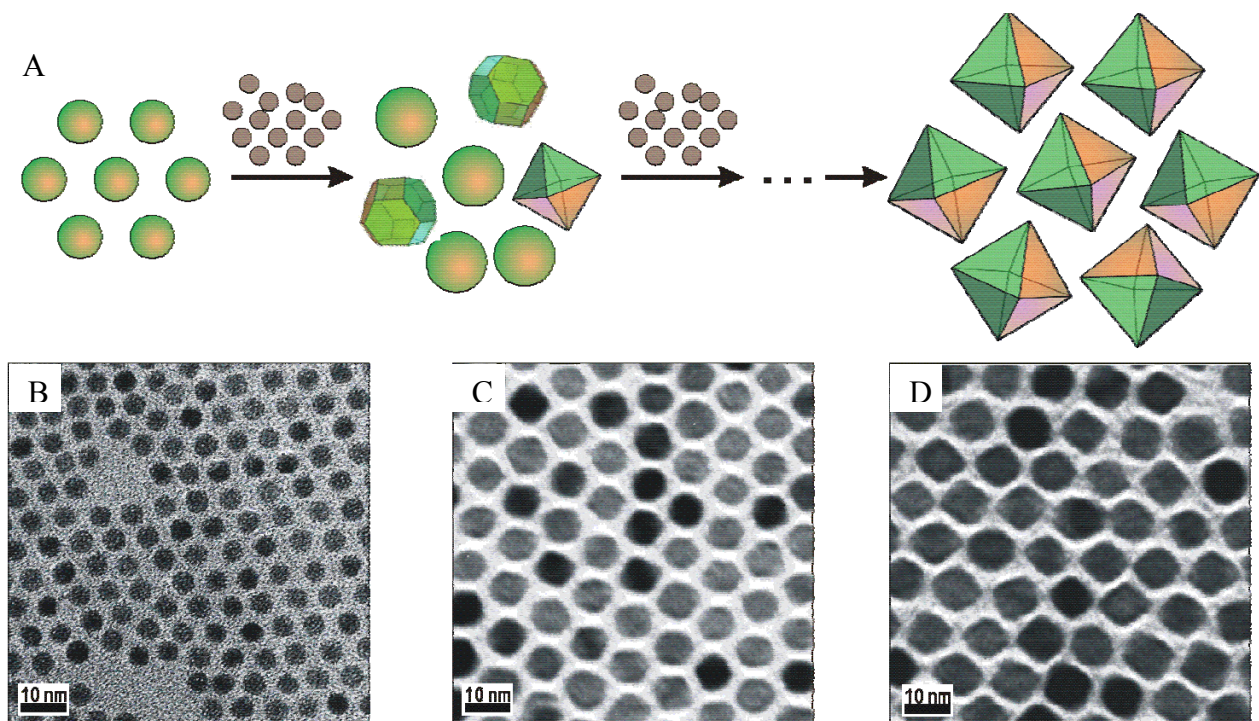


Figure 3-3. Multiple-injection method for preparing octahedral UO_2 nanocrystals. A) The scheme; B) spherical seed UO_2 NCs (diameter, $D = 5.4$ nm); C) multishaped UO_2 NCs after the 1 mL injection of the growth solution four times (edge length of octahedra, $a = 8.3$ nm); D) octahedral UO_2 NCs after the 1 mL injection of the growth solution seven times ($a = 9.1$ nm).

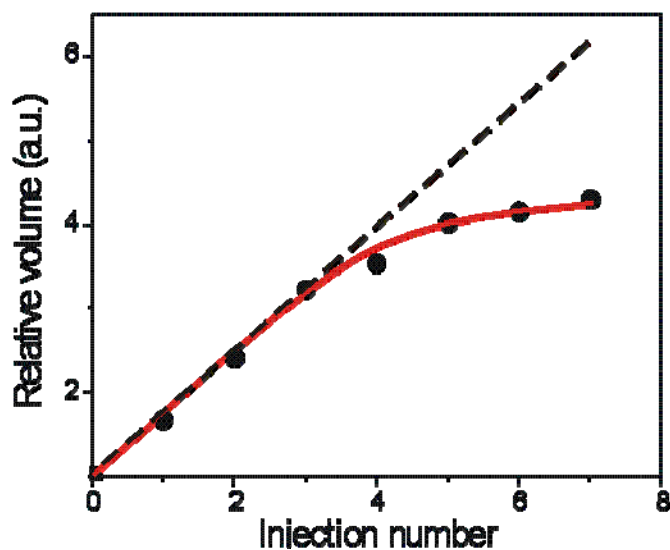


Figure 3-4. The particle growth with multiple-injection of the precursor solutions. Dashed line represents linear growth rate, and spheres are experimental data.

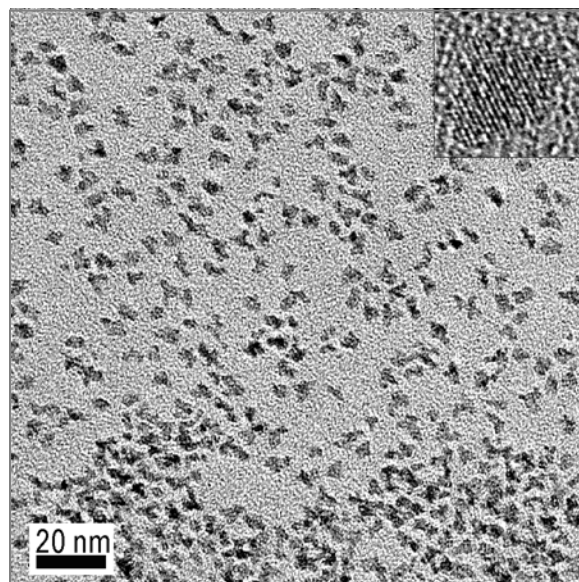


Figure 3-5. A typical TEM image of branched UO_2 NCs. The inset is the HRTEM image

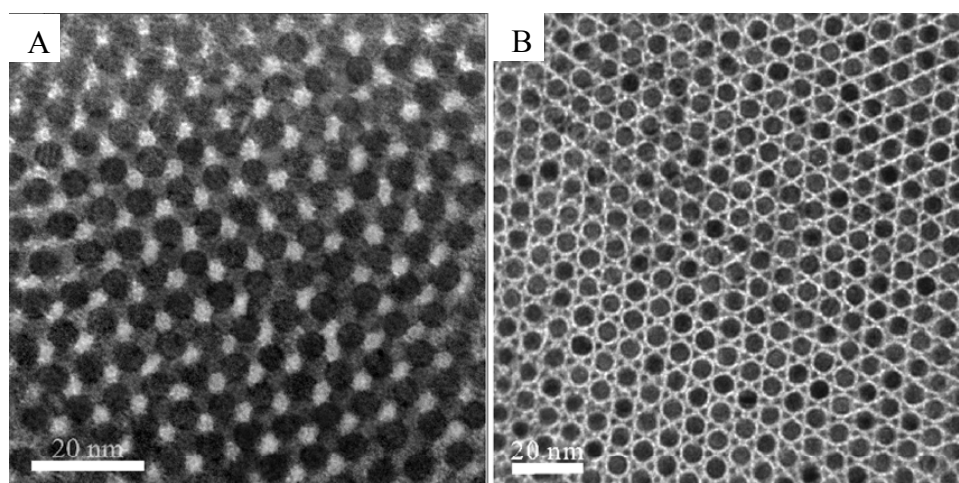


Figure 3-6. TEM images of self-assembled UO_2 nanocrystals (A) monodisperse UO_2 NCs 5.4 nm in diameter; (B) two sizes of UO_2 NCs, 6.0 nm and 2.0 nm.

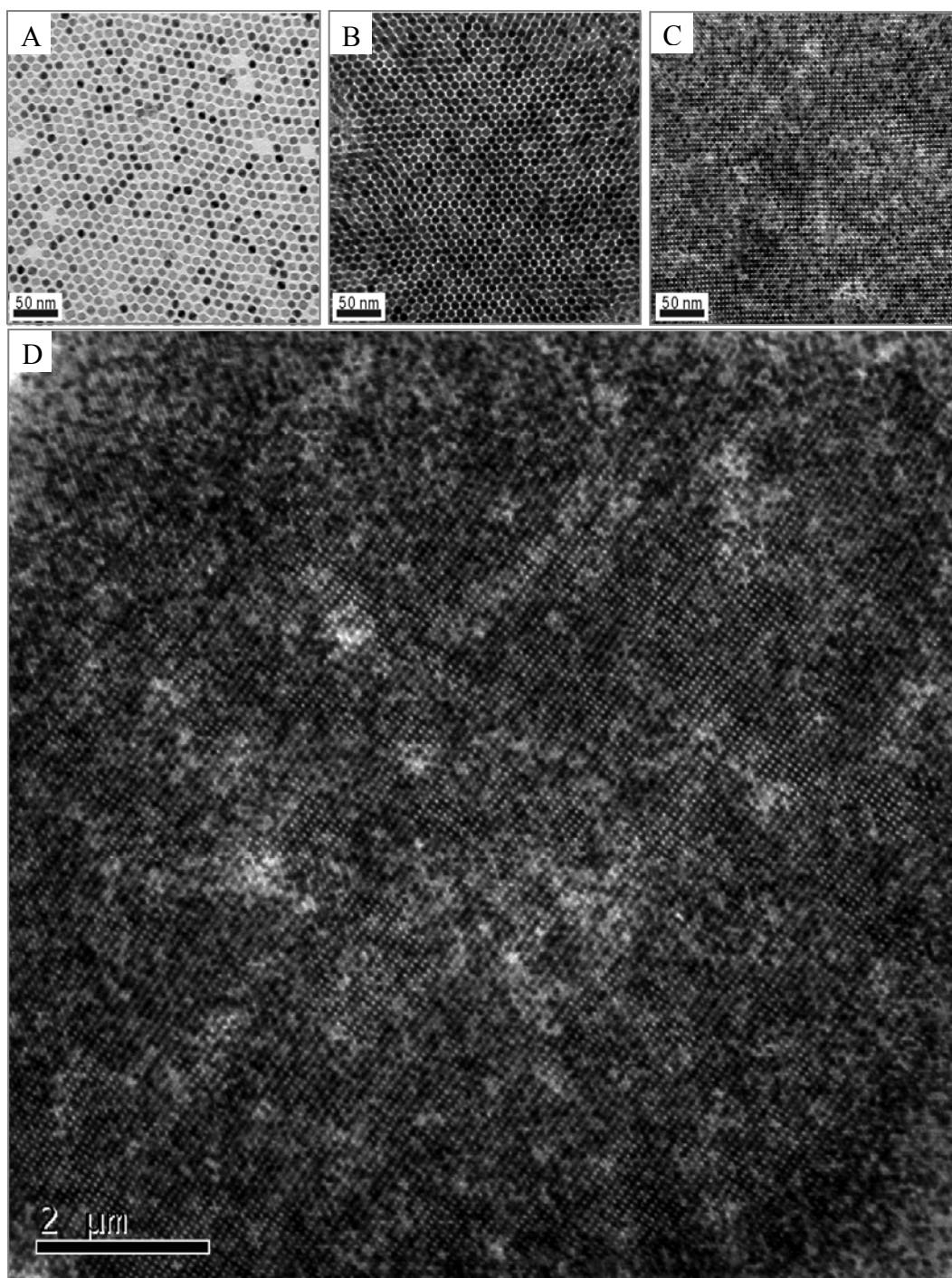


Figure 3-7. TEM images of assemblies of 9.1 nm octahedral UO₂ nanocrystals. (A) monolayer assembly; (B) and (C) 3d self-assembled patterns with a projection direction of <110> and <111>, respectively; (D) a large area assembly with projection direction <111>.

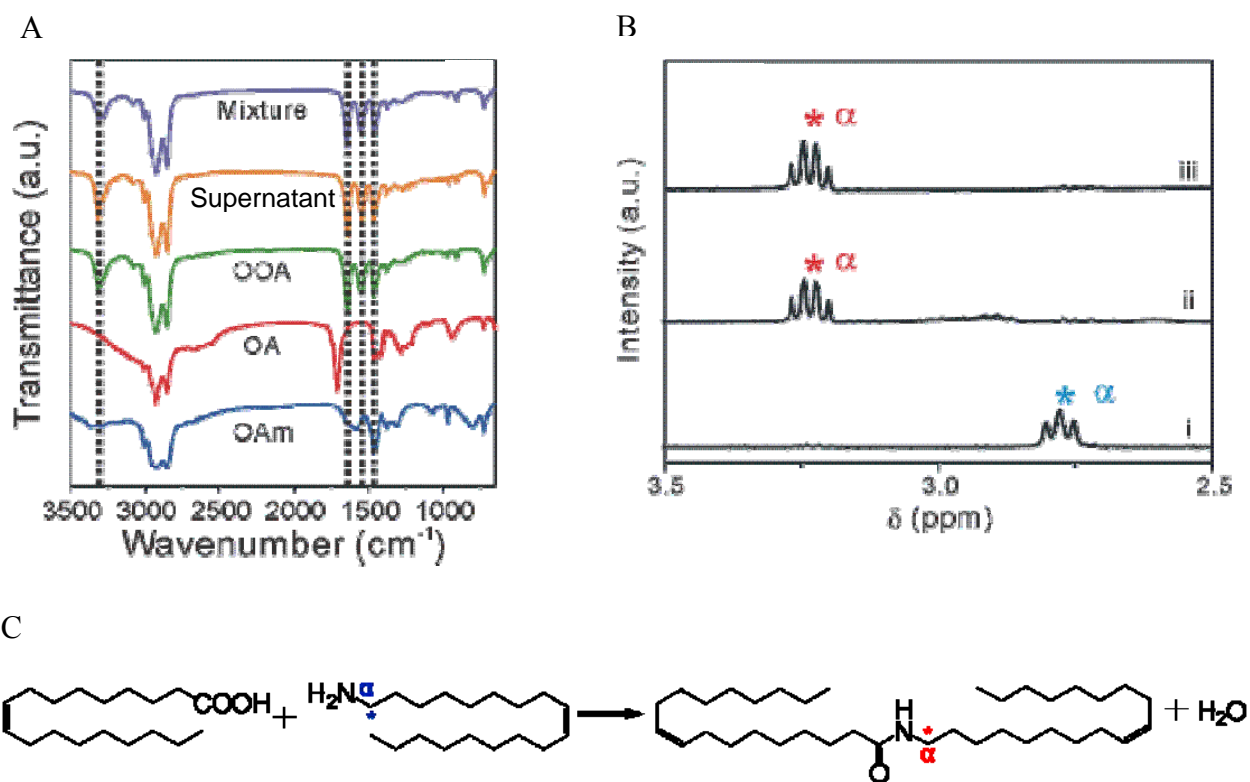


Figure 3-8. IR and ¹H-NMR spectra of reaction mixture. A) IR spectra of a reaction mixture (in violet) and a supernatant solution (in orange) from a typical 5.4-nm-UO₂-nanocrystal synthesis after the reaction solution was aged at 295 °C for 5 min; OOA (in green); OA (in red); and OAm (in blue). B) ¹H-NMR spectra (2.5-3.5 ppm region) of a reaction mixture (i) at 25 °C, (ii) at 200 °C for 20 min, and (iii) at 295 °C for 5 min. C) the equation of the condensation reaction of OA and OAm. Protons on the carbon α, close to the nitrogen, are starred on the OAm and OOA structures and corresponding NMR spectra. (Reprinted with permission from ref 142).

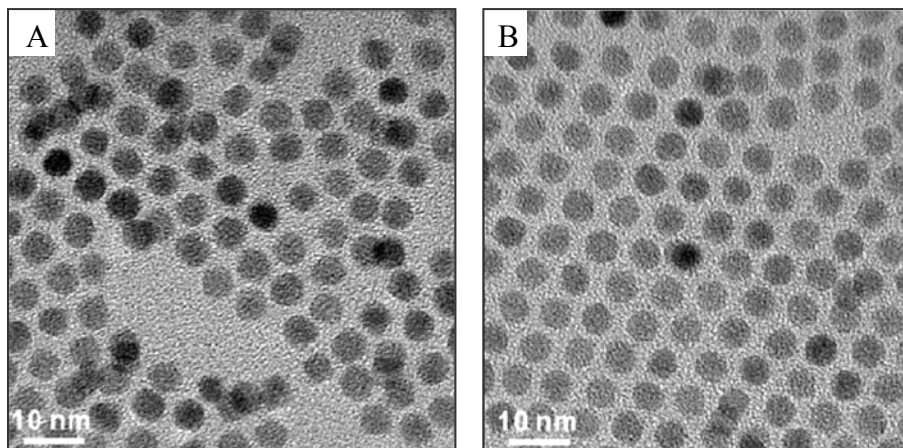


Figure 3-9. TEM measurement of the water effect. A) The particles made in the synthesis with water added; and B) in a typical 5.4-nm- UO_2 synthesis. (Reprinted with permission from ref 142).

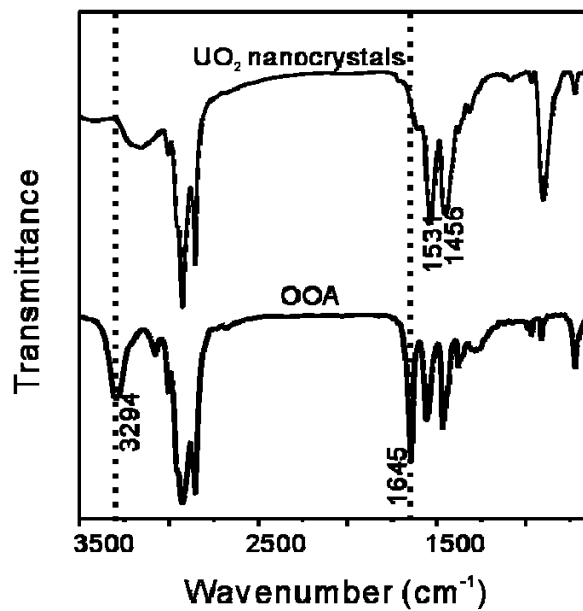


Figure 3-10. IR spectra of purified UO_2 NCs (top) and OOA (bottom). (Reprinted with permission from ref 142)

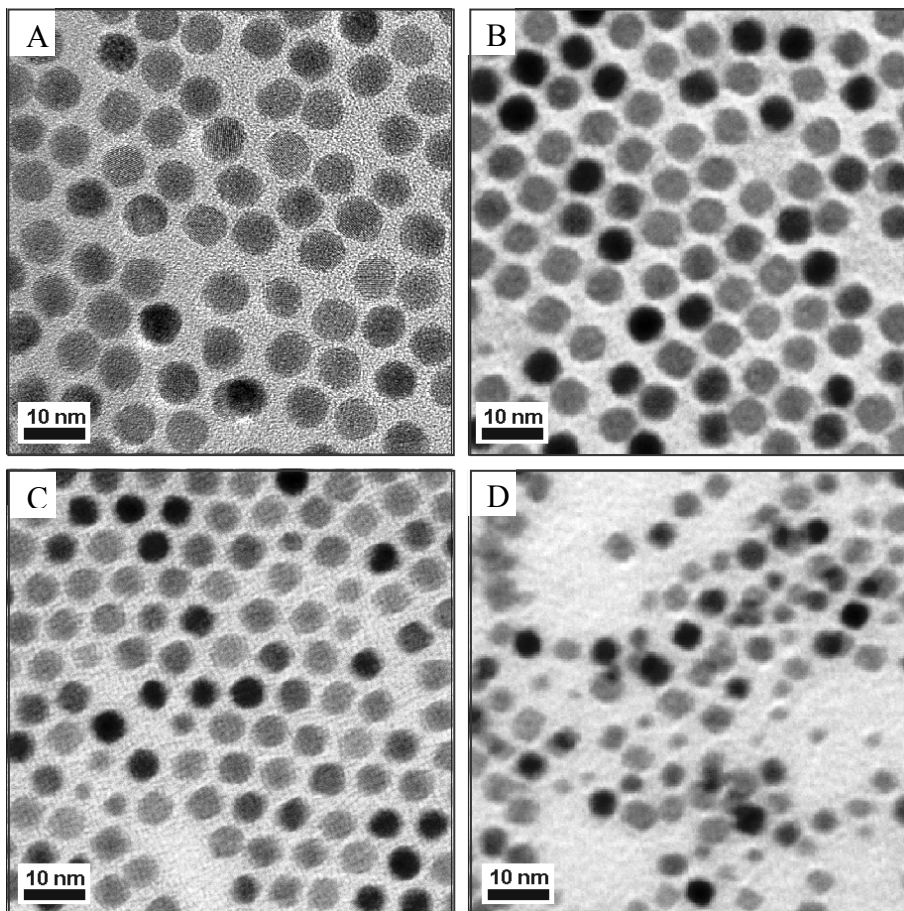


Figure 3-11. TEM measurement of the amide effect. TEM images of UO₂ NCs, synthesized by addition of A) OOA, B) OAT₁, C) OAT₂ and D) OAP.

CHAPTER 4 WATER-SOLUBLE NANOCRYSTALS THROUGH DUAL-INTERACTION LIGANDS

4.1 Introduction

Because of their unique size-dependent optical, electronic, magnetic, and chemical properties, inorganic NCs are becoming powerful tools in biological and medical applications for sensing, labeling, optical imaging, magnetic resonance imaging (MRI), cell separation, and treatment of disease.^[146-148] These applications, however, require NCs that are soluble and stable in aqueous solutions. This creates a need for further engineering of nanocrystal coatings, because high-quality NCs are often synthesized in organic phases and stabilized with hydrophobic ligands.^[46]

To date, two major methods have been developed to modify the coatings of hydrophobic NCs using organic ligands. The first approach is based on coordinate bonding. Functional groups (such as thiol,^[7] dithiol,^[95] phosphine^[20] and dopamine^[149]) are used to link hydrophilic groups directly onto the surface of hydrophobic NCs by replacing the original hydrophobic ligands. The second approach uses hydrophobic van der Waals interactions, through which the hydrophobic tails of amphiphilic ligands interact with (but do not replace) the hydrophobic ligands on the NCs,^[150] leading to the formation of nanocrystal-micelles. Many types of water-soluble NCs made by these two approaches suffer low stability and/or high non-specific binding with non-target biomolecules. Water-soluble NCs coated with PEGylated amphiphilic polymers have very high stability and low nonspecific-adsorption levels,^[95,150] but the PEGylated polymer shells often produce large hydrodynamic diameters (HDs), on the order of 30-40 nm, which can limit the use of these NCs in applications such as *in vivo* cell imaging. Herein, we describe an alternative nanocrystal-surface-engineering approach that uses a new class of ligands (here called dual-interaction ligands) to produce water-soluble NCs. The dual-interaction ligands are based

on Tween-derivatives (TDs), as shown in Figure 4-1. These dual-interaction ligands can bind to the hydrophobic NCs through both coordinate bonding to the inorganic crystal and hydrophobic van der Waals interactions with the non-polar tails of the organic surface ligands.

The dual-interaction ligands are synthesized through simple modifications of Tweens, polyethylene glycol (PEG) sorbitan fatty-acid esters, which all have 20 ethylene-glycol units distributed among their four branches (Figure 4-2). Depending on the length of their fatty-acid tail, these sorbitan fatty-acid esters are commercially named Tween 20, Tween 40, Tween 60 and Tween 80, as shown in Figure 4-2. Because of their low toxicity, these Tween compounds are often used as food additives. More importantly, Tween compounds are widely used as protein stabilizing and blocking agents to minimize non-specific binding in immunoassays such as western blotting and ELISA (enzyme-linked immunosorbent assay). These properties make Tween compounds unique for coating water-soluble NCs for use in biomedical applications. However, the Tween compounds cannot be used directly to stabilize hydrophobic NCs in water because the hydrophobic van der Waals interactions between the Tween fatty-acid tails (R group in Figure 4-2) and the hydrophobic surface ligands are relatively weak. To overcome this difficulty, we have introduced a coordinating functional group via one of the OH-groups. The resulting Tween derivatives (TDs) were expected to have affinity to the surface of hydrophobic NCs through both coordinate bonding and hydrophobic van der Waals interactions.

Two types of coordinating groups were used to functionalize Tween compounds for surface engineering of different types of NCs, as shown in Figure 4-1B. For noble-metal particles and semiconductor QDs, a dithiol coordinating group was introduced into Tween compounds via two steps (Figure 4-2A): (1) attachment of a lipoic-acid group via a mild esterification reaction; and (2) reduction of the product with sodium borohydride to convert the lipoic-acid group into a

dihydrolipoic-acid moiety. The final products are named TD_N-L. For NCs of transition-metal oxides such as Fe₃O₄, a dopamine group was used to modify Tween compounds via a succinic-acid cross-linker in a two-step synthesis (Figure 4-2B): (1) incorporation of a succinic-acid group by an esterification reaction with succinic anhydride, and (2) coupling of a dopamine group with the succinic-acid cross-linker through an EDC (1-ethyl-3-[3-dimethylaminopropyl]carbodiimide hydrochloride)-mediated amide-formation reaction. The reaction sequence yields final products named TD_N-D. Moreover, an additional carboxyl group can be attached onto these TD_N-L compounds, for example, succinic-acid-functionalized TD₂₀-L (TD₂₀-LC, shown in Figure 4-2C). The additional carboxyl group allows protein attachment through a mild EDC-mediated coupling reaction to prepare NC-antibody conjugates. The typical yields of these reactions are higher than 80%. The structures of the resulting TD ligands were confirmed using ¹H-NMR, but the exact positions of the attached functional groups in the TD ligands are not identified.

In this study, water-soluble gold and Fe₃O₄ NCs and CdSe/ZnS quantum dots (QDs) were prepared using dual-interaction ligands with relatively small hydrodynamic diameters (HDs), i.e., less than 20 nm. These NCs exhibit extraordinary stability over in a wide range of pH (e.g. 1-14), salt concentration, and thermal treatment (at 100 °C). In addition, these NCs can be further functionalized with antibodies for monitoring virus-protein expression in cells.

4.2 Experimental Section

4.2.1 Chemicals

Butylamine (99%), dimethylaminopyridine (DMAP, 99%), dopamine hydrochloride, hexamethyl disilathiane ((TMS)₂S), lipoic acid (≥ 99%), 1-methyl-2-pyrrolidinone (NPA, ≥ 99%), *N,N'*-diisopropyl carbodiimide (DIPC, 99%), iron (III) chloride (FeCl₃·6H₂O, 98%), 1-octadecene (ODE, 90%), octadecylamine (ODA, 97%), oleic acid (OA, 90%), *p*-toluenesulfonic acid monohydrate (98%), rhodamine 6G (99%), tributylphosphine (TBP, 97%),

TD₂₀-a: [5-(1,2-Dithiolan-3-yl)-1-oxopentyl]polyethylene glycol sorbitan

monolaurate. Tween-20 (4.91 g, 4.0 mmol), lipoic acid (0.83 g, 4.0 mmol) and DPTS (1.37 g, 4.4 mmol) were mixed in CH₂Cl₂ (20 mL) and stirred for several minutes at room temperature. Then, DIPC (0.63 mL, 4.4 mmol) was added to the mixture. After being stirred at room temperature overnight, the reaction mixture was washed with water (30 mL) four times. The organic phase was dried over magnesium sulfate (MgSO₄), filtered and concentrated. The crude product was purified by column chromatography on silica gel (eluent: ethyl acetate/hexane 9:1 and chloroform/methanol 9:10). Yield: 88%. ¹H-NMR (300 MHz, CDCl₃, Figure 4-3): (ppm) δ_a 0.88 (t, 3H), δ_b 1.25 (m, 16H), δ_c 1.47 (m, 2H), δ_d 1.63 (m, 6H), δ_e 1.90 (m, 1H), δ_f 2.33 (m, 4H), δ_g 2.45 (m, 1H), δ_h 3.13 (m, 3H), δ_i 3.63 (m, 82H), δ_j 4.21 (m, 4H), δ_k 4.56 (m, 2H).

TD₂₀-L: (6,8-Dimercapto-1-oxoocty)polyethylene glycol sorbitan monolaurate.

TD₂₀-a (4.96 g, 3.5 mmol) was dissolved in a mixture of EtOH/water (50 mL, 1:4). Then NaBH₄ (0.23 g, 6.0 mmol) was slowly added. The reaction mixture was stirred for 2 h until the solution became colorless. Then, the solution was diluted with water (50 mL) and extracted with CHCl₃ (50 mL) five times. The combined organic phase was dried over MgSO₄ and filtered. The solvent was removed under reduced pressure to give a white oily product. Yield: 82%. ¹H-NMR (300 MHz, CDCl₃, Figure 4-4): δ_a 0.88 (t, 3H), δ_b 1.24 (m, 16H), δ_c 1.47 (m, 2H), δ_d 1.63 (m, 6H), δ_e 1.90 (m, 1H), δ_f 2.33 (m, 4H), δ_g 2.92 (m, 1H), δ_h 2.70 (m, 3H), δ_i 3.63 (m, 82H), δ_j 4.21 (m, 4H), δ_k 4.56 (m, 2H).

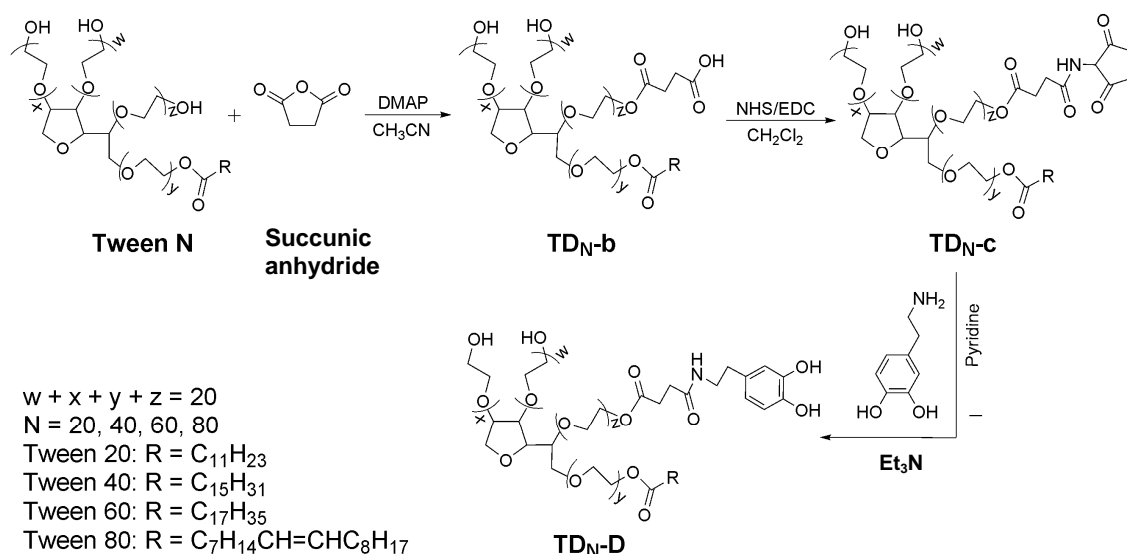
TD₄₀-L: (6,8-Dimercapto-1-oxoocty)polyethylene glycol sorbitan monopalmitate was synthesized using conditions similar to those for the synthesis of TD₂₀-L. ¹H-NMR (300 MHz, CDCl₃): δ (ppm) 0.88 (t, 3H), 1.24 (m, 24H), 1.47 (m, 2H), 1.63 (m, 6H), 1.90 (m, 1H), 2.33 (m, 4H), 2.92 (m, 1H), 2.70 (m, 3H), 3.63 (m, 82H), 4.21 (m, 4H), 4.56 (m, 2H). ¹³C-NMR (100 MHz,

CDCl₃): δ (ppm) 174.06, 173.70, 72.78, 70.79, 70.56, 69.43, 63.67, 63.56, 61.95, 42.98, 39.52, 38.95, 34.43, 34.21, 32.13, 29.90, 29.87, 29.69, 29.57, 29.50, 29.36, 26.72, 25.13, 24.73, 22.90, 22.50, 14.34.

TD₆₀-L: (6,8-Dimercapto-1-oxoocty)polyethylene glycol sorbitan monostearate was synthesized using conditions similar to those for the synthesis of TD₂₀-L. ¹H-NMR (300 MHz, CDCl₃): δ (ppm) 0.88 (t, 3H), 1.24 (m, 28H), 1.47 (m, 2H), 1.63 (m, 6H), 1.90 (m, 1H), 2.33 (m, 4H), 2.70 (m, 3H), 2.92 (m, 1H), 3.63 (m, 82H), 4.21 (m, 4H), 4.56 (m, 2H). ¹³C-NMR (100 MHz, CDCl₃): δ (ppm) 174.06, 173.70, 86.49, 86.21, 82.78, 79.59, 72.78, 71.24, 70.79, 70.56, 69.43, 63.68, 63.56, 61.95, 42.98, 39.52, 38.95, 34.43, 34.21, 32.13, 29.90, 29.87, 29.69, 29.57, 29.50, 29.36, 26.72, 25.13, 24.73, 22.90, 22.50, 14.34.

TD₈₀-L: (6,8-Dimercapto-1-oxoocty)polyethylene glycol sorbitan monooleate was synthesized using conditions similar to those for the synthesis of TD₂₀-L. ¹H-NMR (300 MHz, CDCl₃): δ (ppm) 0.88 (t, 3H), 1.24 (m, 20H), 1.47 (m, 2H), 1.63 (m, 6H), 1.90 (m, 1H), 2.33 (m, 4H), 2.70 (m, 3H), 2.92 (m, 1H), 3.63 (m, 82H), 4.21 (m, 4H), 4.56 (m, 2H), 5.34 (t, 2H).

4.2.2.2 Dopamine-functionalized Tweens (TD_N-D)



Scheme 4-2. Synthetic route to dopamine-functionalized Tweens (TD_N-D)

The synthetic route to dopamine-functionalized Tweens (TD_N-D) is shown in scheme 4-2.

TD₂₀-b: (3-Carboxy-1-oxopropyl)polyethylene glycol sorbitan monolaurate. A mixture of Tween-20 (4.91 g, 4.0 mmol), succinic anhydride (0.41 g, 4.0 mmol) and DMAP (18 mg, 0.15 mmol) in 20 ml of dry acetonitrile was refluxed overnight with stirring. The solution was cooled to room temperature and the solvent was evaporated under reduced pressure. The oily residue was dissolved in CHCl₃ (100 mL) and washed with HCl (1 N, 40 mL) three times and then water (60 mL) three times. The organic phase was dried over MgSO₄ and filtered. The yellow oily product was obtained after removal of the solvent. Yield: 93%. ¹H-NMR (300 MHz, CDCl₃): δ (ppm) 0.88 (t, 3H), 1.25 (m, 16H), 1.60 (m, 2H), 2.32 (t, 2H), 2.63 (s, 4H), 3.63 (m, 82H), 4.23 (m, 4H), 4.57 (m, 2H).

TD₂₀-c: [4-[(2,5-Dioxo-1-pyrrolidinyl)oxy]-1,4-dioxobutyl]polyethylene glycol sorbitan monolaurate. TD₂₀-b (4.85 g, 3.7 mmol) and *N*-hydroxysuccinimide (NHS, 0.43 g, 3.7 mmol) were mixed in CH₂Cl₂ (20 mL). Then EDC (0.71 g, 3.7 mmol) was added. After being stirred at room temperature overnight, the reaction mixture was diluted with CH₂Cl₂ (30 mL).^[S2] This solution was washed with HCl (0.1 N, 60 mL) twice and then brine (60 mL) twice. The organic phase was dried over MgSO₄, filtered and concentrated. The crude product was purified by column chromatography on silica gel (eluent: ethyl acetate/hexane 9:1 and chloroform/methanol 9:1) to give a yellow oily product. Yield: 89%. ¹H-NMR (300 MHz, CDCl₃): δ (ppm) 0.88 (t, 3H), 1.25 (m, 16H), 1.60 (m, 2H), 2.32 (t, 2H), 2.84 (s, 4H), 2.78(t, 2H), 2.97 (t, 2H), 3.63 (m, 82H), 4.26 (m, 4H), 4.57 (m, 2H).

TD₂₀-D: [[[2-(3,4-Dihydroxyphenyl)ethyl]amino]carbonyl]polyethylene glycol sorbitan monolaurate. Dopamine hydrochloride (0.63 g, 3.3 mmol) and triethylamine (0.33 g,

3.3 mmol) were mixed in 1 ml of pyridine. Then the mixture was added to a solution of TD20-c (4.63 g, 3.3 mmol) in pyridine (10 mL). After being stirred for 2 h, the pyridine and solvent were removed under reduced pressure. The oily residue was dissolved in CH₂Cl₂ (20 mL) and the insoluble solid was removed by filtration. The filtered solution was washed with water (30 mL) three times. The organic phase was dried over MgSO₄ and filtered. A dark yellow oily product was obtained after evaporation of the solvent. Yield: 90 %. ¹H-NMR (300 MHz, CDCl₃): δ (ppm) 0.88 (t, 3H), δ_b 1.25 (m, 16H), 1.62 (m, 2H), 2.33 (m, 2H), 2.43 (t, 2H), 2.84 (m, 4H), 3.435 (t, 2H), 3.64 (m, 84H), 4.21 (m, 4H), 4.56 (m, 2H), 6.55 (d, 1H), 6.70 (s, 1H) and 6.79 (d, 1H).

TD₄₀-D: [[[2-(3,4-Dyhydroxyphenyl)ethyl]amino]carbonyl]polyethylene glycol sorbitan monopalmitate was synthesized using conditions similar to those for the synthesis of TD₂₀-D. ¹H-NMR (300 MHz, CDCl₃): δ (ppm) 0.88 (t, 3H), 1.25 (m, 24H), 1.62 (m, 2H), 2.33 (m, 2H), 2.43 (t, 2H), 2.84 (m, 4H), 3.43 (t, 4H), 3.64 (m, 84H), 4.21 (m, 4H), 4.56 (m, 2H), 6.55 (d, 1H), 6.70 (s, 1H) and 6.79 (d, 1H).

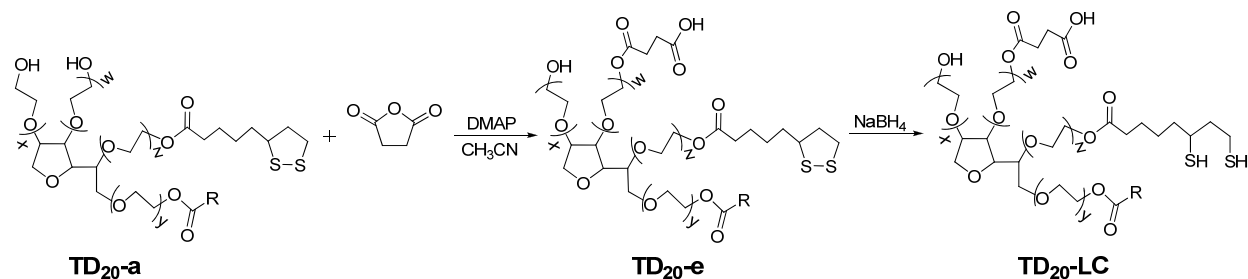
TD₆₀-D: [[[2-(3,4-Dyhydroxyphenyl)ethyl]amino]carbonyl]polyethylene glycol sorbitan monostearate was synthesized using conditions similar to those for the synthesis of TD₂₀-D. ¹H-NMR (300 MHz, CDCl₃): δ (ppm) 0.88 (t, 3H), 1.25 (m, 26H), (m, 2H), 2.33 (m, 2H), 2.43 (t, 2H), 2.84 (m, 4H), 3.43 (t, 4H), 3.64 (m, 84H), 4.21 (m, 4H), 4.56 (m, 2H), 6.55 (d, 1H), 6.70 (s, 1H) and 6.79 (d, 1H).

TD₈₀-D: [[[2-(3,4-Dyhydroxyphenyl)ethyl]amino]carbonyl]polyethylene glycol sorbitan monostearate. was synthesized using conditions similar to those for the synthesis of TD₂₀-D. ¹H-NMR (300 MHz, CDCl₃): δ (ppm) 0.88 (t, 3H), 1.25 (m, 20H), 1.62 (m, 2H), 1.99

(m, 4H), 2.33 (m, 2H), 2.43 (t, 2H), 2.84 (m, 4H), 3.43(t, 4H), 3.64 (m, 84H), 4.21 (m, 4H), 4.56 (m, 2H), 5.34 (t, 2H), 6.55 (d, 1H), 6.70 (s, 1H) and 6.79 (d, 1H).

4.2.2.3 Carboxyl-group-functionalized TD₂₀-L (TD₂₀-LC)

The synthetic route to carboxyl-group-functionalized TD₂₀-L (TD₂₀-LC) is shown in scheme 4-3.



Scheme 4-3. Synthetic route to carboxyl-group-functionalized TD₂₀-L (TD₂₀-LC)

TD₂₀-e: α-[5-(1,2-Dithiolan-3-yl)-1-oxopentyl]-ω-(3-carboxy-1-oxopropyl) polyethylene glycol sorbitan monolaurate. A mixture of TD₂₀-a (4.96 g, 3.5 mmol), succinic anhydride (0.36 g, 3.5 mmol) and DMAP (18 mg, 0.15 mmol) in dry acetonitrile (20 mL) was refluxed overnight with stirring. The solution was cooled to room temperature, and the solvent was evaporated under reduced pressure. The oily residue was dissolved in CHCl₃ (10 mL) and washed with HCl solution (1 N, 40 mL) twice and with water (50 mL) twice. The organic phase was dried over MgSO₄ and filtered. The yellow oily product was obtained after evaporation of the solvent. Yield: 98%. ¹H-NMR (300 MHz, CDCl₃): δ (ppm) 0.88 (t, 3H), 1.24 (m, 16H), 1.46 (m, 2H), 1.63 (m, 6H), 1.90 (m, 1H), 2.32 (m, 4H), 2.45 (m, 1H), 2.65 (m, 4H), 3.13 (m, 3H), 3.63 (m, 82H), 4.21 (m, 6H), 4.56 (m, 2H).

TD₂₀-LC: α-[5-(1,2-Dithiolan-3-yl)-1-oxopentyl]-ω-(6,8-dimercapto-1-oxooctyl)-polyethylene glycol sorbitan monolaurate. TD₂₀-e (5.14 g, 3.4 mmol) in NaHCO₃ aqueous solution (0.25 M, 100 mL) was cooled with an ice bath for 5 minutes. Then NaBH₄ (0.53 g, 14

mmol) was added slowly. The reaction mixture was stirred for 2 h until the reaction mixture turned colorless. Then, HCl (6 N, 10 mL) was added to quench the reaction. The mixture was extracted with CHCl₃ (50 mL) five times. The combined organic solution was dried over MgSO₄ and filtered. A white oily product was obtained after evaporation of the solvent. Yield: 92%. ¹H-NMR (300 MHz, CDCl₃): δ (ppm) 0.88 (t, 3H), 1.24 (m, 16H), 1.47 (m, 2H), 1.63 (m, 6H), 1.90 (m, 1H), 2.33 (m, 4H), 2.92 (m, 1H), 2.65 (m, 4H), 2.70 (m, 3H), 3.63 (m, 82H), 4.21 (m, 6H), 4.56 (m, 2H).

4.2.3 Gold, Fe₃O₄ and CdSe/ZnS Nanocrystal Synthesis

1-Dodecanethiol-capped 6.6-nm gold NCs were synthesized according to the literature procedure.^[54] In a typical synthesis, AuCl₃ (0.068 g) was dissolved in a DTAB solution (0.185 g of DTAB in 20 ml of toluene) with ultrasonication to form a dark orange solution. Then a freshly prepared aqueous solution of NaBH₄ (75 μmol) was added dropwise to the solution with vigorous stirring. After 20 minutes, 1-dodecanethiol (1.6 mL) was added and the stirring was continued for 10 minutes. The NCs were precipitated by adding ethanol, and the solid was re-dispersed in toluene (20 mL) in the presence of 1-dodecanethiol (1.6 mL) and refluxed for 30 minutes under nitrogen. The NCs were precipitated from the reaction solution with ethanol (30 mL), isolated by centrifugation, and re-dispersed in CHCl₃. The resulting NCs have a diameter of 6.6 nm with a standard deviation of 7.0 %.

Oleic-acid-capped 5.8-nm Fe₃O₄ NCs were synthesized according to the literature method.^[55]

Oleylamine-capped 5.6-nm CdSe/ZnS core/shell NCs. CdSe/ZnS core/shell NCs were prepared by a two-step procedure consisting of synthesis of CdSe core NCs^[152] and growth of ZnS layers. The syntheses were conducted according to the literature method.^[153]

4.2.4 Preparation of TD-capped Water-soluble NCs

Hydrophobic NCs (i.e., Au, Fe₃O₄ or CdSe/ZnS) (5 μM) and TDs (e.g., TD_N-L, TD_N-D or TD₂₀-LC) (10 μmol) were mixed in CHCl₃ (5 mL). The solution was stirred at room temperature for 10 minutes. Then triethylamine (0.05 mL) was added to the mixture. The resulting mixture was stirred further for 10 minutes. After evaporation of the solvent, the NCs were re-dispersed in water. The nanocrystal solution was filtered through a 0.22-μm MCE syringe filter (Fisher Scientific). The excess of TD ligands was removed by spin filtration (Millipore, 10K NMWL, 10000×g, 10 min) four times. The resulting NCs were re-dispersed in water (18 Ω) for further studies.

4.2.5 Antibody-functionalized CdSe/ZnS Nanocrystals

Hydrophilic CdSe/ZnS QDs with a diameter of 5.6 nm (RSD ~ 8.0 %) and capped with a mixture of compound TD₂₀-L and TD₂₀-LC (5:1 molar ratio) were prepared as described above. CdSe/ZnS QDs (0.20 nmol) were dissolved in 2-(*N*-morpholino)ethanesulfonic-acid buffer solution (MES buffer, 0.1 M, 150 μL, pH = 6.0). An aqueous solution of 1-ethyl-3-(3-dimethylaminopropyl)carbodiimide (EDC, 5.0 mg/mL, 50 μL) and an aqueous solution of *N*-hydroxysulfosuccinimide (Sulfo-NHS, 5.0 mg/mL, 50 μL) were added to the QD-buffer solution. The mixture solution was incubated for 1 h at room temperature with gentle shaking. Then, 2-mercaptoethanol (1.0 μL) was added to the reaction mixture to quench the EDC. The excess reducing agent and inactivated cross-linker were removed by filtering through a NAP-5 column using phosphate buffered saline (PBS buffer, pH = 7.4) as the elution buffer. The collected QD solution was concentrated to 50 μL by spin filtration (10K NMWL, Millipore, 10000×g, 10 min) and re-dissolved in PBS buffer solution (250 μL, pH 7.4). NS5A-specific mouse monoclonal antibody (100 μg) was added to the QD solution, and the resulting mixture was incubated for 2hr at room temperature. Hydroxylamine (0.5 μL) was added to quench the

reaction. The mixture was transferred to a spin filter (100K NMWL, Millipore, 10000×g, 10 min) and concentrated to 50 μL. Then PBS buffer solution (200 μL, pH 7.4) was added and the mixture was spun again. The washing step was repeated 2 times to remove thoroughly the free antibodies. Finally, the purified antibody-functionalized QDs (0.15 nmol) were re-dispersed in a PBS buffer solution (450 μL, pH 7.4). Sodium azide was added to the solution of antibody-conjugated QDs (with a concentration of 0.01 % w/v) as a preservative.

4.2.6 Immunoassay Tests

FCA1 HCV replicon cells were grown on glass coverslips for 24 h, and the cells were fixed in an ethanol solution with 5% acetic acid at -20 °C overnight. The fixed cells were washed with PBS (pH 7.4) at room temperature twice (5 minutes each time), and the cells were blocked by 1:50 normal goat serum for 30 min at room temperature. Then the cells were incubated with NS5A-specific-antibody functionalized QDs (50 nM, 0.20 mL) at room temperature for 1 h. After the cells were washed with PBS (pH 7.4) 3 times (5 minutes each), the nuclei of the cells were counterstained with DAPI (4',6-diamidino-2-phenylindole, Vector Laboratories Inc, Burlingame, CA) as an internal reference, and the extra DAPI was removed with PBS (pH 7.4). Finally, the FCA1 cells were examined under a fluorescence microscope (Olympus BX51, Olympus Imaging America Inc, Center Valley, PA).

In a control test, TD-capped QDs (with the ratio of TD₈₀-L: TD₂₀-LC = 5:1), which were not functionalized with NS5A-specific antibody, were used for staining FCA1 cells.

Histograms of fluorescent images show the mean pixel intensities. The intensity ratio of blue channel (from DAPI) and red channel (from QDs) was calculated for each cell, and more than 300 cells were analyzed.

4.2.7 Stability Tests

Each stability test was repeated more than five times using the same batch of TD-capped NCs. The sample standard deviation (S) and relative standard deviation (RSD) were calculated by the following equations, respectively:

$$S = \sqrt{\frac{1}{N-1} \sum_{i=1}^N (x_i - \bar{x})^2} ; \text{ and } \text{RSD} = S / \bar{x}$$

where x_i is the result of each experiment and \bar{x} is the average value.

For example, five sets of dynamic light scattering (DLS) data (Figure 4-5) were obtained from five parallel stability-test experiments. The nanocrystal hydrodynamic size in each experiment is Figure 4-5A) 16.3 nm, B) 17.8 nm, C) 17.1 nm, D) 17.3 nm and E) 17.0 nm. So the average size of these five experiments was $17.1 \text{ nm} \pm 0.54 \text{ nm}$ and $\text{RSD} = 3.2\%$, as calculated by the above equations.

4.2.8 Other Measurements

4.2.8.1 $^1\text{H-NMR}$ Measurements

$^1\text{H-NMR}$ spectra were recorded using a Varian Mercury NMR Spectrometer (300 MHz). The samples were prepared by adding aliquots of products (10 mg) to deuterated chloroform (CDCl_3 , $\sim 0.6 \text{ mL}$).

4.2.8.2 Determination of Fluorescence Quantum Yields (QY)

Fluorescence spectra were measured using a Fluorolog-3 spectrofluorometer (Horiba Jobin Yvon, Irvine, CA). Room-temperature fluorescence QY of the CdSe/ZnS core/shell QDs was determined using the literature method.^[58] LD690 (63% QY) was used as reference and the excitation wavelength was 500 nm.

4.2.8.3 DLS Measurements

The nanocrystal aqueous solutions were first filtered through a 0.22- μm MCE syringe filter (Fisher Scientific). The hydrodynamic sizes of NCs were obtained using a Brookhaven Instruments dynamic light scattering instrument (DLS) (Corporation, Holtsville, NY) at 25 °C.

4.2.8.4 TEM Measurements

TEM measurements were performed on a JEOL 200CX operated at 200 kV. To prepare the specimens, a particle solution (10 μL) was dropped onto a 200-mesh copper grid, and dried overnight at ambient conditions.

4.3 Results and Discussion

To examine the function of these TD ligands, three types of hydrophobic NCs were used: gold NCs (6.6 nm in diameter with RSD 7.0 %), Fe_3O_4 (5.8 nm in diameter with σ of 6.0%), and CdSe/ZnS QDs (5.6 nm in diameter with RSD of 8.0%) (Figure 4-6A-C). In the first set of experiments, TD₂₀-L (or TD₂₀-D) was used to functionalize the gold and CdSe/ZnS (or Fe_3O_4) NCs, respectively. The ligand-exchange reactions were performed in chloroform for 20 min. After evaporation of the chloroform, the resulting hydrophilic NCs are highly soluble in water, with a transfer yield of nearly 100%. The extra ligands in the hydrophilic-nanocrystal solutions were removed by spin filtration four times.

TEM measurements show that the TD-functionalized hydrophilic NCs exhibit nearly identical size and shape, as compared to their hydrophobic counterparts (Figure 4-6D-F). Dynamic light scattering (DLS) measurements show that the HDs of these NCs are 17.1 nm for the TD₂₀-L-functionalized Au particles, 16.3 nm for the TD₂₀-D-functionalized Fe_3O_4 NCs, and 15.9 nm for the TD₂₀-L-functionalized CdSe/ZnSe QDs (Figure 4-6G-I). After subtracting the respective core sizes from the HDs, we obtain a nearly identical shell thickness of about 5.2 nm for all three types of NCs. The shell thickness is very close to the average length of these TD

ligands (~4.9 nm). This result shows that only one monolayer of TD ligands is functionalized onto the nanocrystal surface. In addition, gas-chromatography-mass spectrometry (GC-MS) measurements show that these TD ligands do not totally remove the original hydrophobic ligands of these NCs. In a sample of TD₂₀-D-functionalized Fe₃O₄ NCs, oleic acid (the original ligand) was unambiguously identified by GC-MS (Figure 4-7).

Taken together with the results above, this partial ligand exchange suggests that TD ligands indeed functionalize hydrophobic NCs through both coordinate bonding, as well as via hydrophobic van der Waals interactions between the fatty-acid chain in the TD ligands and the hydrophobic ligands on the NCs. This nanocrystal functionalization with dual-interaction ligands is further consistent with the results from the following nanocrystal-stability measurements.

The stability of the hydrophilic NCs was investigated as a function of pH, salt concentration and time of a thermal treatment at 100 °C. For the TD₂₀-L-functionalized gold NCs, the stability tests were monitored using both LDS and UV-Vis absorption spectroscopy, as shown in Figure 4-8. In boiling water (pH 6.5) for 4 h, these gold NCs do not exhibit significant change in their hydrodynamic diameters (HD), as measured using LDS, or in the position of their absorption peak, as measured by absorption spectroscopy (Figure 4-9A). The results from pH-stability tests (Figure 4-9B) show that these hydrophilic gold NCs are stable from pH 2 to 13 for more than one week. At pH 1, the HD of these particles is slightly decreased, but without a change in the position of absorption maxima for more than two hours. At pH 14, the particles show small changes in both HD and absorption-peak position, but the nanocrystal solution is stable for more than three days at this condition. In addition, the gold NCs are stable almost indefinitely in NaCl solutions with concentrations up to 5 M (Figure 4-9C). Altogether, these results show that TD₂₀-L-functionalized gold NCs exhibit extraordinary stability in various

extreme conditions. Such stability is even higher than that of gold NCs heavily functionalized with alkylthiol-capped oligonucleotides, which have been used in commercial biomedical diagnosis because of their high stability in high-concentration salt solutions.

The TD₂₀-D-functionalized Fe₃O₄ NCs also exhibit excellent stability in these tests. These Fe₃O₄ NCs are stable in a solution of boiling water (pH 6.5) for 3 h (Figure 4-9D). pH-stability tests show that these Fe₃O₄ NCs are stable from pH 3 to 14 for more than one week. At pH 2, the HD of these Fe₃O₄ NCs slightly increases (Figure 4-9E). Surprisingly, TEM measurements show that after a 2hr treatment at pH 2 the NCs exhibit no measurable change in size and shape, as compared with the NCs in the control experiment at pH 7 (Figure 4-10). Moreover, the TD₂₀-D-modified Fe₃O₄ NCs are stable nearly in NaCl solutions with concentrations up to 2 M. In a 4-M NaCl solution, these Fe₃O₄ NCs are stable for more than 4 h (Figure 4-9F). These results show that TD₂₀-D-functionalized Fe₃O₄ NCs exhibit a much higher stability than Fe₃O₄ NCs functionalized with PEGylated-dopamine ligands, which attach onto the nanocrystal surface through coordinate bonding only.^[154] Therefore, the excellent stability of TD-functionalized hydrophilic NCs may be attributed to the ability of the TD ligands to bind to the nanocrystal surface via both coordinate bonding and hydrophobic interactions.

Figure 4-11 shows four different colors of TD₂₀-L capped CdSe/ZnS NCs in aqueous solution. These NCs are very bright under a UV-lamp. The absorption spectra and emission spectra of these NCs are shown in Figure 4-11C and D. To compare the stability of TL₂₀-L-capped NCs with the other ligands, the same CdSe/ZnS NCs were used, but the ligands on the NC surfaces were different. Table 4-1 lists the results of transfer efficiency of ligand exchange, hydrodynamic size measured by DLS, and the stability test of these NCs. It clearly shows that TD₂₀-L functionalized CdSe/ZnS NCs are relatively small but stable NCs.

To further explore the effect of the hydrophobic van der Waals interactions between TD ligands and the nanocrystal hydrophobic coating, the stability of TD_N-L-functionalized CdSe/ZnS QDs was studied as a function of the fatty-acid chain in the TD_N-L ligands (N = 20, 40, 60 or 80). In these experiments, 5.6-nm oleylamine-coated CdSe/ZnS particles were transferred into the aqueous phase through surface functionalization with the four types of TD_N-L ligands. The resulting TD₂₀-L-modified CdSe/ZnS NCs were stable from pH 3.5 to 11 (Figure 4-12A). Such stability is higher than that of CdSe/ZnS particles functionalized with PEGylated-lipoic-acid ligands, which lack hydrophobic interactions with the nanocrystal surface.^[95] When the length of the fatty-acid chain was increased to C16 and C18, TD_N-L-modified CdSe/ZnS NCs (N = 40, 60, or 80) are stable in a wider pH range, from 1 to 14, according to DLS measurements (Figure 4-12A). Such the fatty-acid-chain-dependent stability is also observed in the stability tests with NaCl solutions. TD₂₀-L-modified particles are stable in NaCl solutions only up to 0.6 M, while TD₄₀-L-modified particles are stable in a 2-M NaCl solution. With a further increase of fatty-acid length to C18, TD₈₀-L- (or TD₆₀-L)-functionalized CdSe/ZnS NCs are stable in a nearly saturated NaCl solution (Figure 4-12B). Taken together, these results demonstrate that the stability of NCs indeed depends on the length of the fatty-acid chains on the TD ligands.

This chain-length-dependent stability suggests that the van der Waals interactions between the fatty-acid chains and the oleylamine coating play a significant role in stabilizing NCs in aqueous solutions. The longer the fatty-acid chain, the greater the van der Waals interactions with the oleylamine coating. In addition, the van der Waals interactions should create a hydrophobic shell on the nanocrystal surface. Such a hydrophobic shell can provide additional protection for the hydrophilic NCs by preventing hydrophilic reagents (such as H⁺)

from reacting with the nanocrystal surface. Indeed, we have found that the fluorescence quantum yield of TD₈₀-L-functionalized CdSe/ZnS QDs is maintained at about 50% for more than three months in aqueous solutions between pHs 3.5 and 12.5. Furthermore, the fluorescence brightness of these NCs does not significantly change for 2 hours in an aqueous solution of pH 2 (Figure 4-12C).

To demonstrate the suitability of using these water-soluble NCs for biomedical diagnosis, TD-modified CdSe/ZnS QDs were used as fluorescence labels to monitor the expression of a HCV (Hepatitis C virus) protein (NS5A) inside FCA1 cells. In these experiments, 5.6-nm oleylamine-capped CdSe/ZnS QDs were first functionalized with a mixture of TD₈₀-L and TD₂₀-LC (5:1). Anti-HCV NS5A monoclonal antibodies were then attached onto the resulting QDs through an EDC coupling reaction. In a control test, the QDs without NS5A-specific antibodies showed very low non-specific adsorption onto NS5A-containing FCA1-cell substrates (Figure 4-13A). In contrast, the antibody-modified QDs exhibit a very high specific affinity to such substrates (Figure 4-13B). Significantly, the fluorescence intensity from QDs labels is more than 75 times stronger than that in the control test (Figure 4-13C).

4.4 Conclusion

Dual-interaction ligands were successfully used to convert hydrophobic gold, Fe₃O₄ and CdSe/ZnS NCs into hydrophilic NCs. A series of dual-interaction ligands was synthesized through simple modifications of Tween compounds. The hydrophilic NCs functionalized with these TD ligands exhibit high stability in aqueous solutions with a wide range of pH and salt concentration, and under thermal treatment at 100 °C. Such extraordinary nanocrystal stability is attributed to the new type of surface functionalization through both coordinate bonding and hydrophobic van der Waals interactions. In addition, the TD-functionalized QDs are excellent fluorescent labels for detecting the HCV-NS5A expression in FCA1 cells. Moreover, the new

surface-functionalization approach can be readily generalized for NCs with other compositions. Finally, because of their excellent stability, these TD-functionalized NCs should play an important role in a variety of nanocrystal-based biomedical applications.

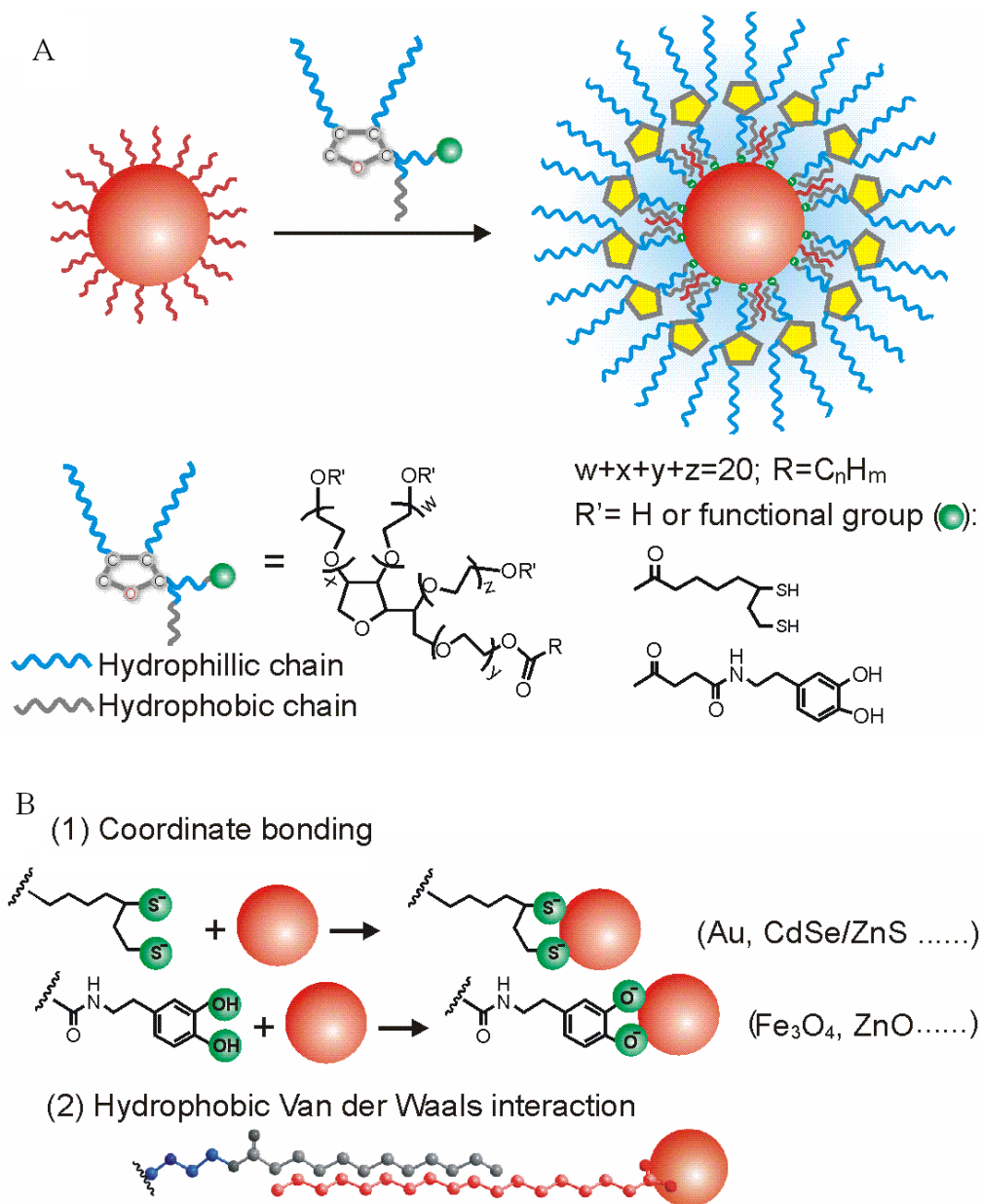


Figure 4-1. Schematic illustration of the Tween-derivatives (TDs) dual interaction. A) The molecular structure of Tween-derivatives. B) The dual interactions: coordinate bonding to the inorganic crystal and hydrophobic van der Waals interaction with the non-polar tails of the organic surface ligands. Dithiol group coordinates with Au and semiconductor QDs and diphenol group has strong interaction with metal oxide NCs. (Reprinted with permission from ref 151).

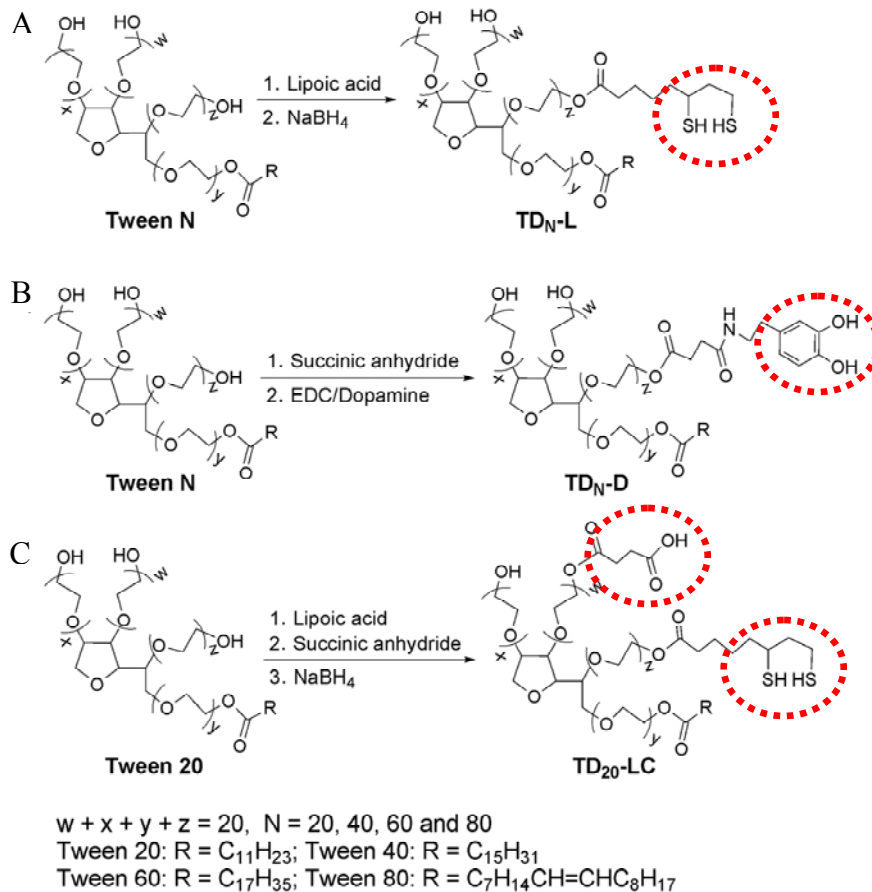


Figure 4-2. Synthesis of dual-interaction TD ligands: A) lipioic-acid-functionalized TDs; B) dopamine-functionalized TDs, and C) carboxyl-group-functionalized TD₂₀-L. In this study, water-soluble gold, Fe₃O₄ NCs and CdSe/ZnS quantum dots (QDs) functionalized with dual interaction ligands were prepared with relatively small hydrodynamic diameters (e.g., less than 20 nm). These NCs exhibit extraordinary stability over in a wide range of pH (e.g., 1-14), salt concentration, and thermal treatment (at 100 °C). In addition, these NCs can be further functionalized with antibodies for monitoring virus-protein expression in cells. (Reprinted with permission from ref 151).

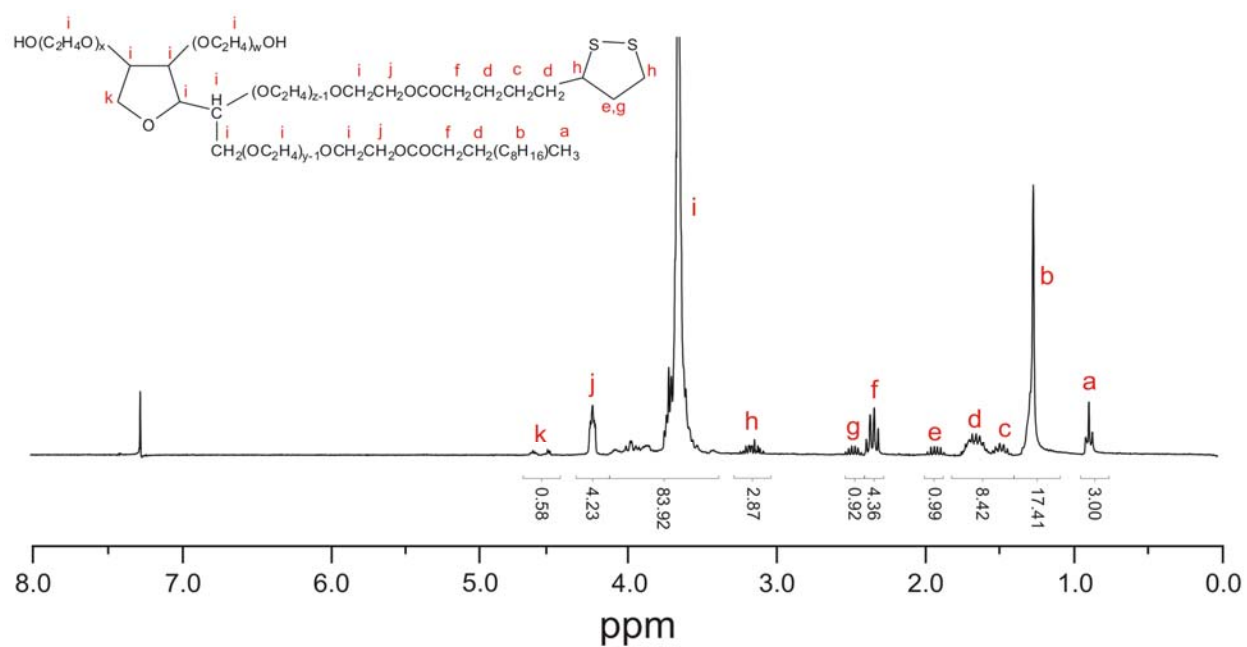


Figure 4-3. ¹H-NMR of compound TD₂₀-a

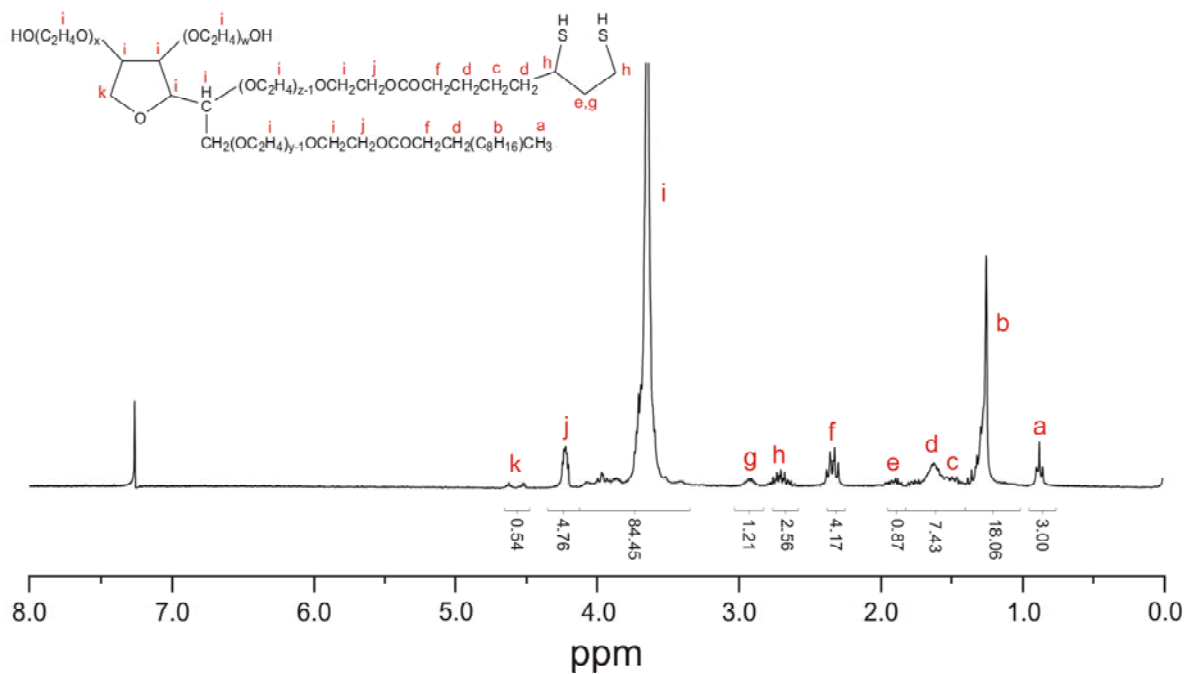


Figure 4-4. ¹H-NMR of compound TD₂₀-L

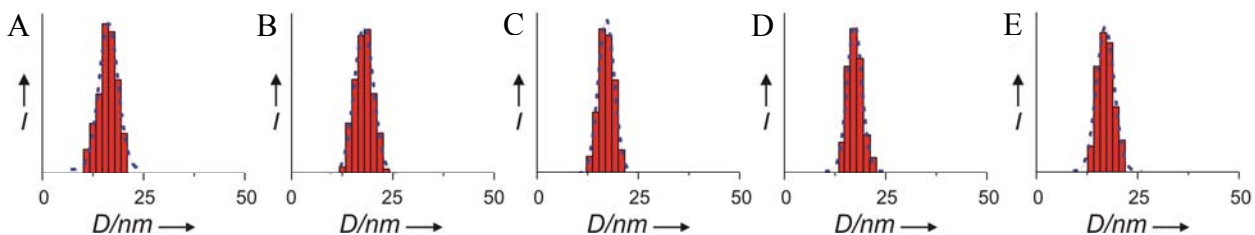


Figure 4-5. DLS data for TD₂₀-L-functionalized 6.6-nm Au NCs from five parallel thermal-stability-test experiments (at 100 °C and pH 6.5 for 120 min). (Reprinted with permission from ref 151).

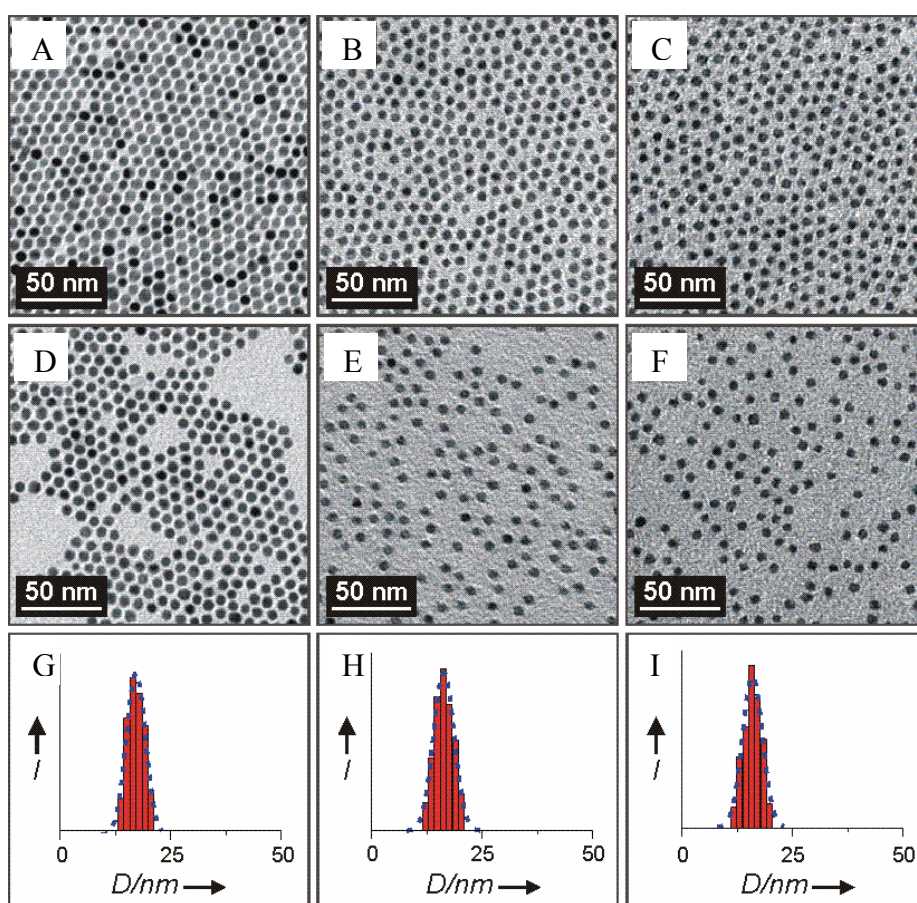


Figure 4-6. TEM images of hydrophobic NCs: A) 6.6-nm Au, B) 5.8-nm Fe₃O₄ and C) 5.6-nm CdSe/ZnS core/shell NCs prior to functionalization; and their hydrophilic counterparts functionalized with TD₂₀ ligands: D) Au NCs/TD₂₀-L, E) Fe₃O₄ NCs / TD₂₀-D and F) CdSe/ZnS QDs/TD₂₀-L. Dynamic light scattering spectra of these hydrophilic NCs: G) Au NCs/TD₂₀-L, (h) Fe₃O₄ NCs/TD₂₀-D and I) CdSe/ZnS QDs / TD₂₀-L. (Reprinted with permission from ref 151)

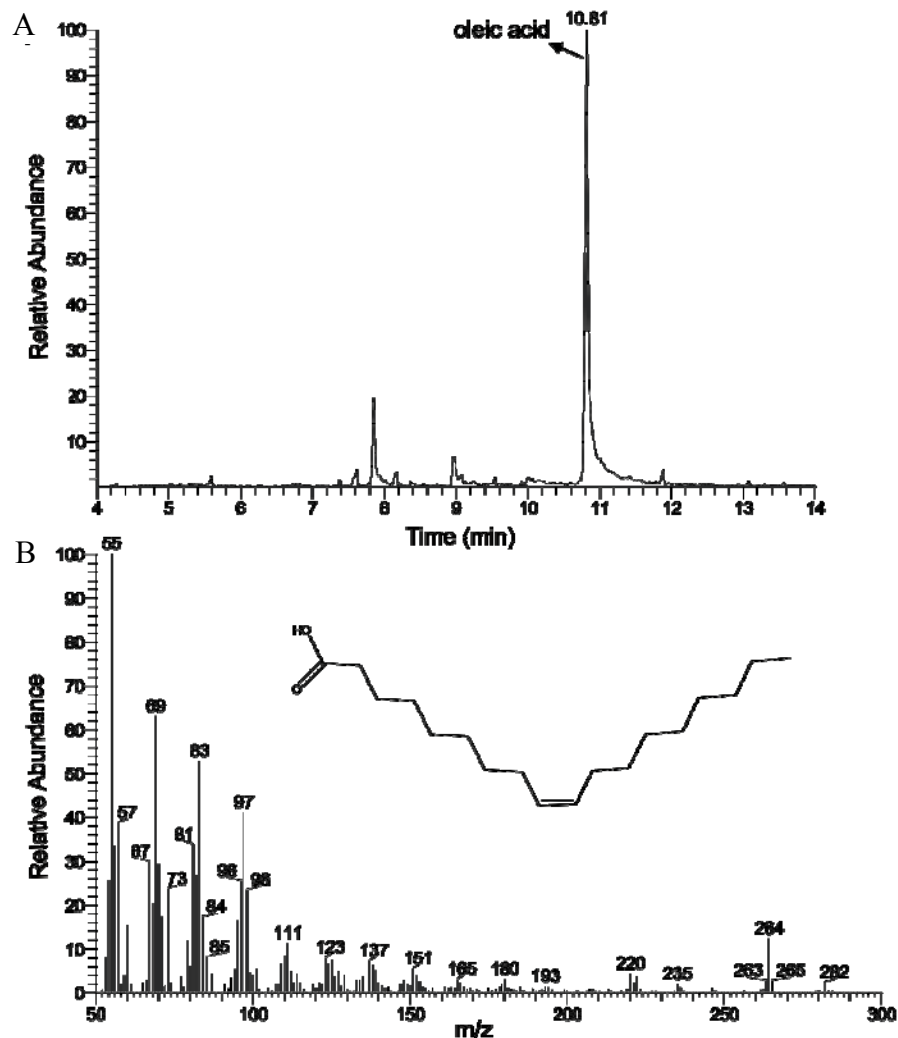


Figure 4-7. Gas-chromatography mass spectrometry (GC-MS): A) a gas chromatogram of a solution with the ligands from TD₂₀-D-functionalized Fe₂O₃ NCs; and B) a mass spectrum of the compound with a retention time of 10.81 min. This spectrum is nearly identical to the standard mass spectrum of oleic acid. The sample was prepared as follows: TD₂₀-D-functionalized Fe₂O₃ NCs (~15 mg) were dissolved by HCl (10 M, 1 mL), and then water and excess HCl were evaporated from the solution using a rotary evaporator. The resulting yellow, oily residue was dissolved in methanol (1 mL) for the GC-MS measurements. (Reprinted with permission from ref 151).

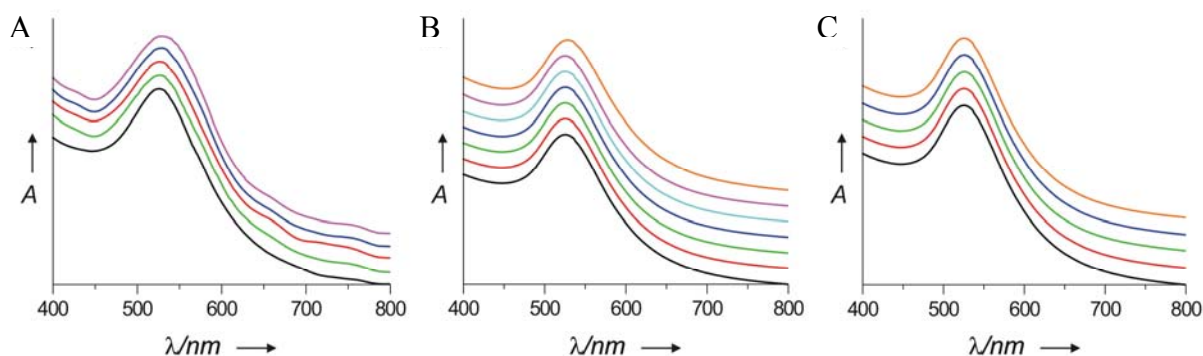


Figure 4-8. UV-Vis spectra for the stability tests of TD₂₀-L-functionalized Au NCs: A) thermal stability test at 100 °C as a function of time: Black: 0 h, Red: 1 h, Green: 2 h, Blue: 3 h and Magenta: 4 h; B) stability as a function of pH: Black: pH 1; Red: pH 2, Green: pH 3, Blue: pH 7, Cyan: pH 12, Magenta: pH 13 and Orange: pH 14; C) stability as a function of NaCl concentration. Black: 0 M, Red: 1 M, Green: 2 M, Blue: 3.5 M and Orange: 5 M. (Reprinted with permission from ref 151).

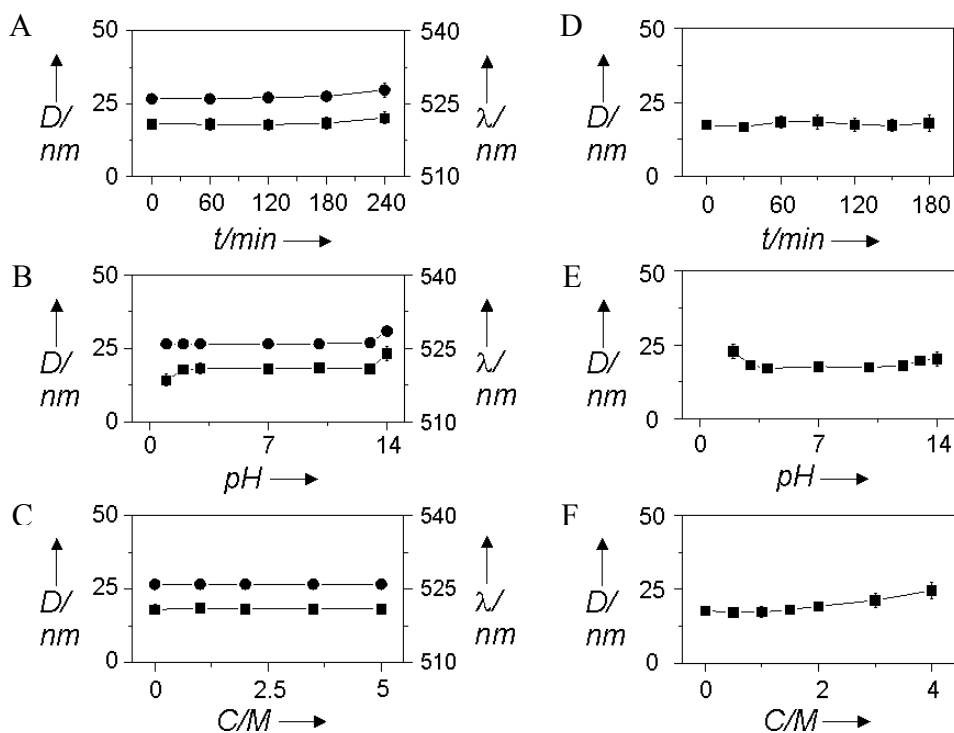


Figure 4-9. Stability tests of TD₂₀-L-functionalized 6.6-nm Au NCs monitored with DLS (black) and UV-Vis spectra (Red): A) Thermal-stability test at 100 °C; B) pH-stability test; and C) stability as a function of NaCl concentration. D), E) and F) are the respective stability tests for TD₂₀-D-functionalized 5.8-nm Fe₃O₄ NCs. (Reprinted with permission from ref 151).

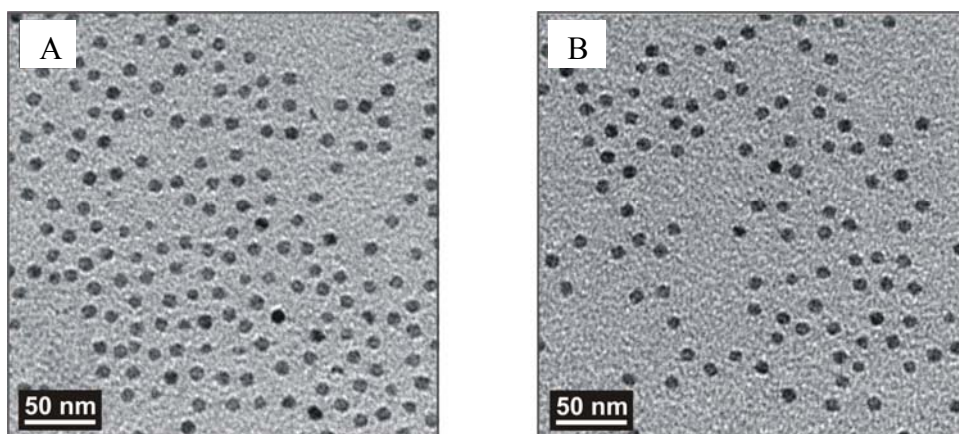


Figure 4-10. TEM images of TD₂₀-D-capped Fe₃O₄ NCs from aqueous solutions at A) pH 7 and B) pH 2 for 2h(Reprinted with permission from ref 151).

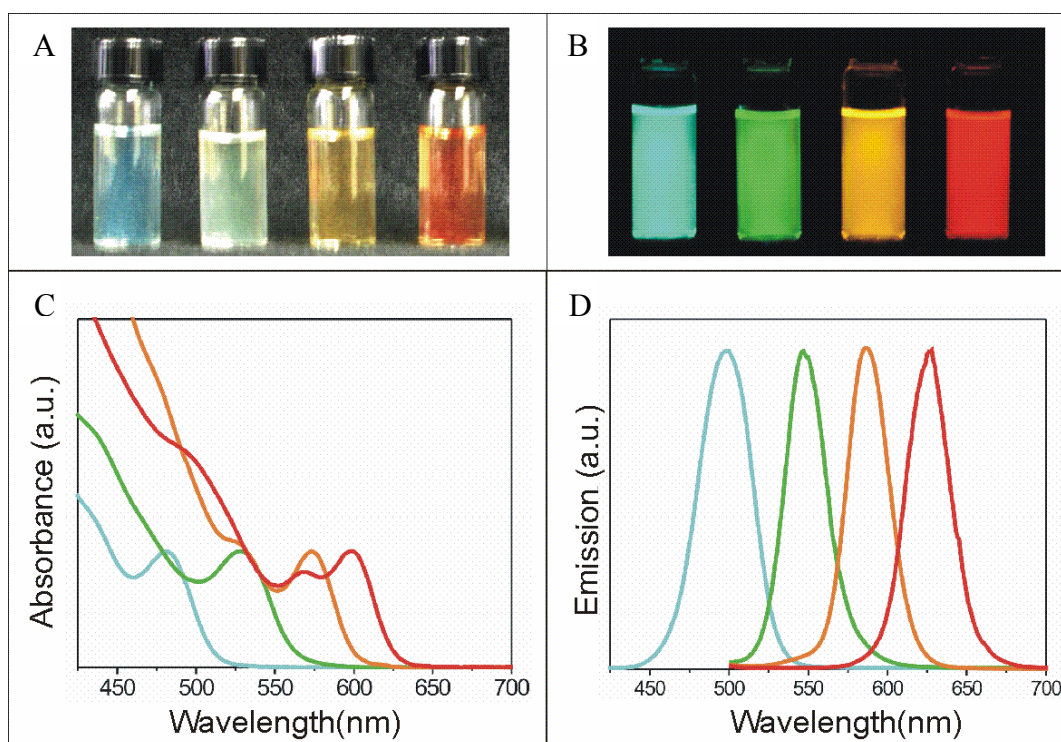


Figure 4-11. TD₂₀-L capped CdSe/ZnS NCs with different sizes in aqueous solution. A) Photo image and B) fluorescence image, C) absorption spectra and D) emission spectra.

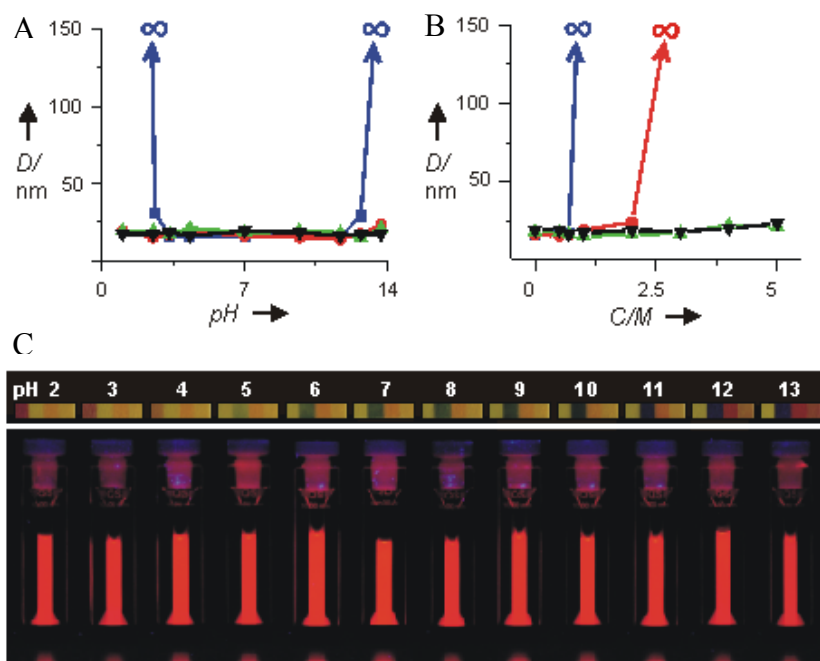


Figure 4-12. Stability tests of TD_N-L-functionalized 5.6-nm CdSe/ZnS NCs as a function of the fatty-acid chain on these TD ligands A) pH and B) NaCl: TD₂₀-L (blue square); TD₄₀-L (red dot); TD₆₀-L (green triangle up); and TD₈₀-L (black triangle down). C) Fluorescence images of TD₈₀-L-functionalized 5.6-nm CdSe/ZnS NCs as a function of pH, which was indicated by pH-test paper.

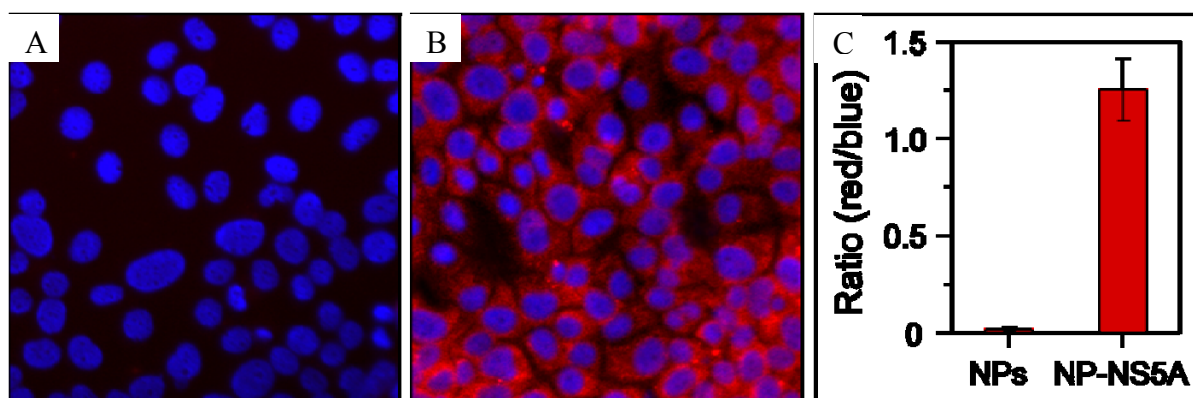


Figure 4-13. Immunofluorescence tests of NS5A-containing FCA1 cells using TD-functionalized CdSe/ZnS core/shell nanocrystal QDs: A) without and B) with NS5A-specific antibodies. The nuclei of these FCA1 cells were counterstained with DAPI (4',6-diamidino-2-phenylindole, exhibiting blue fluorescence) as an internal reference. The images were taken under an Olympus fluorescence microscope. C) Fluorescence-intensity ratios of blue channel (from DAPI) and red channel (from QDs) were calculated on the basis of the fluorescence images taken from the immunostaining tests. A: control test, and B: test with antibody-functionalized QDs. (Reprinted with permission from ref 151).

Table 4-1. Stability test of CdSe/ZnS NCs capped with different ligands

Ligands	T ^a (%)	DLS (nm) ^b	pH	[NaCl]
TD ₂₀ -L	100	~18	3.5~11	0.7M
DHLA-PEG2000 ^[95]	100	~29	5.5~11	0.7M
PEG2000-PMAO (30:1) ^[150]	65	~28	3.5~12	0.7M
PEG5000-PMAO (30:1) ^[150]	100	~35	3.5~13	1.0M
Cysteine	100	~9	2~13 ^c	0.3
Modified PAA ^[155]	70	~14	4.5~13	0.4

a: transfer efficiency of ligand exchange; b: at pH~6. 5; c: Cysteine-capped CdSe/ZnS NCs are not stable at pH around 5.

CHAPTER 5
GOLD NANOCRYSTAL-BASED ASSAY FOR THE DETECTION OF β -GALACTOSIDASE

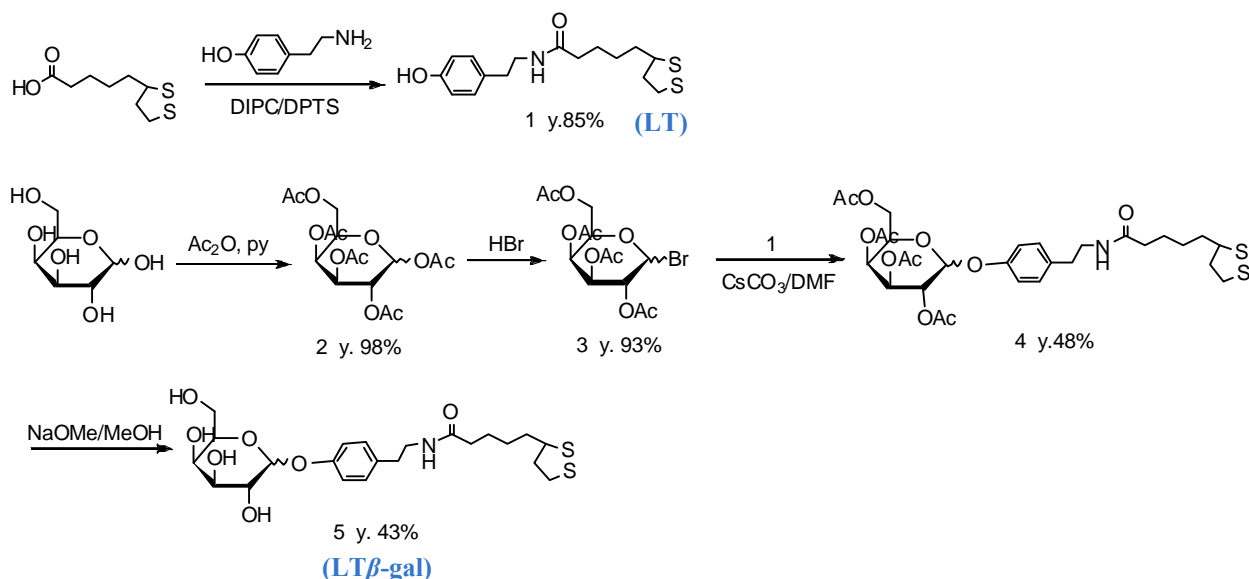
5.1 Introduction

Because of its high selectivity and stability, β -galactosidase is a commonly used reporter gene marker in gene expression studies.^[156,157] The current method for detecting β -galactosidase involves the use of fluorometry based upon organic dyes.^[158-160] After incubation with the enzyme, a weakly fluorescent substrate is converted into a highly fluorescent substrate. However, most of organic dyes are toxic and cannot be used to study gene expression in living systems. Recently, a magnetic resonance imaging (MRI) contrast agent was designed to identify β -galactosidase,^[161-163] in which the access of water to a chelated paramagnetic ion (Gd^{3+}) is blocked by the galactopyranosyl ring. In the presence of galactosidase, the galactopyranosyl ring can be cleaved by β -galactosidase, resulting in a change in the T_1 .^[163] However, this method has low sample throughput, and it requires multi-step and low-yield synthesis, and complicated instrumentation. Therefore, a need exists for developing simple and easy assays for the detection of β -galactosidase. Chromophoric colorimetric methods have attracted attention due to their easy readout (even by the naked eye). Compared with fluorometric methods, colorimetric detections are not hindered by background from either autofluorescence of analytes or fluorescence created during sample preparation. However, colorimetric methods normally suffer from low sensitivity and high limits of detection (LOD) $\geq \sim 1\mu M$.^[164]

Recently, Au NP-based colorimetric sensors have become an attractive research area because of the special optical and electronic properties of Au NCs, in particular surface plasmon resonance (SPR).^[165] The positions of SPR peaks of Au-NCs are dependent not only on the size and shape of Au NCs, but also on the distances between the particles. The SPR change of Au-NCs can be measured from the adsorption spectrum of a Au-NP solution, and it can even be

observed by the naked eye. In addition, these Au-NCs possess high stability and easy surface modification. The molar extinction coefficient of Au-NCs aqueous solutions ($\sim 2 \times 10^8 \text{ M}^{-1} \text{ cm}^{-1}$ per particle), which is extremely high compared to those of most organic dyes, provides a promising detection sensitivity. Therefore, Au-NCs have been applied for a wide variety of assays, such as detection of proteins,^[98] metal ions^[166] or other small organic molecules.^[164] However, assays for β -galactosidase activity based on Au-NCs have not been developed. Therefore, we have designed a new type of Au NP-based biosensor to detect β -galactosidase, based on the distance-dependent SPR of Au-NCs.

Figure 5-1 shows the molecular design of the sensor and the general principle for detection of β -galactosidase. Galactopyranosyl functionalized ligands, LT β -gal are used to cap Au-NCs and stabilize the NCs in aqueous solution. The galactopyranosyl ring is cleaved from the ligand after the addition of β -galactosidase, resulting in the Au-NP aggregation, and the color of the Au-NP solution changes from red to purple.



Scheme 5-1. Synthetic route of LT β -gal ligands.

5.2 Experimental Section

5.2.1 Chemicals.

N,N'-Diisopropylcarbodiimide (DIPC, 99%), iron (III) chloride ($\text{FeCl}_3 \cdot 6\text{H}_2\text{O}$, 98%), 1-octadecene (ODE, 90%), octadecylamine (ODA, 97%), *p*-toluenesulfonic acid monohydrate (98%), (\pm)- α -lipoic acid (99%), tyramine (99%), D-(+)-galactose (99%), acetic anhydride ($\geq 99\%$), hydrobromic acid solution ($\geq 33\%$ in acetic acid), cesium carbonate (99.9%), triphenylphosphinegold(I) chloride (AuPPh_3Cl , 99.9+%), *tert*-butylamine borane (TBAB, 97%), 1-dodecanethiol ($\geq 97\%$), β -galactosidase from *E. Coli* (molecular weight 540,000, EC 3.2.1.23) and β -glucosidase from almonds (EC 3.2.1.21) were purchased from Aldrich. Nanopure water ($18.2 \text{ M}\Omega \cdot \text{cm}$) was prepared by a Barnstead Nanopure Diamond system. All the other reagents were purchased from Fisher Scientific International Inc.

4-(*N,N'*-Dimethylamino)pyridinium-4-toluenesulfonate (DPTS) was prepared by mixing THF solutions of DMAP (2 M, 50 mL) and *p*-toluenesulfonic acid monohydrate (2 M, 50 mL) at room temperature with stirring. The resulting precipitate was filtered and dried under vacuum.^[142]

5.2.2 Synthesis of LT β -gal

The synthetic route to prepare LT β -gal is shown in Scheme 5-1. Lipoic acid and tyramine react in the presence of DIPC and DPTS to form 5-(1,2-dithiolan-3-yl)-*N*-(4-hydroxyphenethyl)pentanamide (compound 1). Galactose is first acetylated and the acetyl-group at the anomeric carbon is replaced with bromide to form 1- α -bromo-2,3,4,6-tetraacetyl-D-galactose (compound 3). Compound 3 condenses with 1 which is deacetylated via reaction with sodium methoxide (NaOMe).

Preparation of 5-(1,2-dithiolan-3-yl)-N-(4-hydroxyphenethyl)pentanamide

(compound 1, LT). Tyramine (3.3 g, 24.0 mmol), lipoic acid (2.6 g, 12.8 mmol), and DPTS (4.7 g, 15.1 mmol) were mixed in pyridine (30 mL) and stirred for several minutes at room temperature. Then, DIPC (2.3 mL, 15.1 mmol) was added to the mixture. After being stirred at room temperature overnight, the reaction mixture was filtered and the solvent was removed under reduced pressure. The oily residue was dissolved in CHCl₃ (100 mL) and washed with water (60 mL) three times. The organic phase was collected, dried over MgSO₄, filtered and concentrated. The crude product was purified by column chromatography on silica gel (ethyl acetate/hexane 7:3) to give a yellow powder. Yield: 85%. ¹H-NMR (300 MHz, CDCl₃): δ 6.80-7.02 (dd, 2H), 3.50 (m, 2H), 3.07 (m, 3H), 2.76 (t, 2H), 2.43 (m, 1H), 2.12 (t, 2H), 1.90 (m, 1H), 1.64 (m, 1H), 1.40 (m, 2H).

Preparation of pentaacetyl-D-galactose (compound 2). D-galactose (3.00 g, 16.7 mmol) was dissolved in dry pyridine (33 mL) at 0 °C under Ar flow. Then acetic anhydride (31.5 mL, 333 mmol) was added slowly. The reaction mixture was stirred at 0°C for 1 hr before a catalytic amount of DMAP (200 mg, 1.67 mmol) was added. Then the reaction mixture was stirred at room temperature for 6 h. The resulting clear yellow solution was poured into rapidly stirring ice water (500 mL) and extracted with ethyl acetate (75 mL) two times. The combined organic phase was dried over MgSO₄ and filtered. The solvent was removed under reduced pressure to give a white oily product. Yield: 98 %. ¹H-NMR (300 MHz, CDCl₃): δ 6.35 (s, 1H), 5.46-5.47 (m, 1H), 5.29-5.31 (m, 2H), 4.29-4.33 (m, 1H), 4.02-4.10 (m, 2H), 1.96-2.12 (m, 15H).

Preparation of 1-α-bromo-2,3,4,6-tetraacetyl-D-galactose (compound 3). Compound 2 (5.77 g, 14.7 mmol) was dissolved in a HBr (14.7 mmol) acetic acid solution (20 mL). After 3 h, the reaction mixture was evaporated and coevaporated with dry toluene under reduced

pressure to give a brown oily product. Yield: 93%. ¹H-NMR (300 MHz, CDCl₃): δ 6.66 (d, 1H), 5.45-5.47 (m, 1H), 5.36 (m, 1H), 5.00 (m, 1H), 4.41-4.46 (m, 1H), 4.05-4.10 (m, 2H), 1.95-2.09 (m, 12H).

Preparation of 2-(4-(2-(5-(1,2-dithiolan-3-yl)pentanamido)ethyl)phenoxy)-2,3,4,6-tetraacetyl-D-galactose (compound 4). Compound 1 (1.00 g, 3.07 mmol) was dissolved in dry *N,N*-dimethylformamide (5 mL) and cesium carbonate (4.00 g, 12.28 mmol) was added to the solution at 0 °C. Compound 3 (5.03 g, 12.28 mmol) in dry *N,N*-dimethylformamide (20 mL) was added dropwise under an Ar flow, and the reaction solution was stirred at room temperature for 4 h. Then the inorganic precipitate was removed by filtration and the filtrate was concentrated under reduced pressure. The residue was diluted with water and extracted with ethyl acetate, and the combined organic extracts were dried over MgSO₄ and filtered. After removing the organic solvent by evaporation, the crude product was purified by column chromatography on silica gel (ethyl acetate/hexane 1:1 to 9:1) to give a yellow powder. Yield: 48%. ¹H-NMR (300 MHz, DMF): δ 6.94-7.12 (m, 2H), 5.42 (m, 2H), 5.12 (m, 1H), 5.01 (d, 1H), 4.22-4.04 (m, 2H), 3.45 (m, 2H), 3.11 (m, 3H), 2.76 (t, 2H), 2.43 (m, 1H), 2.02-2.16 (m, 12H), 1.95 (m, 1H), 1.68 (m, 1H), 1.42 (m, 2H).

Preparation of LTβ-gal (compound 5). Compound 4 (0.97 g, 1.47 mmol) was dissolved in methanol (20 mL). Sodium methoxide (0.02 g, 0.37 mmol) was added at 0 °C and the solution was stirred at room temperature for 2 h. The reaction mixture was neutralized with Amberlite IR-120 plus (H⁺). The Amberlite was removed by filtration, and the filtrate was evaporated. The remaining organic solid was purified by column chromatography silica gel (chloroform/methanol 9:1) to give a yellow powder. Yield: 43%. ¹H-NMR (300 MHz, CDCl₃): δ 6.92-7.08 (dd, 2H), 5.12 (d, 1H), 4.72-4.80 (dd, 2H), 4.60 (t, 1H), 4.42 (d, 1H), 3.45 (m, 2H), 3.11 (m, 3H), 2.60 (t,

2H), 2.40 (m, 1H), 2.01(t, 2H), 1.80(m, 1H), 1.60 (m, 1H), 1.42 (m, 1H), 1.28 (m, 2H).

$[M+H]^+=488.18$ (Appendix C).

Preparation and 8.0 nm gold nanocrystals. Gold NCs were synthesized according to the literature procedure.^[118] In a typical synthesis, AuPPh₃Cl (0.124 g, 0.25 mmol) and dodecanethiol (0.125 mL, 0.50 mmol) were dissolved in benzene (20 mL) to form a clear colorless solution. Then *tert*-butylamine borane (TBAB, 0.22 g, 2.5 mmol) was added. The resulting solution was stirred at 100 °C via silicon oil bath for 1 h. The NCs were precipitated from the reaction solution with ethanol (30 mL), isolated by centrifugation and re-dispersed in CHCl₃. The resulting NCs have a diameter of 8.0 nm with a standard deviation of 7.0 %.

Preparation of LT β -gal-capped water-soluble NCs. Hydrophobic 8.0 nm Au NCs (5 μ mol) in CHCl₃ (2 mL) and LT β -gal (10 μ mol) in ethanol (2 mL) were mixed. Then triethylamine (0.05 mL) was added and the resulting mixture was stirred overnight. Then Au NCs were precipitated and the solvent was discarded. These NCs were washed with chloroform twice and re-dispersed in water. The excess of LT β -gal ligands was removed by spin filtration (Millipore, 10K NMWL, 10000 \times g, 10 min) four times. The resulting NCs were re-dispersed in aqueous buffer solution (PBS, pH 7.4, 25 °C) for further studies. Using the same method, Au-NCs capped by a mixture of ligands (LT β -gal and LT with different weight ratios: 4:1, 2:1, 4:3, 1:1, and 3: 4) were also prepared.

5.2.3 Detection of β -galactosidase

Solutions of PBS buffer (pH 7.4, 1.25 mL), a magnesium chloride (MgCl₂, 30 mM, 0.05 mL) were prepared in separate tubes, Varying amount of β -galactosidase were added and the mixtures were equilibrated to 37 °C. Then the LT β -gal capped Au-NP solution was added to each mixture. The peak positions and absorbances at 523 nm were monitored. The intensities were

measured at the wavelength of 523 nm. A blank PBS buffer solution and a glucosidase solution were used for control tests.

5.2.4 Measurements

5.2.4.1 ¹H-NMR Measurements

¹H-NMR spectra were recorded using a Varian Mercury NMR Spectrometer (300 MHz). The samples were prepared by adding aliquots of products (10 mg) to CDCl₃.

5.2.4.2 UV/Vis Spectra

UV/Vis spectra of Au-NCs were measured using UV-1700 PharmaSpec UV-Visible spectrophotometer (Shimadzu, MD).

5.2.4.3 DLS Measurements

The nanocrystal aqueous solutions were filtered through a 0.22- μ m MCE syringe filter (Fisher Scientific). The hydrodynamic sizes of NCs were obtained using Brookhaven Instr. Corp. dynamic light scattering instrumental (Holtsville, NY) at 25 °C.

5.2.4.4 TEM Measurements

TEM measurements were performed on a JEOL 200CX operated at 200 kV. The specimens were prepared as described in previous chapters.

5.3 Results and Discussion

The galactopyranosyl-ring functionalized ligand (LT β -gal) was synthesized by simple organic reactions, as described above. To stabilize Au-NCs, a dithiol coordination group was incorporated into the ligand. The ligand-exchange reaction was performed to make the Au-NCs water-soluble with a transfer yield of nearly 100%. These functionalized Au-NCs are stable in the aqueous buffer solution (PBS, pH 7.4, 25 °C) for more than five months. The UV/Vis absorption spectrum of the Au-NCs in the PBS buffer solution shows a sharp peak at 523 nm, which indicates that these functionalized Au-NCs are well dispersed in the buffer solution. The

TEM images show a monolayer of the functionalized Au-NCs, indicating that no aggregation occurs.

To demonstrate the suitability of using these Au-NCs (8.0 nm in diameter) for enzyme detection, a solution of functionalized Au NCs (PBS, pH 7.4) was added to enzyme β -galactosidase buffer solution (PBS, pH 7.4) with various concentration at 37 °C, and UV/Vis measurements were performed to monitor the aggregation of Au NCs. In control experiments, the Au-NC buffer solution was added to a blank PBS buffer solution (without any enzyme) and a β -glucosidase buffer solution (PBS, pH 7.4) at 37 °C. The control solutions showed a very small red-shift (≤ 3 nm) and a tiny decrease in absorbance after being mixed with the Au NC suspension for 6 hr. In contrast, Figure 5-2 shows that the mixture of Au NCs and β -galactosidase exhibits a 21 nm red-shift and a dramatic decrease in absorbance within 1 hr after the addition of Au-NC solution. The red-shift absorbance of the SPR (from 523 nm to 544 nm) and the decrease of the absorbance at 523 nm are due to the aggregation of Au-NCs. The change is easily observed even by the naked eye.

Interestingly, when the pure LT β -gal-capped Au-NCs were used as the probes to detect β -galactosidase, no shift was observed in the UV/Vis absorption of the Au-NC suspension. We attribute this to the possibility that β -galactosidase cannot reach the active site of galactopyranosy ring when LT β -gal is the only ligand bound to the surface of Au-NCs. Introducing another short ligand, LT, to the surfaces of Au-NCs separates the LT β -gal sufficiently for the active-site on the LT β -gal, which allows to interact with β -galactosidase. Since the pure LT capped Au-NCs are unable to disperse in the aqueous solution, changing the ratios between LT β -gal and LT affects the solubility of corresponding Au-NCs and causes different sensitivities of these Au-NCs.

To test the effect of the use of two ligands on the sensitivity of these assays, the Au-NCs capped with LT and LT β -gal at different ratios were prepared. The kinetics of Au-NP aggregations was studied using the same conditions for these different Au-NCs. As the indication of Au-NP aggregation, the absorbance at 523 nm was measured every 15 minutes after mixing the enzyme solution with the Au-NP suspension, as shown in Figure 5-3A. The aggregation of Au-NCs is faster when the surface of Au-NCs is covered by a higher percent of LT. However, the higher percent of LT capped on the Au NCs results in a decrease in the stability of the Au-NCs. The highest percentage of LT on the Au-NCs is about 57% (3:4 molar ratio LT β -gal: LT). Further increase of the amount of LT on the Au-NP surface induces Au-NP aggregation in the absence of enzyme.

The detection of enzyme was further studied for Au-NCs capped with LT β -gal and LT of at a ratio 3: 4. Different concentrations of β -galactosidase (0, 5, 10, 20, 40, 60, 80, 140, 200, 250 and 300 units/ml) were tested, as shown in Figure 5-3B. A linear relationship between the enzyme concentration and the wavelength shift of Au-NCs suspensions is observed when the concentration of enzyme is less than 100 units/mL. However, the wavelength shift reaches the maximum when the concentration of β -galactosidase is around 140 units/mL. If the concentration of β -galactosidase is further increased, the absorption shift begins to drop. One possible reason is that the excess β -galactosidase in the solution can attach to the surface of Au-NCs and facilitate the solubility of Au-NCs in the aqueous solution.^[12]

In summary, we have demonstrated a new design of β -galactosidase assay based on Au-NC's aggregation. The enzyme was detected by the red-shifted absorbance of the SPR and the decrease of the absorbance of Au-NP solutions. The sensitivity of the Au-NP based assay was tuned by varying the ratios of dual ligands, LT β -gal and LT. The design is useful not only for the

detection of β -galactosidase, but also for the detection of other enzymes via rational design of the ligands on Au-NCs. For example, a phosphate group functionalized ligand can be used for the detection of phosphatase.

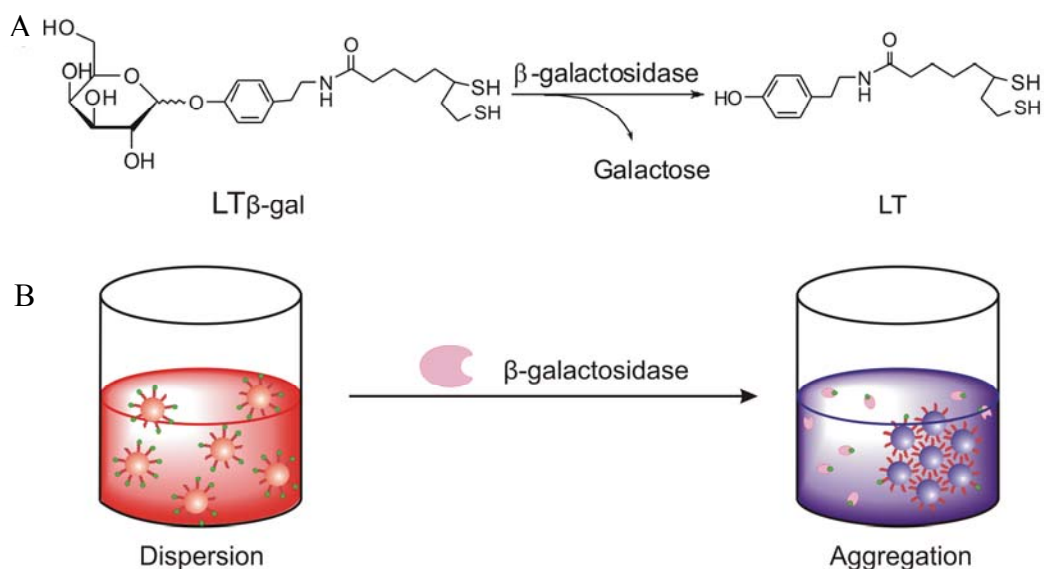


Figure 5-1. β -galactosidase assay based on Au-NCs. A) The molecular structure of LT β -gal. Galactopyranosyl ring is the hydrophilic part in LT β -gal. After interacting with β -galactosidase, the galactopyranosyl ring is cleaved from LT β -gal, which induces the Au-NCs to aggregate. B) The color of Au-NP aqueous solution changes from red to purple due to the aggregation of Au-NCs.

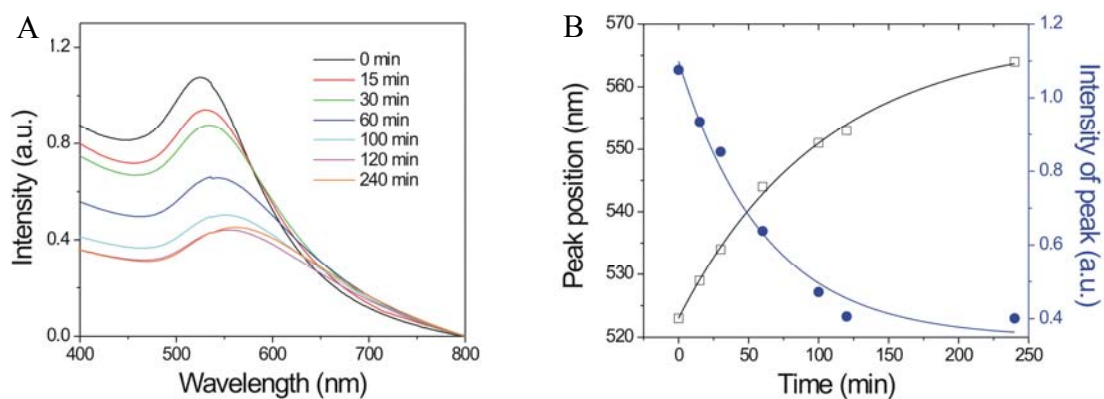


Figure 5-2. Detection of β -galactosidase. A) UV/Vis spectra of LT β -gal capped Au-NC solutions at 0 min (black line), 15 min (red line), 30 min (green), 60 min (blue), 100 min (cyan), 120 min (purple) and 240 min (orange) after the addition of the β -galactosidase buffer solution; B) the red-shift of the peak (\square) and the decrease of the absorbance (\bullet) of Au-NP solutions.

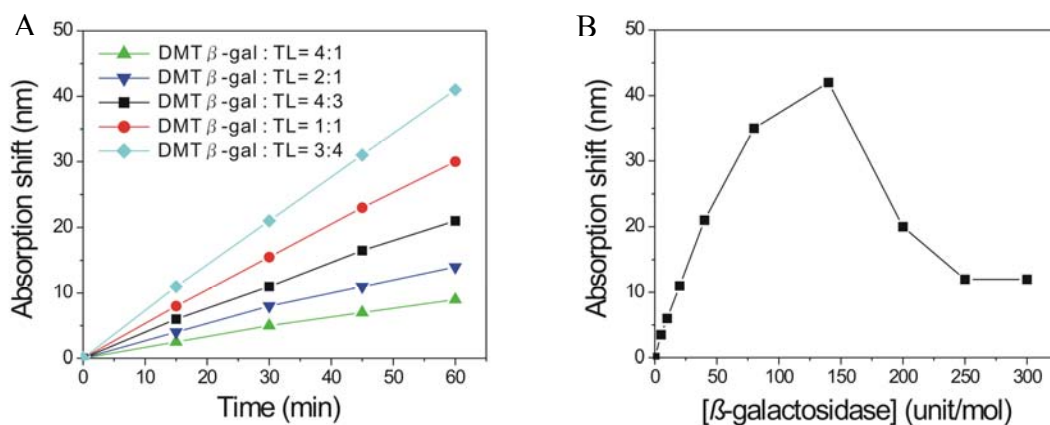


Figure 5-3. Kinetics studies of the enzyme-induced Au-NC aggregation. A) Au-NCs were capped with LT β -gal and LT at different molar ratios. The spectra were measured every 15 min after the addition of Au-NCs suspension. B) The absorption shifts of Au-NC solution at different concentrations of β -galactosidase, measured at 30 min after the addition of Au-NCs suspension. Au-NCs were capped with LT β -gal and LT at the molar ratio of 3:4

CHAPTER 6 SYNTHESIS OF HYBRID NANOCRYSTALS

6.1 Introduction

Compared to single-component inorganic nanomaterials, hybrid nanocrystals (HNCs) are attractive candidates for advanced nanomaterials because they contain two or more different nanoscale functionalities. By tuning the compositions and tailoring the topological domain for each composition, these nanocomposites can exhibit novel physical and chemical properties that will be essential for future technological applications. For example, the core/shell structure provides a protective shell on the core material and significantly improves stability. The difference in surface chemistry of heterodimer-structured nanocrystals allows different functional molecules to attach to the heterodimer, which is very useful in biomedical applications.

In general, the topologies of hybrid nanocrystals are controlled by both kinetic processes and thermodynamic factors during the synthesis.^[167] It is believed that interfacial structures play an important role in the final crystallographic structures of HNCs. Core/shell HNCs can be formed when the two components have similar lattice constants and when the synthesis parameters allow the interfacial energy to be kept low. So far, core/shell structured HNCs have been prepared for various semiconductors (such as CdSe, CdS, CdTe, ZnS, ZnSe, InAs) in which the outer shell of a higher band gap material increases the photostability and enhances the photoluminescence (PL) quantum yield of the core^[58,59,113,168]. When the materials possess limited miscibility or a large interfacial energy, heterodimer structured nanocrystals can be formed, in which the two materials are phase segregated into two separate particle domains, and the limited junction areas allow the minimization of interfacial energy. Heterodimer formation has been exploited to grow FePt/CdS^[169], FePt/CdSe^[170], FePt/Fe₃P₄^[167], Fe₂O₃/group II-IV sulfide,^[171] Fe₃O₄/Ag^[172] Fe₃O₄/Au^[173], and CoPt₃/Au^[174] HNCs.

The influence of the lattice mismatch on the formation of HNCs has been explained by the coincidence site lattice (CSL) theory^[175]. For specific orientations of crystal lattices, there are specific lattice points of one lattice which coincide with points of the other lattice.^[176] Therefore, on a crystal substrate, with an exposure facet having a certain crystallographic orientation, a second material with another type of lattice tends to grow, and its relative orientation produces the best fit of the lattice points of the two structures at the interfacial plane. This match occurs at regular intervals along two directions of the interfacial plane to define the two-dimensional cell that describes the interface. The better the fit between lattice points of the two structures and the shorter the repetition intervals, the lower the interfacial energy will be.^[171]

So far, the synthesis parameters of heterostructured NCs have not been fully characterized out, and CSL theory cannot always explain the relationships between two domains of HNCs. The development of HNCs with controlled structures and interfacial interactions requires further studies of the growth of HNCs. In this chapter, two kinds of heterostructured dimers (FePt/In₂O₃ and UO₂/In₂O₃) were synthesized using a seed-growth procedure and different topologies were observed. The interfacial structure was investigated carefully by HRTEM and an amorphous layer on the seed nanocrystals played an important role in the formation of the heterodimers.

6.2 Experimental Section

6.2.1 Chemicals

Platinum (II) acetylacetonate (Pt(acac)₂, 99%) and uranyl(VI) acetylacetonate (UAA, 99%) were purchased from STREM Chemicals. Iron pentacarbonyl (Fe(CO)₅, 98%), indium (III) acetate (99.99%), trimethylamine *N*-oxide (TMNO, 98%), 1-octadecene (ODE, 90%), oleic acid (OA, 90%), oleylamine (OAm, 70%), were purchased from Aldrich. All the other reagents were purchased from Fisher Scientific International Inc.

6.2.2 Synthesis of FePt Nanocrystals

Modified literature procedures were used to prepare 6.7 nm FePt NCs. In a typical synthesis, Pt(acac)₂ (100 mg, 0.25 mmol) was mixed with 7.5 ml of ODE, and the mixture was degassed under vacuum at 60°C for 10 min. Then the mixture was heated to 130 °C under Ar flow, resulting in a clear yellow solution, which indicated that the Pt(acac)₂ salt was completely dissolved in ODE. Subsequently, Fe(CO)₅ (95 mg, 0.5 mmol) dissolved in 785 mg (2.5 mmol) of OA, was swiftly injected into the reaction mixture. After 5 min, 955 mg (2.5 mmol) of OAm was added to the reaction mixture. Then, the reaction mixture was heated to 200 °C at a rate of approximately 10 °C/min, aged at this temperature for 1hr, and then cooled to room temperature. The NCs were precipitated from the reaction mixture by adding acetone. The black NCs were further washed twice with a mixture of hexane and acetone (1:4) to remove excess surfactant and unreacted precursors. Finally they were fully dissolved in non-polar solvents, such as hexane, toluene or chloroform.

6.2.3 Synthesis of UO₂ Nanocrystals

The method described in section 3.2.3 was used to prepare 6.2 nm UO₂ nanocrystals.

6.2.4 Preparation of Indium Stock Solution

Indium acetate (165 mg, 0.4 mmol), oleylamine (0.55 mL), and oleic acid (0.6 mL) were mixed with ODE (7 mL) in a three-neck flask. The mixture was degassed under vacuum at 110 °C for 30 min to form a clear light-green solution. Trimethylamine *N*-oxide (TMNO, 161 mg, 1.45 mmol) was added to the vigorously stirred hot mixture under Ar. Then, the reaction mixture was further degassed at 120 °C for 1hr. The resultant yellow indium stock solution, was stored at room temperature under Ar protection.

6.2.5 Synthesis of Corn-seed-shaped FePt/In₂O₃ Hybrid Nanocrystals.

After heating at 200 °C for 1 h, the reaction mixture for the synthesis of FePt NCs (section 6.2.2) was further heated to 300 °C at a rate of approximately 7 °C/min under Ar flow. Indium stock solution was then injected into the FePt NCs solution. After heating at 300 °C for 30min, the mixture was cooled to room temperature. The hybrid nanocrystals (HNCs) were precipitated from the reaction solution by adding acetone and were further purified by adding a mixture of hexane and acetone (1:4). The black nanocrystal precipitate was easily redispersed in non-polar organic solvents such as hexane or toluene.

A small aliquot of the FePt reaction mixture was extracted via a syringe before injection of the indium stock solution at 300 °C. The aliquot was suddenly cooled, and the NCs were purified as described above.

A control experiment was also performed by heating the FePt reaction mixture to 300°C for 30 min without injection of the indium stock solution.

6.2.6 Synthesis of Peanut-shaped UO₂/In₂O₃ Hybrid Nanocrystals.

After heating at 300 °C for 5min, the reaction mixture of synthesis of UO₂ NCs (section 6.2.3) was cooled to room temperature and mixed with 8 ml of ODE. The mixture was then heated to 300 °C at a rate of approximately 15 °C/min under Ar flow. Indium stock solution was then injected into the UO₂ NCs solution. After heating to 300 °C for 30min, the mixture was cooled to room temperature. The hybrid nanocrystals (HNCs) were precipitated from the reaction solution by adding acetone and further purified as described above (section 6.2.5).

6.2.7 TEM Measurements

TEM measurements were performed on a JEOL 200CX operated at 200 kV. To prepare the specimens, a particle solution (10 µL) was dropped onto a 200-mesh copper grid, and dried overnight at ambient conditions.

6.3 Results and Discussion

6.3.1 Synthesis and Characterization of FePt/In₂O₃ Hybrid Nanocrystals

Cubic FePt nanocrystals with an average size of 6.7 nm (Figure 6-1A) were obtained after heating the reaction mixture at 200 °C for 1 hr. Following the formation of the FePt NCs, further heating of the reaction mixture to 300 °C induced the additional growth of thin iron-layers, which were further oxidized under air and converted to iron oxide layers. Figure 6-1B shows the core/shell-structured nanocrystals. Since the image contrast of Iron oxide is lower than that of FePt, the light thin shells come from Iron oxide layers and the dark cores are FePt nanocrystals. The shells of Iron oxide on the cores are not evenly dispersed, resulting in incomplete coverage of FePt cores. Figure 6-1C shows corn-seed-shaped hybrid nanocrystals, which were obtained after the injection of indium stock solution and subsequent heating.

Figure 6-1D illustrates the formation of the corn-seed-shaped dimer. In this system, the FePt-Iron oxide NCs act as seeds for the growth of indium oxide NCs and prevent the homogenous nucleation of indium oxide. Heterogeneous deposition of indium oxide on certain surfaces of FePt-Iron oxide NCs leads to the formation of corn-seed-shaped dimers. Since only about half of the FePt-Iron oxide NC surface is covered by In₂O₃, the HNCs have corn-seed-shaped structures. According to the coincidence site lattice theory, the lattice mismatch at the heterointerface in these dimers should be small, but this was not observed in further experiments described below.

To further characterize these hybrid nanocrystals, scanning transmission electron microscopy (STEM) was performed, to obtain more structural and compositional information about these nanocrystals. The contrast in dark-field STEM (DF-STEM, Figure 6-2A) is strongly dependent on atomic number, whereas bright-field STEM (BF-STEM, Figure 6-2B) is in some ways complementary to the dark-field contrast image. Thus, FePt cores show as bright areas in

DF-STEM and dark areas in BF-STEM. Conversely Iron oxide or In_2O_3 areas are dark in DF-STEM and bright in BF-STEM. However, the contrasts of Iron oxide or In_2O_3 are similar, so the domains of Iron oxide or In_2O_3 cannot be determined in these images.

Since the composition of the large part of the dimer is not clear, there is a possibility that it could be Iron oxide. To eliminate this possibility, a control experiment was performed by heating the FePt reaction mixture to 300 °C for 30 min without injection of the indium precursors. The resultant nanocrystals were observed by TEM, as shown in Figure 6-3. The Iron oxide shells are thicker than those in Figure 6-1B due to the extra aging time, but they are significantly smaller than the dimers obtained by the injection of the indium stock solution (Figure 6-1C). Thus, the further growth achieved in Figure 6-2B is most likely caused by the heterogeneous growth of In_2O_3 on the surfaces of the FePt-Iron oxide NCs.

High resolution TEM (HRTEM) studies provided more detail information about the crystal structures and orientations of these dimers. Figure 6-4 shows the HRTEM images of these individual dimers and different orientations of the FePt nanocrystals and the In_2O_3 nanocrystals are observed. The spacing of lattice fringes in Figure 6-4A are 1.95 Å and 2.70 Å, corresponding to the {200} lattice planes for FePt and {123} lattice planes for In_2O_3 , the lattice mismatch of respectively. The mismatch associated with this interface is about 28%. Such a huge lattice mismatch has not been commonly observed in other types of dimers,^[171,173] and are not predicted by the coincidence site lattice theory. These HRTEM images also clearly show that there are amorphous areas between the interfaces of the FePt and In_2O_3 NCs, as marked by red arrows. (No amorphous area is observed in Figure 6-4D, because the FePt part is sitting on the surface of the In_2O_3 NC and the interface is hidden. Therefore, it can be inferred that the amorphous layers

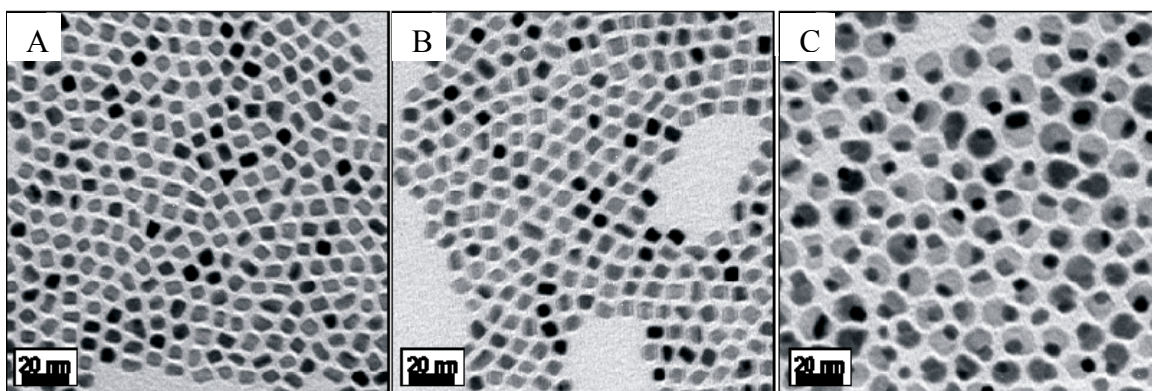
on the FePt nanocrystals acts as a glue and cause corn-seed-shaped dimers. Since there are no preferred heterointerface configurations, the growth of In_2O_3 can have different orientations.

6.3.2 Synthesis and Characterization of $\text{UO}_2/\text{In}_2\text{O}_3$ Hybrid Nanocrystals

As a comparison, another type of dimer was synthesized: $\text{UO}_2/\text{In}_2\text{O}_3$ dimer. The synthesis of UO_2 nanocrystals has been described in detail in chapter 3. The synthesized UO_2 nanocrystals are completely single-crystalline and stable in air, and have high contrast on TEM images. Thus, the UO_2 nanocrystal is a good candidate for the study of dimer formation. As described in section 6.2.6, the procedure for making $\text{UO}_2/\text{In}_2\text{O}_3$ dimers was the same as that for $\text{FePt}/\text{In}_2\text{O}_3$ dimers, but 6.2 nm UO_2 NCs were used as seeds (Figure 6-5A). The injection of the indium stock solution also led to the formation of dimers. However, the shapes of the $\text{UO}_2/\text{In}_2\text{O}_3$ dimers are different compared to the $\text{FePt}/\text{In}_2\text{O}_3$ dimers. The TEM image (Figure 6-5B) shows that $\text{UO}_2/\text{In}_2\text{O}_3$ dimers are peanut-shaped. This shape was further confirmed by DF-STEM and BF-STEM (Figure 6-5C and D). In this system, UO_2 show as bright areas in DF-STEM and dark areas in BF-STEM, whereas In_2O_3 is dark in DF-STEM and bright in BF-STEM. Figure 6-5E illustrates the formation of the peanut-shaped dimers.

HRTEM measurement was also performed in the investigations of the $\text{UO}_2/\text{In}_2\text{O}_3$ dimers. Only two types of heterointerface configurations were observed in this system. Figure 6-6A shows the most popular configuration. The fringe distances in Figure 6-5A are 2.73 Å and 2.53 Å, corresponding to the {200} lattice planes for FePt and the {400} lattice planes for In_2O_3 respectively. The calculated lattice mismatch, associated with this interface, is about 7%, which is in the range of common dimers. In the other type of heterointerface configuration, shown in Figure 6-6B, the lattice mismatch at the interface is also about 7%. The images clearly demonstrate a high crystallinity across the entire heterostructure. In conclusion, two kinds of heterostructured dimers, $\text{FePt}/\text{In}_2\text{O}_3$ and $\text{UO}_2/\text{In}_2\text{O}_3$, were synthesized using a similar procedure.

The injection of the same indium stock solution into the different seed solutions led to dimers with different shapes. The structures of the interfaces in these two systems were carefully investigated by HRTEM. The corn-seed-shaped FePt/In₂O₃ dimers cannot be explained by lattice mismatch, as proposed by the CSL theory. The amorphous Iron oxide layers on the FePt seed surfaces are believed to act as “glue” in the heterostructure. The UO₂/In₂O₃ dimers were synthesized as a comparison. In this system, no amorphous layers were observed on the UO₂ seed surfaces. This result agrees with the CSL theory because of the small lattice mismatch (~7%). The resultant dimers have peanut-shaped structures and fewer interfacial areas compared to the corn-seed-heterodimers. Further studies are currently underway to gain a deeper insight into the mechanism of dimer formation.



D

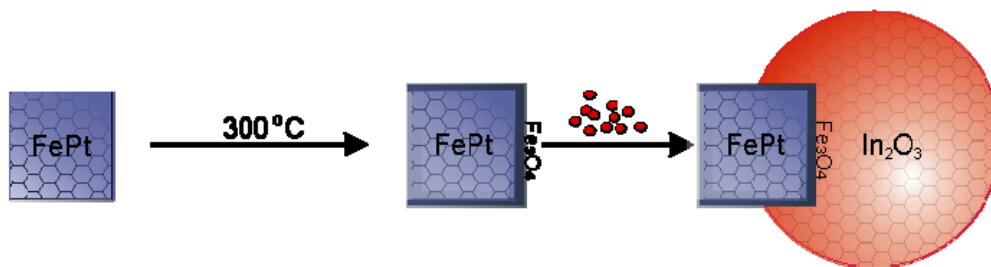


Figure 6-1. TEM images of A) FePt seeds, B) the nanocrystals extracted from the FePt reaction mixture before the injection of the indium stock solution. A thin layer of iron oxide was formed after the reaction mixture was heated to 300 °C; C) FePt/In₂O₃ hybrid nanocrystals, obtained from the reaction mixture after the injection of the indium stock solution and heating at 300 °C for 30 min. (d) Schematic illustration of the formation of the corn-seed-shaped dimer.

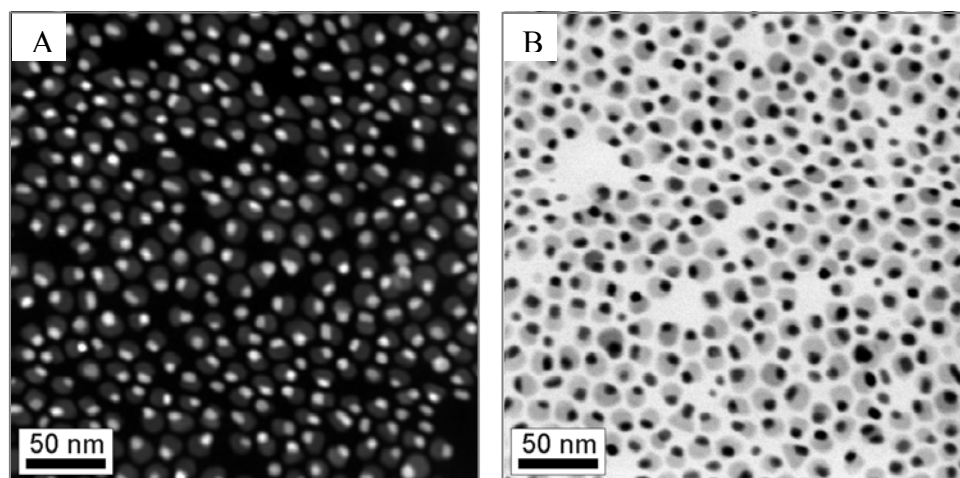


Figure 6-2. STEM images of FePt/In₂O₃ hybrid nanocrystals A) dark-field STEM and B) bright-field STEM

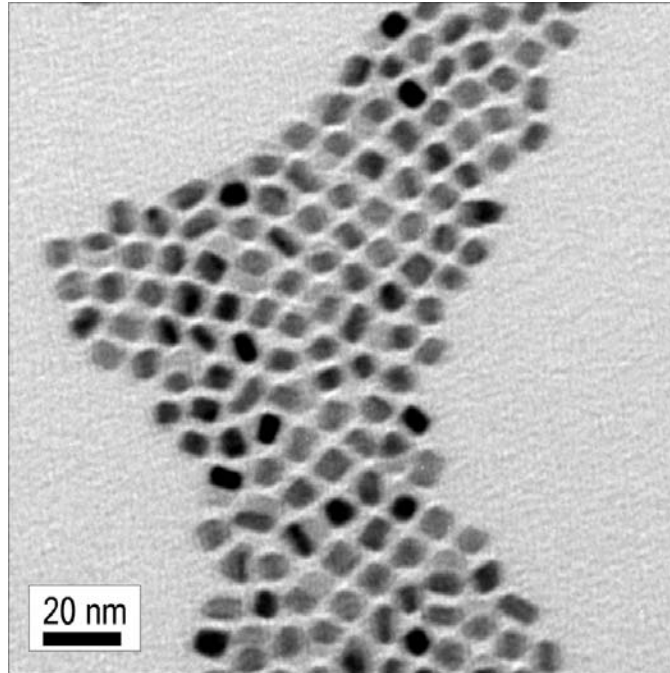


Figure 6-3. TEM image of the FePt-Iron oxide core-shell NCs obtained from the control experiment, in which the reaction mixture was heated to 300 °C and aged at that temperature for 30 min without the injection of the indium stock solution.

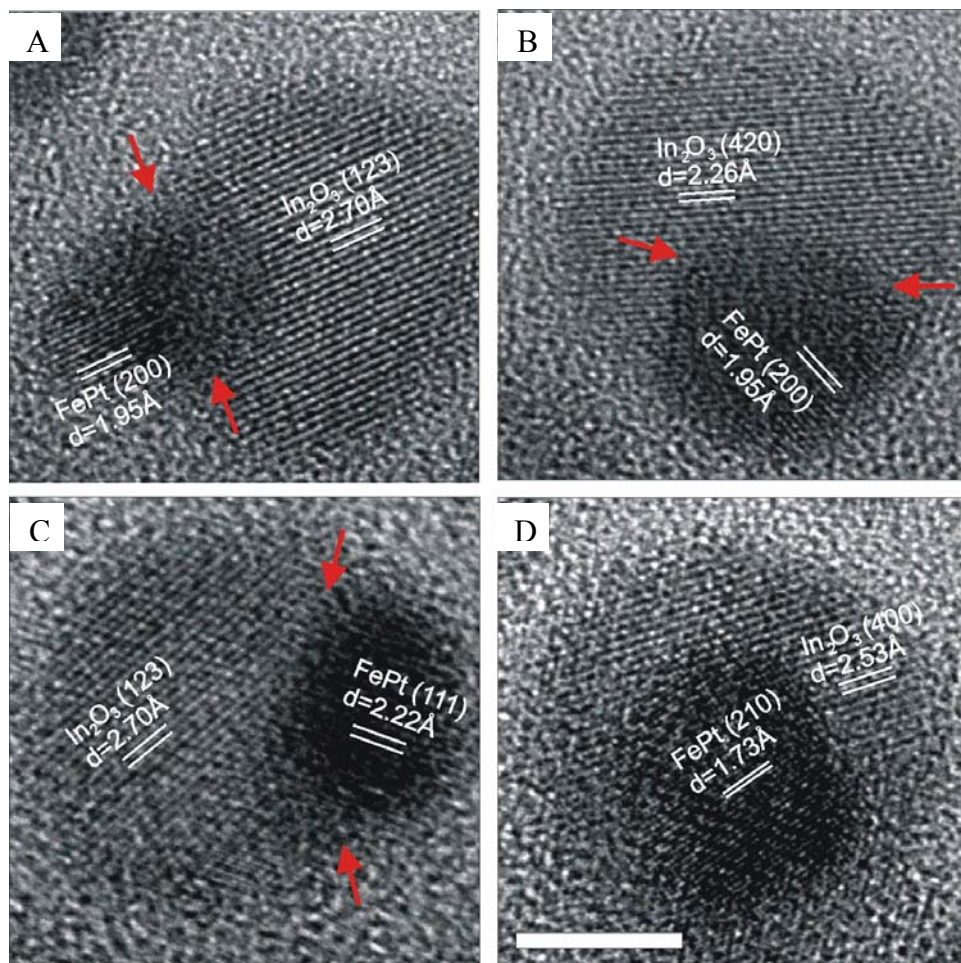


Figure 6-4. HRTEM studies of an individual FePt/In₂O₃ hybrid nanocrystal. Red arrows indicate areas of amorphous Iron oxide layers. The scale bar is 5 nm.

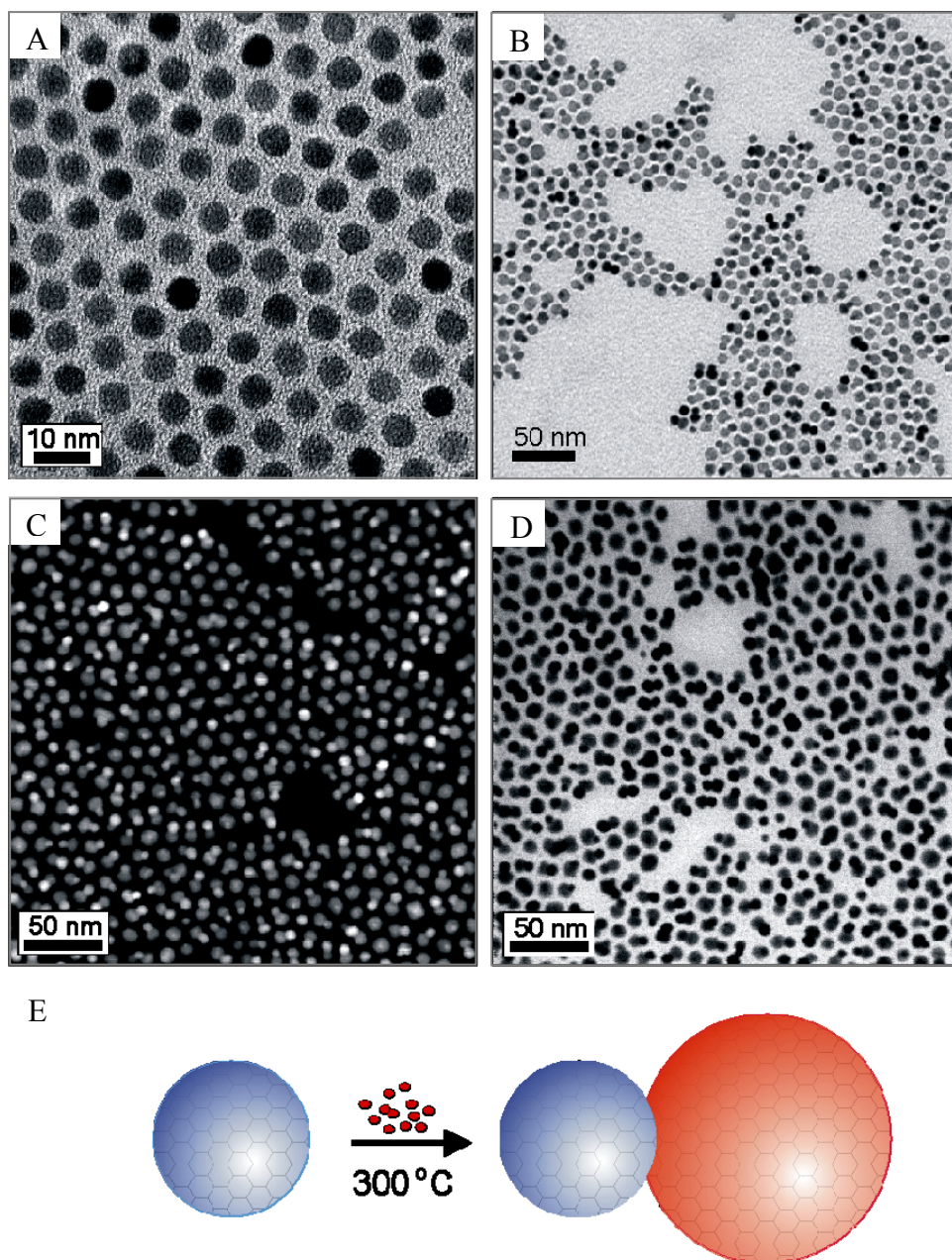


Figure 6-5. TEM images of A) 6.2 nm UO_2 seeds, B) $\text{UO}_2/\text{In}_2\text{O}_3$ hybrid nanocrystals; C) dark-field STEM image of $\text{UO}_2/\text{In}_2\text{O}_3$ hybrid nanocrystals and D) bright-field STEM image of $\text{UO}_2/\text{In}_2\text{O}_3$ hybrid nanocrystals. E) Schematic illustration of the formation of the peanut-shaped hybrid nanocrystals.

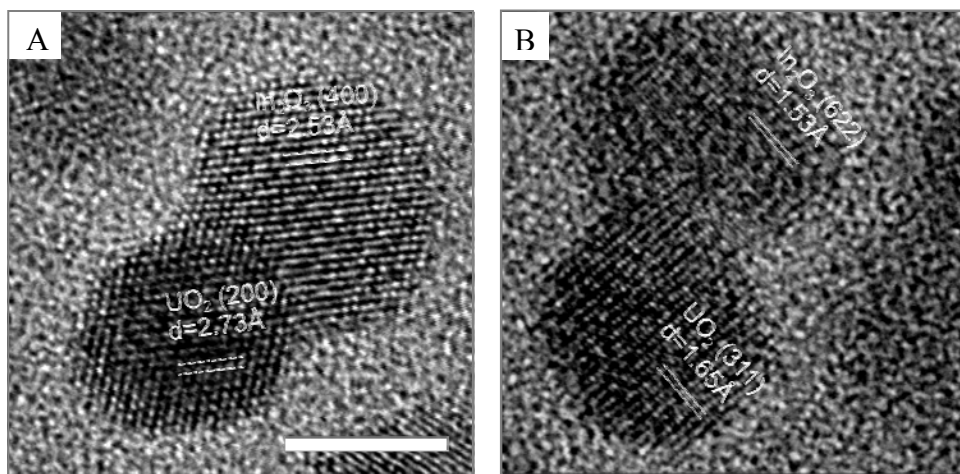


Figure 6-6. HRTEM images of an individual $\text{UO}_2/\text{In}_2\text{O}_3$ hybrid nanocrystal. The scale bar is 5 nm.

CHAPTER 7 CONCLUSIONS

7.1 Summary of This Research

A broad range of nanocrystals were synthesized and studied in this research. First of all, a one-pot synthesis for making high-quality monodisperse uranium-dioxide nanocrystals was developed. The size of UO_2 NCs could be controlled by adjusting the amount of ligands, and the shape of the particles was varied by tuning the precursor concentration per particle. Studies of the mechanism for controlling the nanocrystal formation demonstrated that the amide, the condensation product of oleic acid and oleylamine substantially affects the formation of UO_2 nanocrystals. Since oleic acid and oleylamine are widely used in synthesizing a variety of high-quality metal and metal-oxide nanocrystals, our results are very important for understanding the detailed mechanisms of these syntheses.

Second, a new concept for converting hydrophobic NCs (e.g., Au, Iron oxide, and CdSe/ZnS quantum dots) into hydrophilic NCs through dual-interaction ligands was demonstrated. A series of dual-interaction ligands, Tween derivatives (TDs), have been synthesized. The hydrophilic nanocrystals (Au and Fe_3O_4 NCs and CdSe/ZnS core/shell QDs) functionalized with these TDs exhibit high stability in aqueous solutions. Moreover, the TD-functionalized quantum dots were applied as fluorescence labels for monitoring the expression of a HCV (Hepatitis C virus) protein (NS5A) in FCA1 cells. Because of their excellent stability, these TD-functionalized nanocrystals can play an important role in a variety of nanocrystal-based biomedical applications.

Third, a gold nanocrystal-based assay to detect enzyme activity was designed taking advantage of the aggregation of the NCs induced by changes of ligands on the particle surface. A natural enzyme, β -galactosidase was chosen as the model system. As the proof-of-concept

experiment, a ligand functionalized with β -D-galactopyranoside was synthesized. Upon hydrolysis of the ligands by β -galactosidase, the gold NCs begin to aggregate, which induces a red-shift of the absorption maximum.

Fourth, more complicated hybrid nanocrystals were synthesized. Hybrid nanocrystals are interesting because of the combination of two or more different materials in one nanocrystal in separated phases. FePt/In₂O₃ and UO₂/In₂O₃ were prepared by a seed-growth method. The studies of the formation of FePt/In₂O₃ HNCs indicate that the amorphous iron-oxide layer on the seed particle surface acts as “glue” to interconnect the two components, and controls the final topologies of heterostructured NCs.

7.2 Perspectives

Nanocrystals have demonstrated many potential applications, especially in optoelectronic and biomedical areas. The development of nanocrystal synthesis allows preparation of monodisperse, shape- and size-controllable nanocrystals. In addition to the challenge of synthesizing high-quality nanocrystals, surface engineering and the controlled assembly of nanocrystal are also very important for the development of nanocrystal-based devices. For possible future directions, some researches are suggested in two areas: synthesis and surface engineering.

Synthesis. The development of new nanostructured materials and the investigation of new properties of nanomaterials will still be hot research areas. The concern about the toxicity of nanocrystals, such as CdSe/ZnS QDs, requires exploration of the biological effects of nanocrystals and eventually the development of low and non-toxic materials. And of course, to provide enough materials for testing, methods to prepare high-quality nanocrystals in large scale are needed. Hybrid nanocrystals are a new generation of NCs, which are expected to have a wide

range of applications in the future. Understanding of the crystal growth of these systems is crucial for future development.

Surface engineering. New functionalization methods are needed to be make nanocrystals suitable for various applications. The challenges existing in nanoscience, such as how to improve the stability and the performance of nanocrystals, how to realize selective surface modification, how to conjugate with biological molecules without losing their biological activities, and how to realize nanocrystal assemblies to build nanomachines are all related to the surface engineering of nanocrystals.^[177,178]

APPENDIX A
XRD MEASUREMENT OF URANIUMOXIDE NANOCRYSTALS

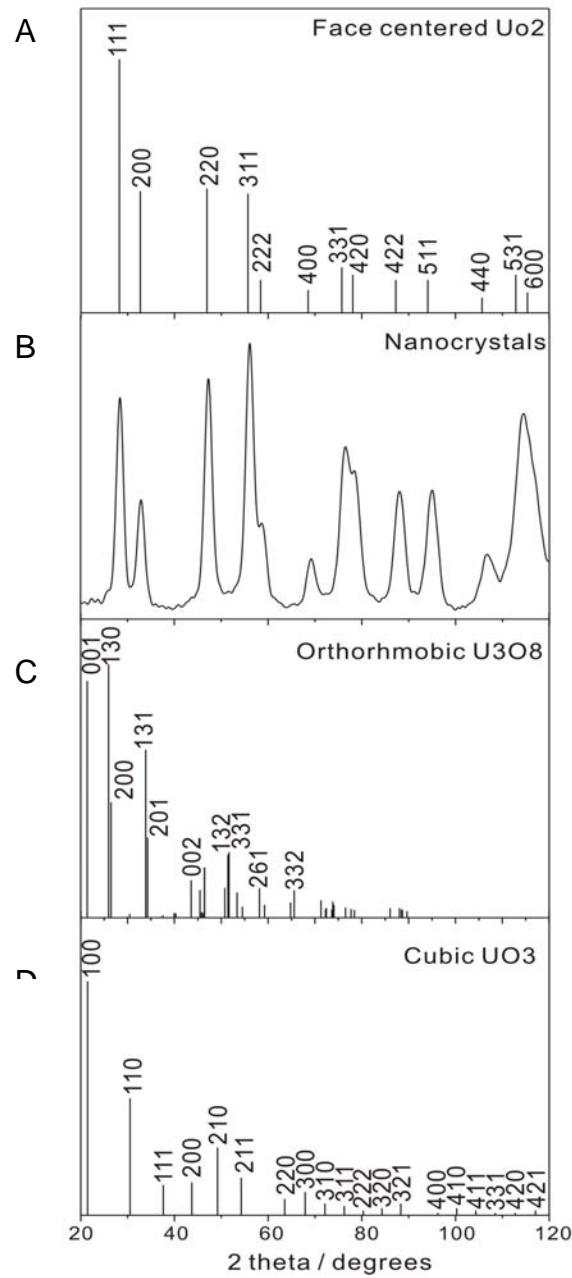


Figure A-1. XRD measurement of UO_2 Nanocrystals. A) The standard diffraction peak positions and relative intensities are indicated for the bulk and pure-phased face-centered cubic (fcc) UO_2 ; (B) the XRD spectrum for synthesized NCs; (C) for orthorhombic U_3O_8 and (D) for primitive cubic UO_3 . The Bragg diffractions of the uranium oxide NCs can be indexed to nearly all of those of the standard bulk face-centered cubic UO_2 . These Bragg diffractions are quite distinguishable from those Bragg diffractions of bulk UO_3 or U_3O_8 structures.

APPENDIX B
¹H-NMR SPECTRUM

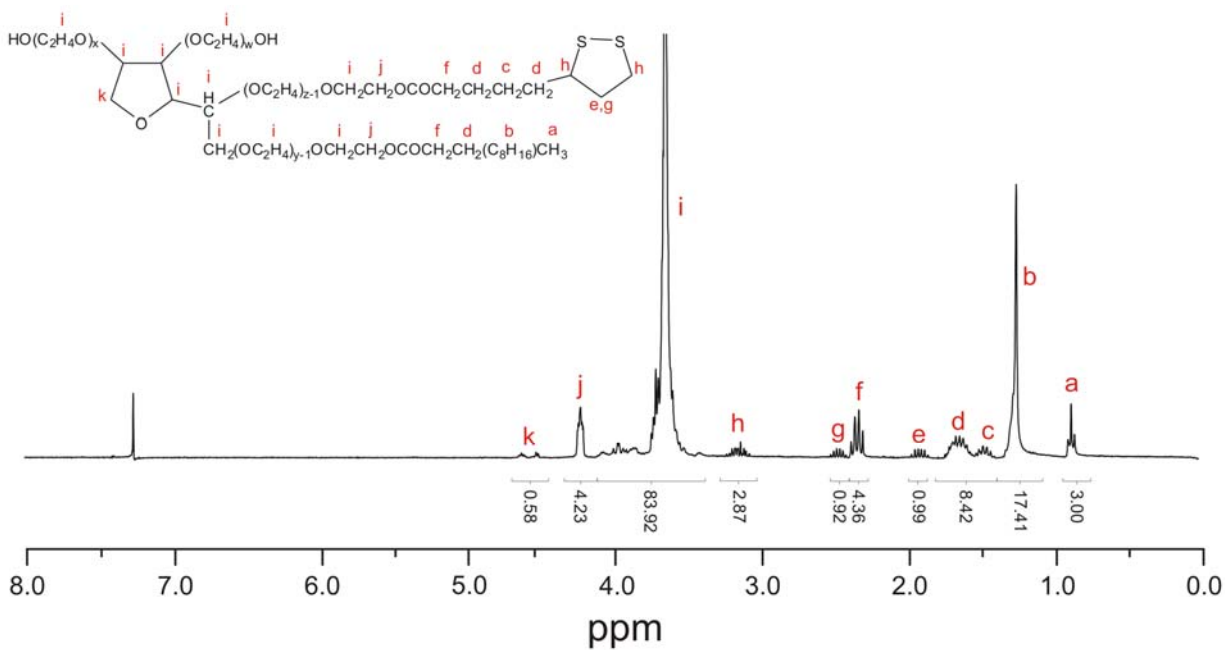


Figure B-1. ¹H-NMR of compound TD₂₀-a

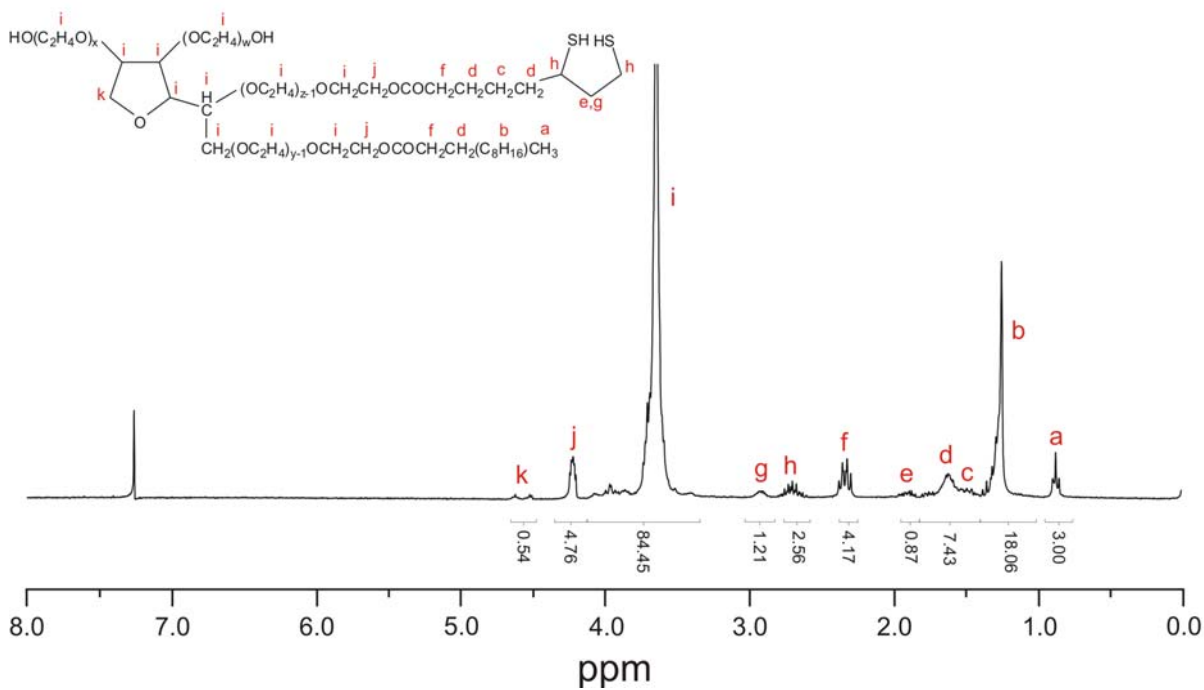


Figure B-2. ¹H-NMR of compound TD₂₀-L

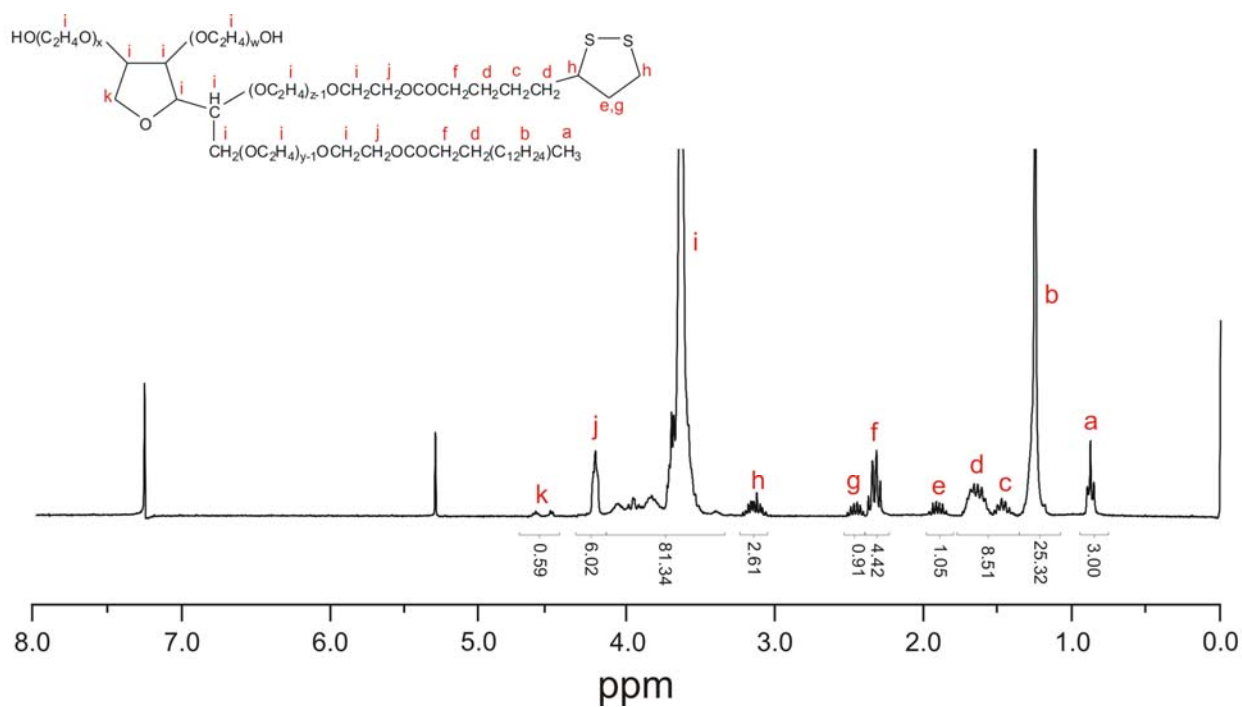


Figure B-3. $^1\text{H-NMR}$ of compound TD₄₀-a

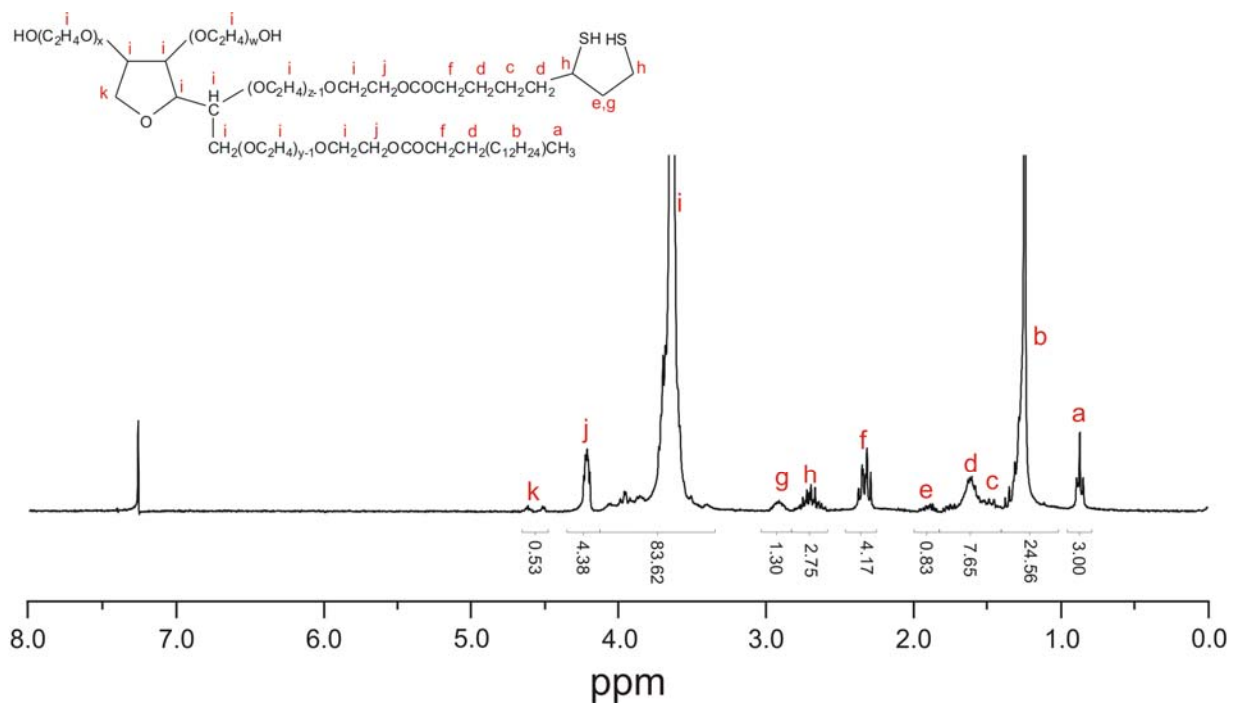


Figure B-4. $^1\text{H-NMR}$ of compound TD₄₀-L

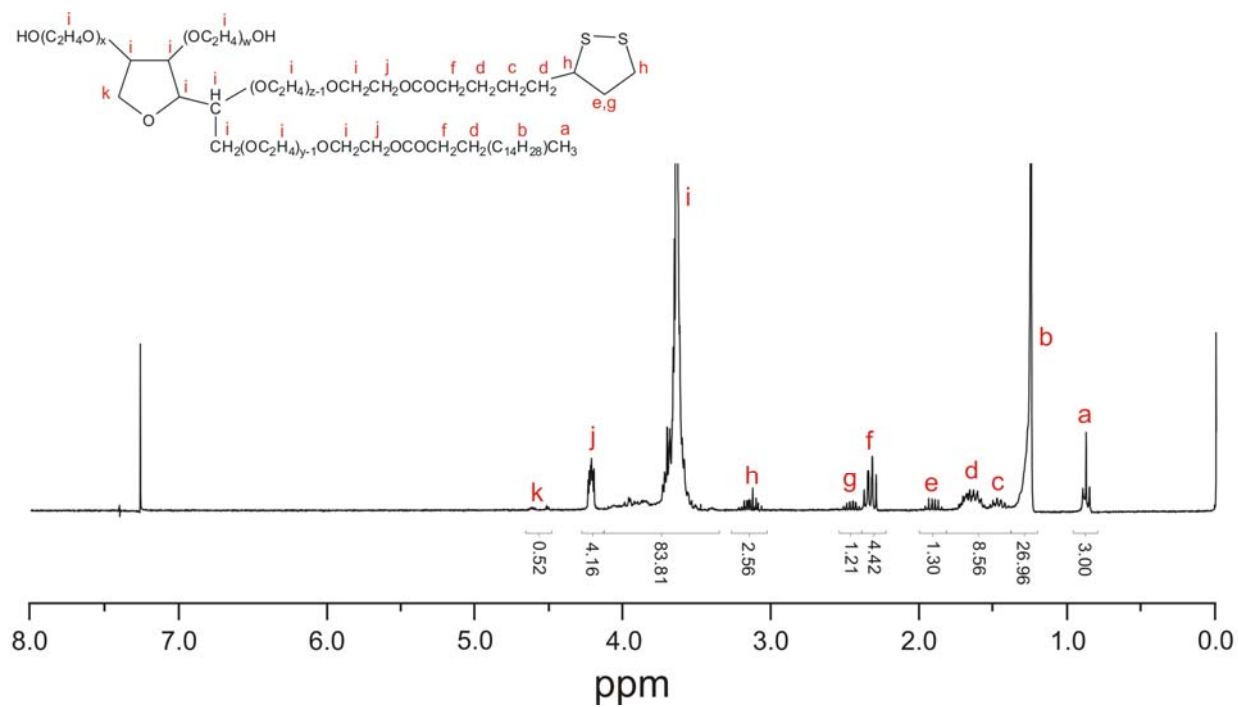


Figure B-5. ¹H-NMR of compound TD₆₀-a

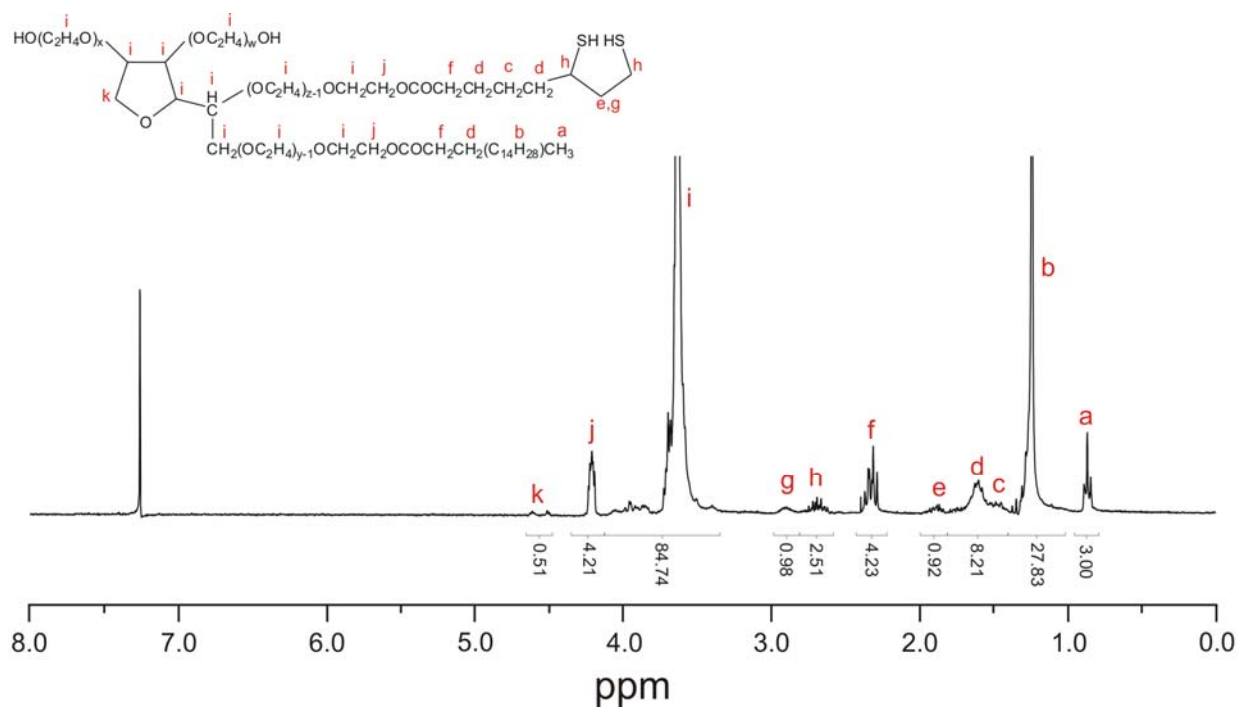


Figure B-6. ¹H-NMR of compound TD₆₀-L

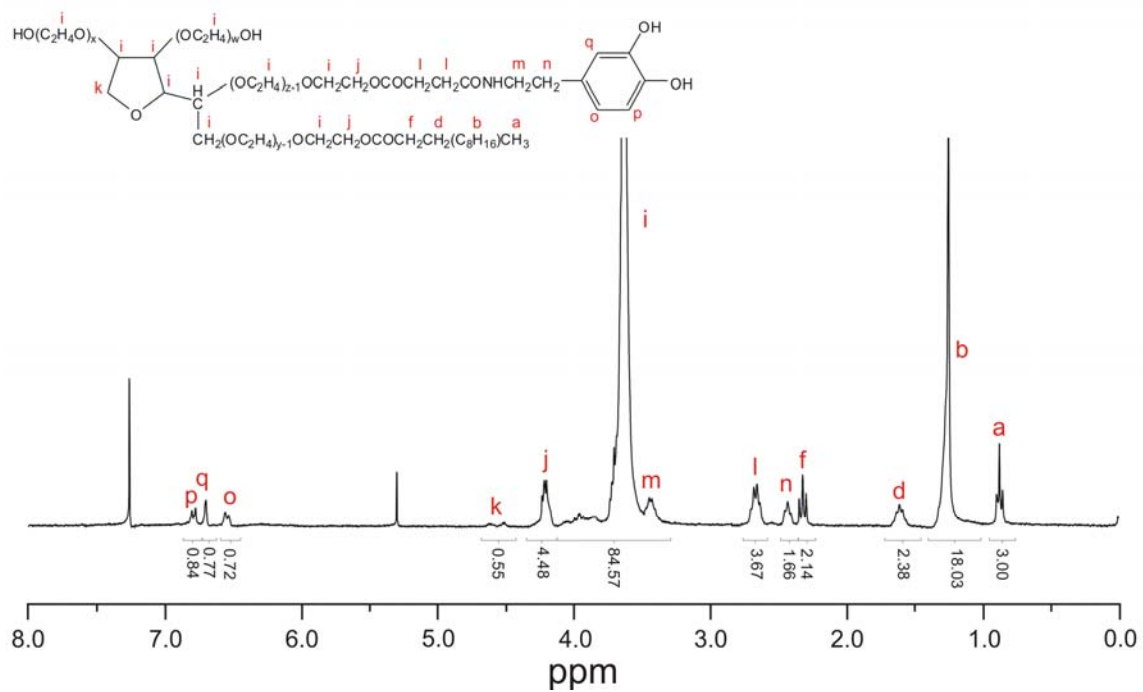


Figure B-11. ¹H-NMR of compound TD₂₀-D

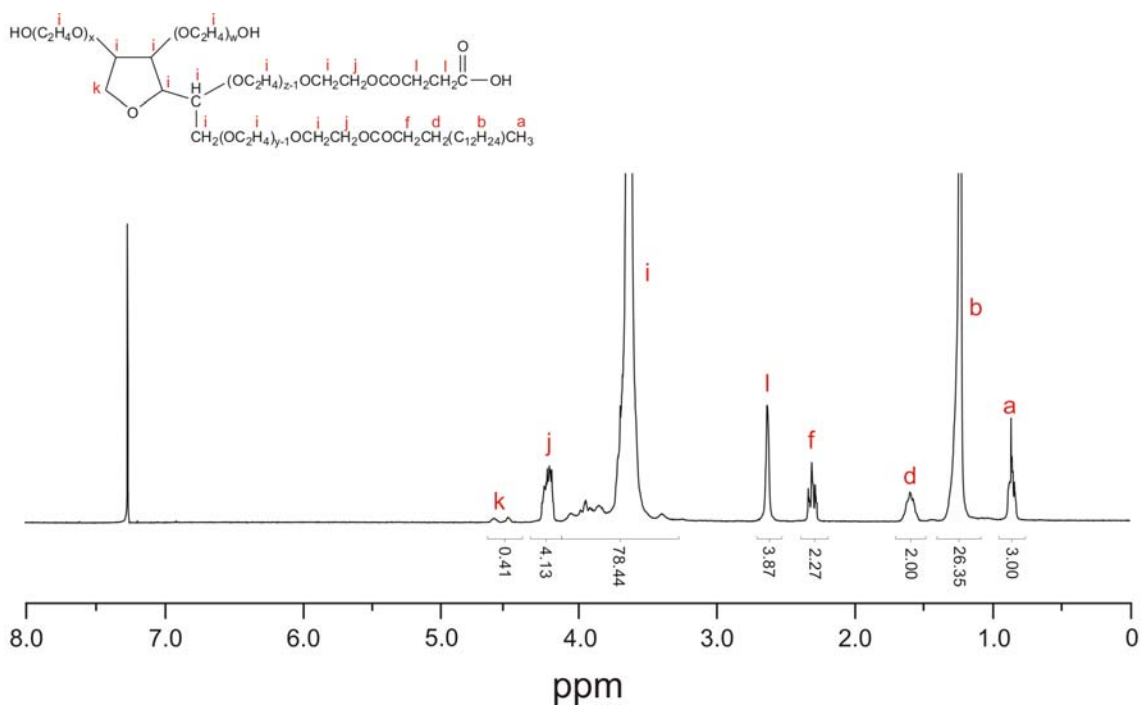


Figure B-12. ¹H-NMR of compound TD₄₀-b

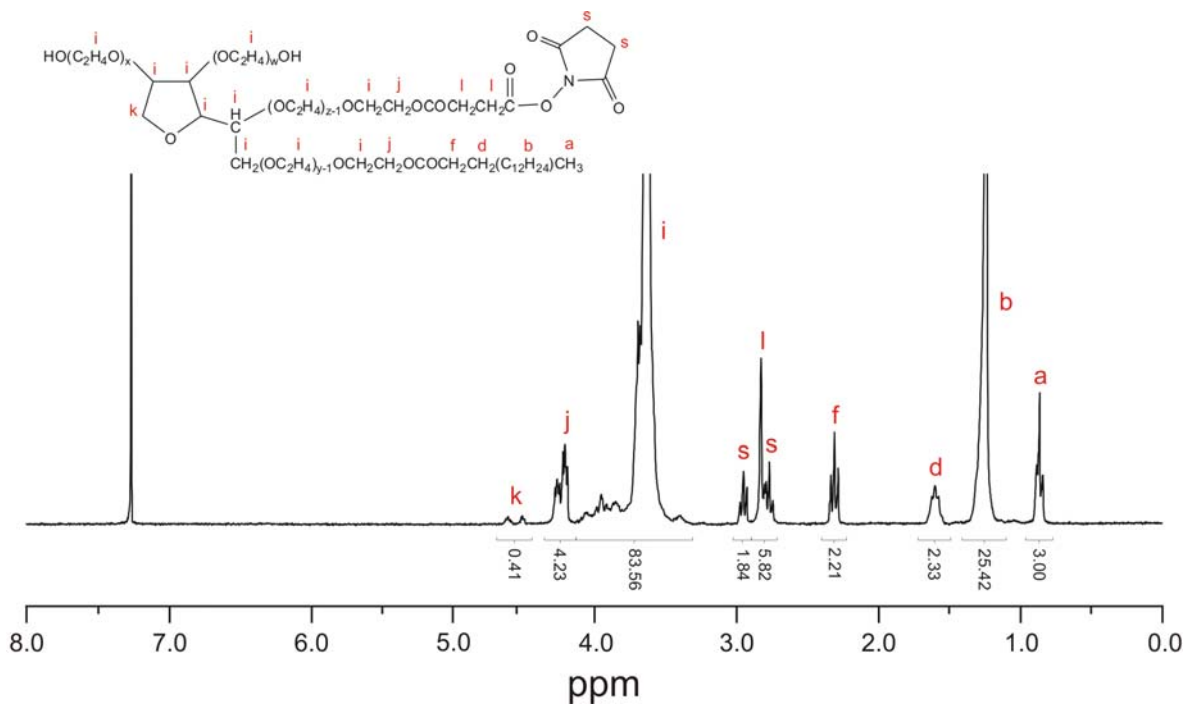


Figure B-13. ¹H-NMR of compound TD₄₀-c

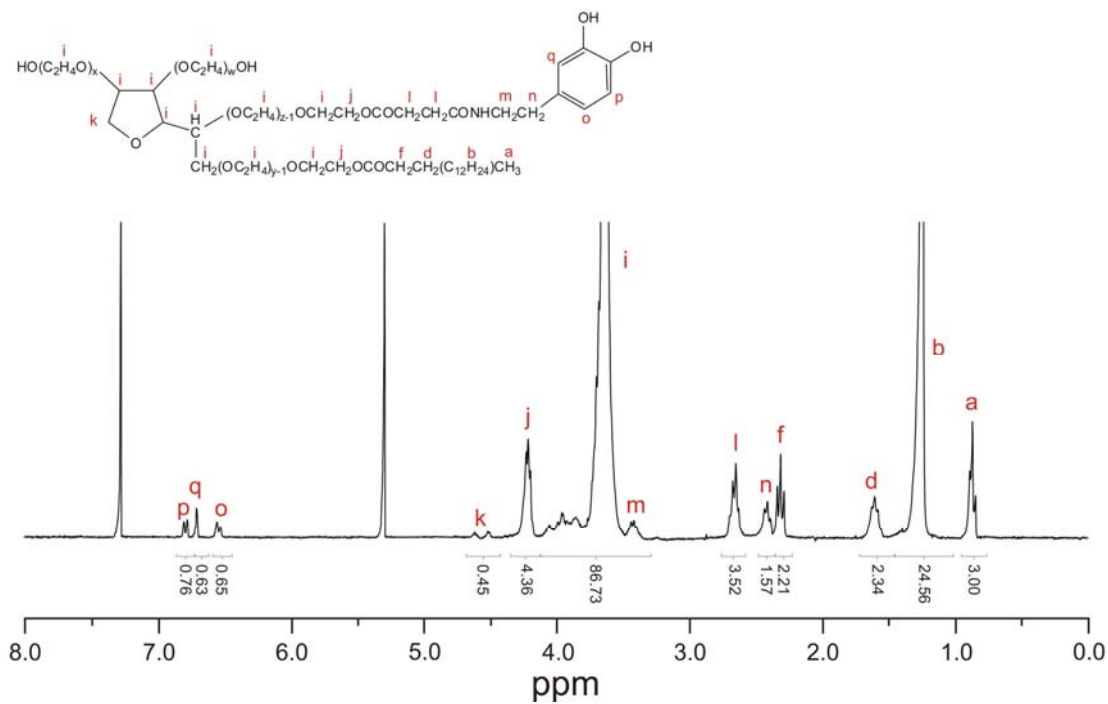


Figure B-14. ¹H-NMR of compound TD₄₀-D

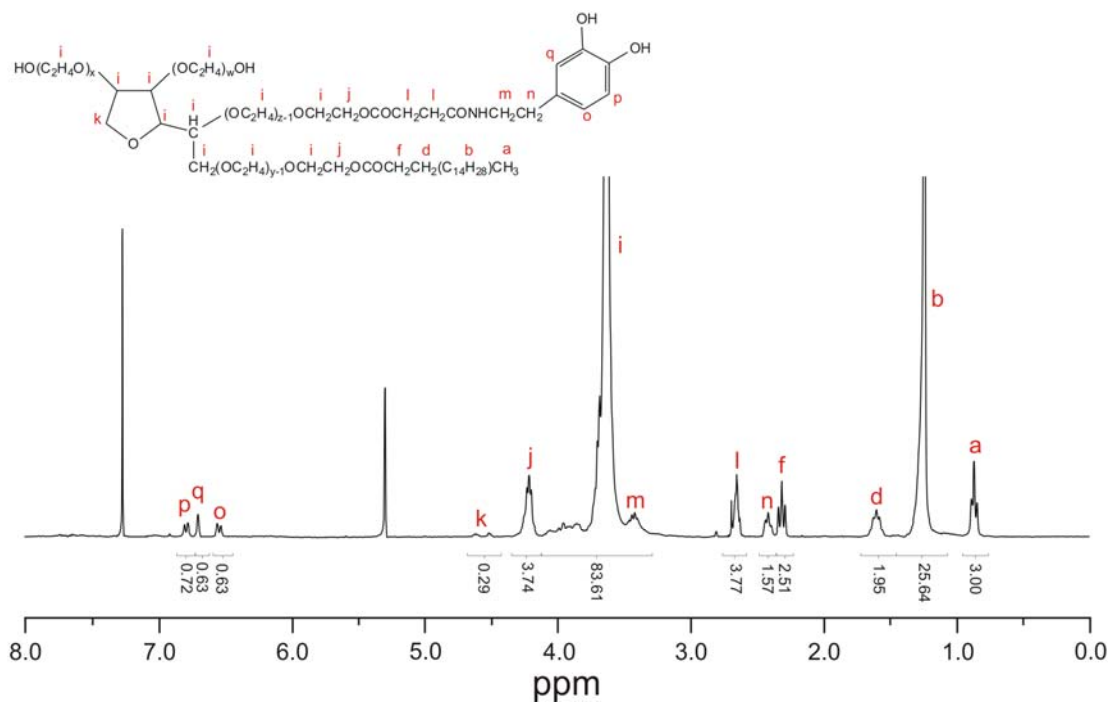


Figure B-17. ¹H-NMR of compound TD₆₀-D

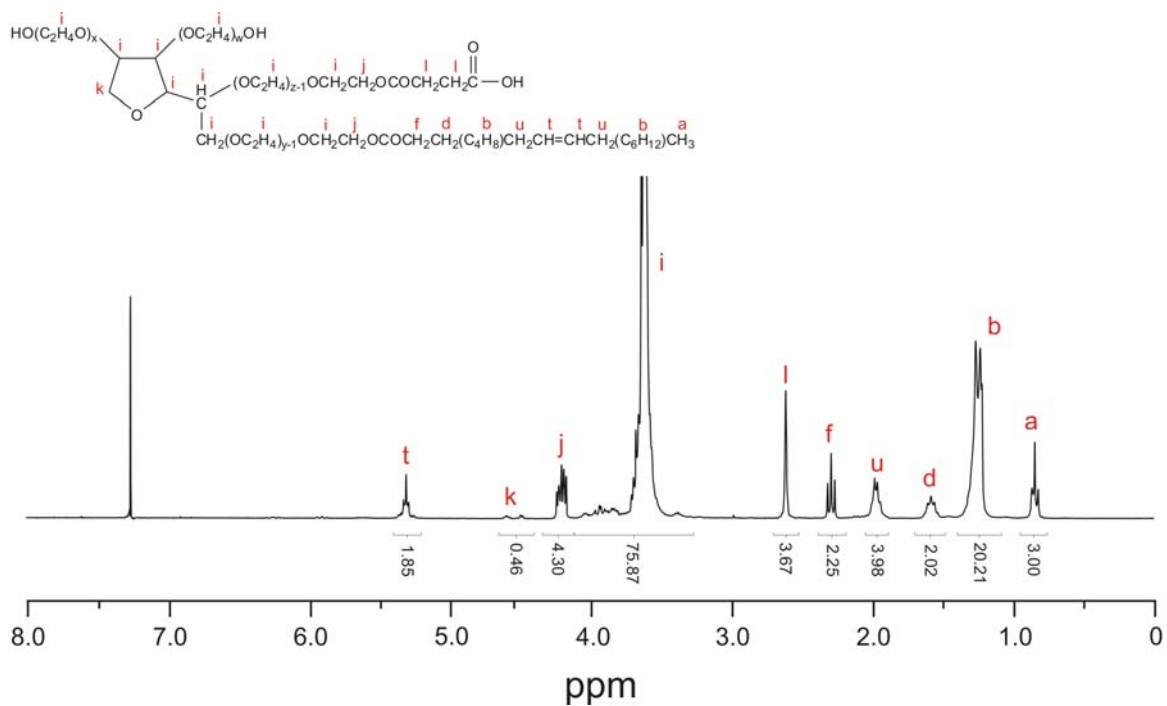


Figure B-18. ¹H-NMR of compound TD₈₀-b

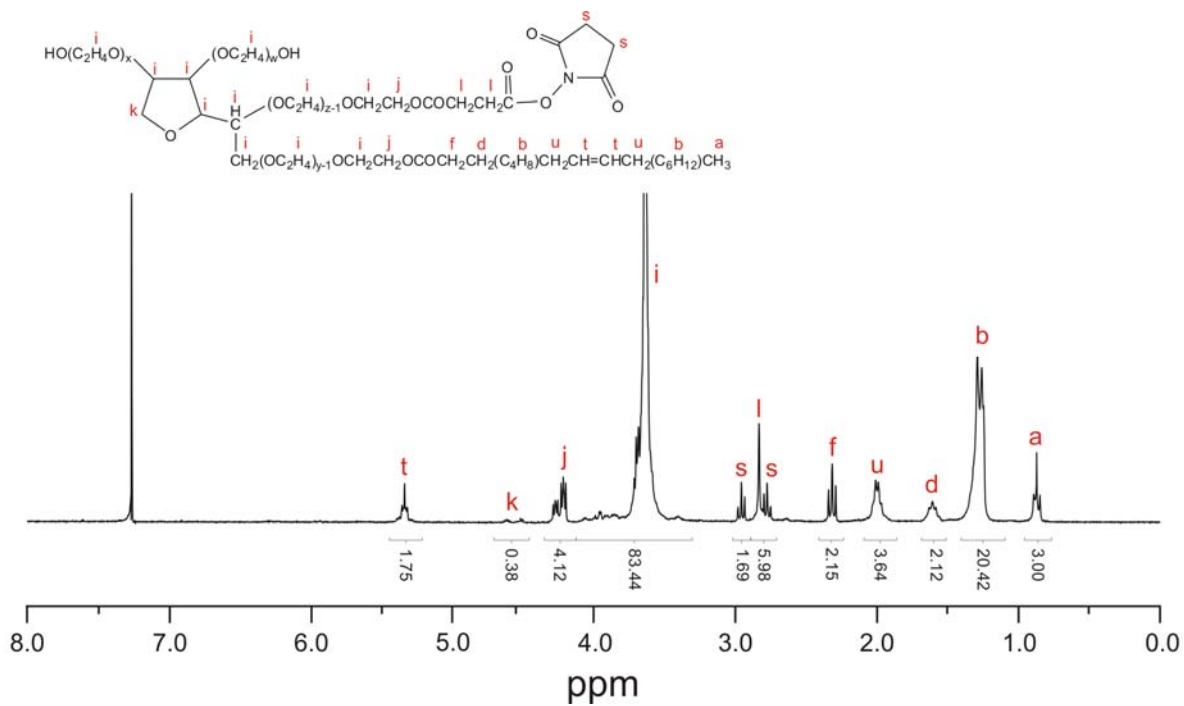


Figure B-19. ¹H-NMR of compound TD₈₀-c

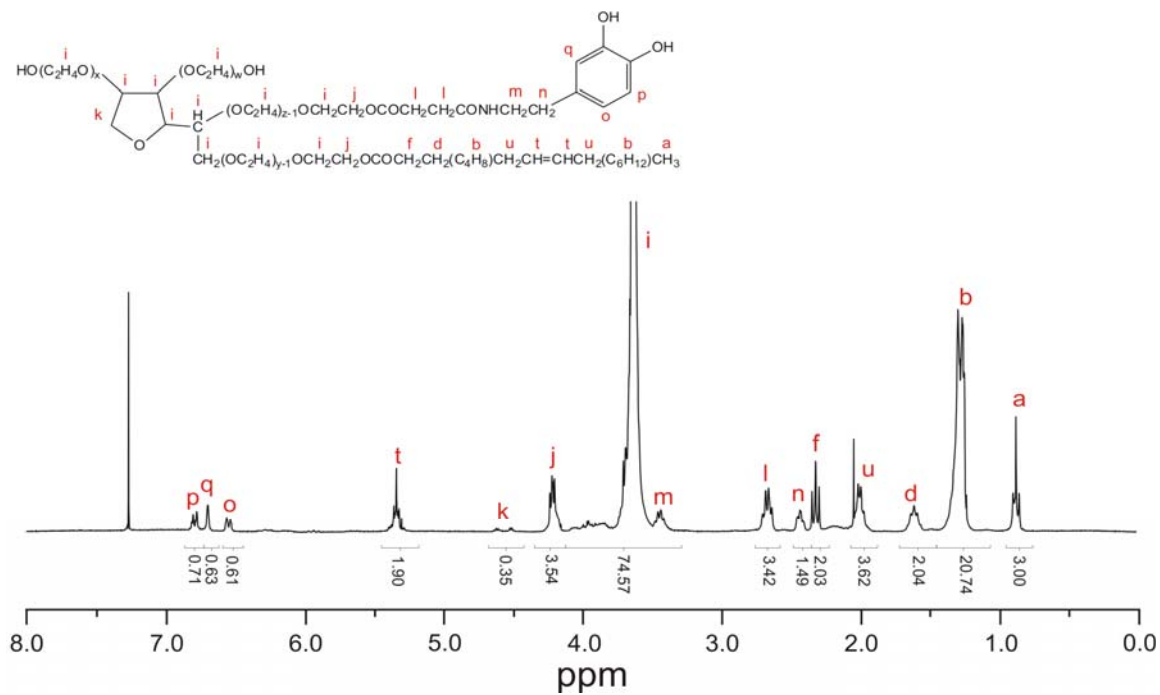


Figure B-20. ¹H-NMR of compound TD₈₀-D

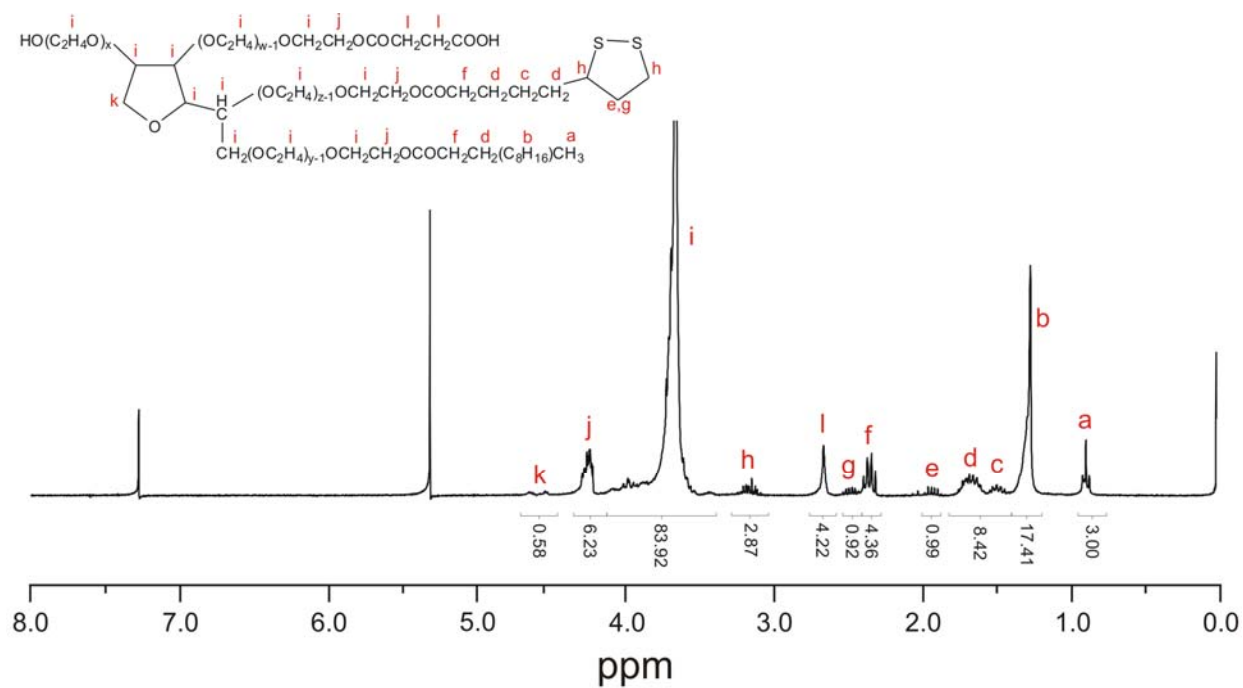


Figure B-21. ¹H-NMR of compound TD₂₀-e

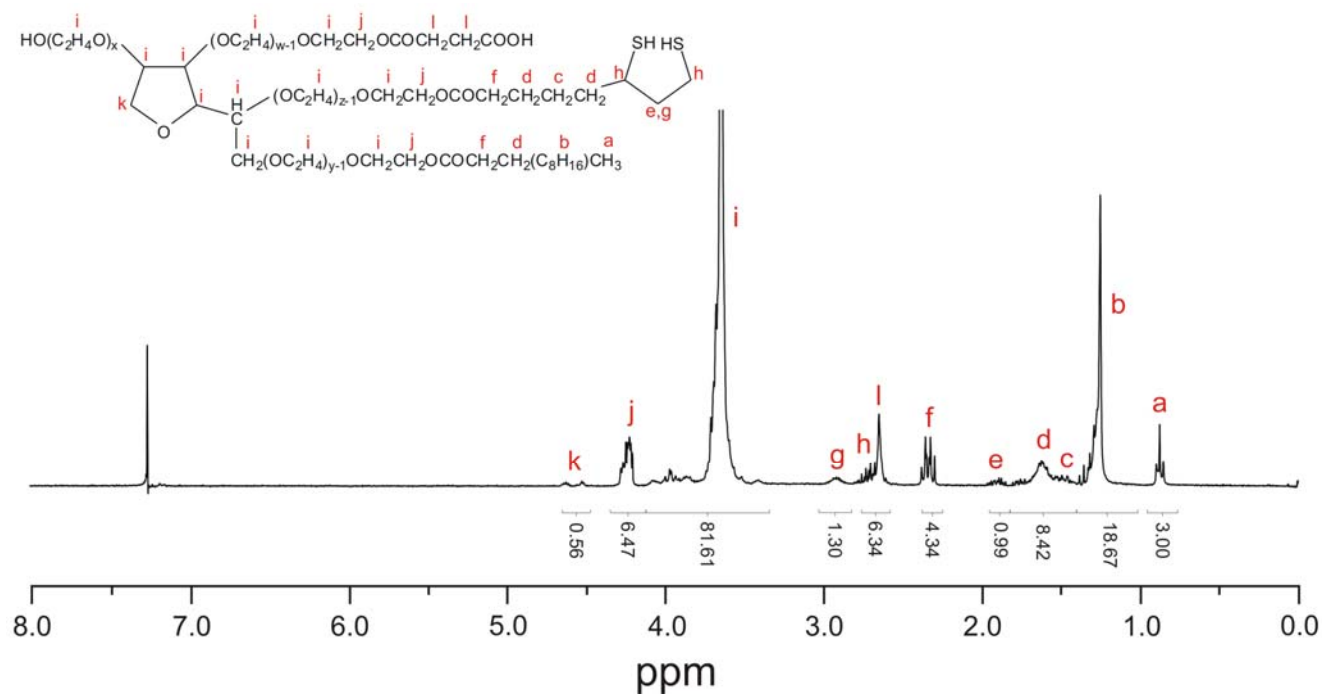
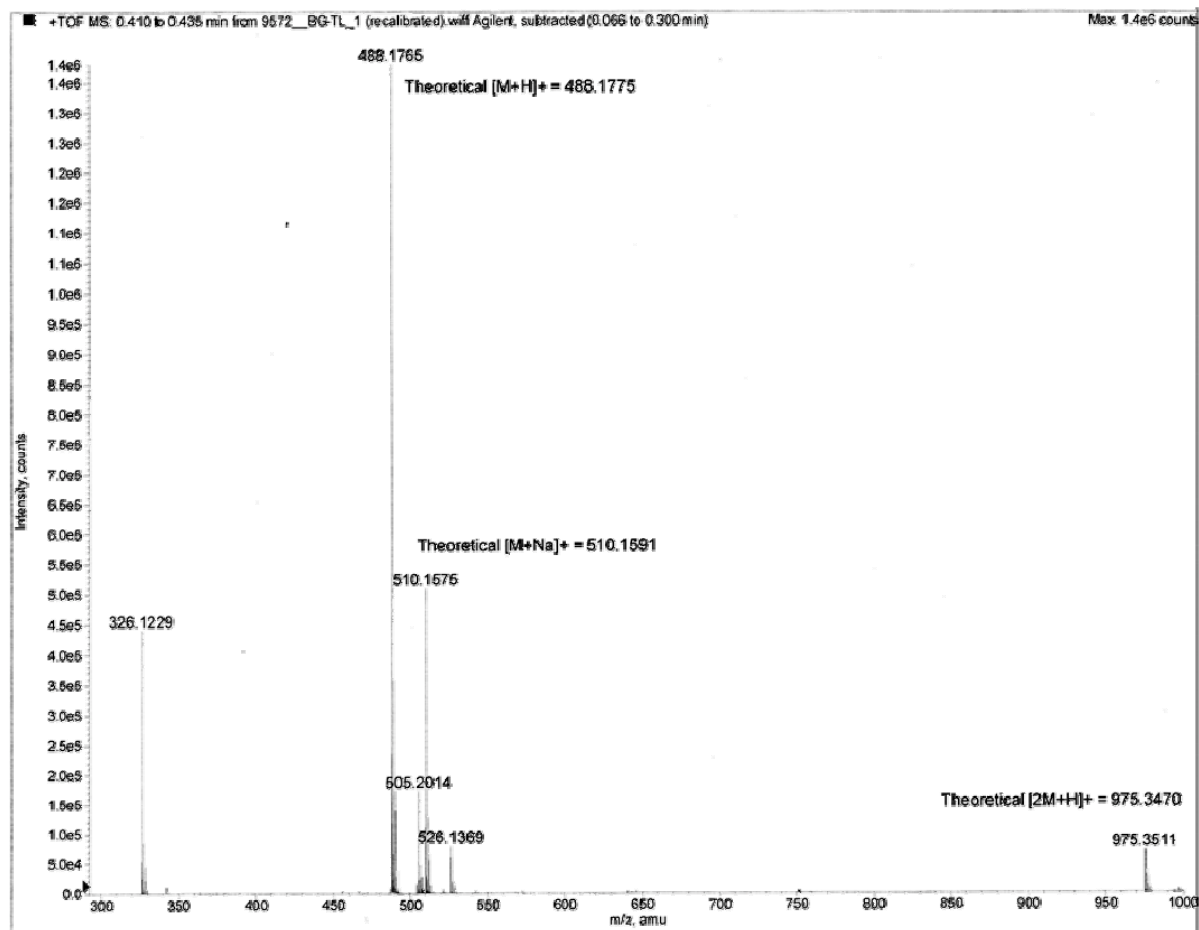


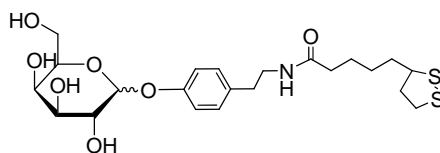
Figure B-22. ¹H-NMR of compound TD₂₀-LC

APPENDIX C
MS SPECTRUM OF LT β -GAL

A



B



Chemical Formula: C₂₂H₃₃NO₇S₂
 Exact Mass: 487.17
 Molecular Weight: 487.63
 m/z: 487.17 (100.0%), 488.17 (26.0%), 489.17 (11.0%), 489.18 (2.9%), 490.17 (2.3%)
 Elemental Analysis: C, 54.19; H, 6.82; N, 2.87; O, 22.97; S, 13.15

Figure C-1. MS spectrum of LT β -gal. (A) The MS spectrum and (B) the molecular weight of LT β -gal.

LIST OF REFERENCES

1. Alivisatos, A. P. *J. Phys. Chem.* **1996**, *100*, 13226-13239.
2. Bruchez, M.; Moronne, M.; Gin, P.; Weiss, S.; Alivisatos, A. P. *Science* **1998**, *281*, 2013-2016.
3. Elghanian, R.; Storhoff, J. J.; Mucic, R. C.; Letsinger, R. L.; Mirkin, C. A. *Science* **1997**, *277*, 1078-1081.
4. Tian, N.; Zhou, Z. Y.; Sun, S. G.; Ding, Y.; Wang, Z. L. *Science* **2007**, *316*, 732-735.
5. Ishii, D.; Kinbara, K.; Ishida, Y.; Ishii, N.; Okochi, M.; Yohda, M.; Aida, T. *Nature* **2003**, *423*, 628.
6. Wu, B.; Heidelberg, A.; Boland, J. J. *Nat Mater* **2005**, *4*, 525-529.
7. Chan, W. C. W.; Nie, S. M. *Science* **1998**, *281*, 2016-2018.
8. Larson, D. R.; Zipfel, W. R.; Williams, R. M.; Clark, S. W.; Bruchez, M. P.; Wise, F. W.; Webb, W. W. *Science* **2003**, *300*, 1434-1436.
9. Liu, G. L.; Yin, Y. D.; Kunchakarra, S.; Mukherjee, B.; Gerion, D.; Jett, S. D.; Bear, D. G.; Gray, J. W.; Alivisatos, A. P.; Lee, L. P.; Chen, F. Q. *Nat. Nanotechnol.* **2006**, *1*, 47-52.
10. Cao, Y. W. C.; Jin, R. C.; Mirkin, C. A. *Science* **2002**, *297*, 1536-1540.
11. Huynh, W. U.; Dittmer, J. J.; Alivisatos, A. P. *Science* **2002**, *295*, 2425-2427.
12. Gur, I.; Fromer, N. A.; Geier, M. L.; Alivisatos, A. P. *Science* **2005**, *310*, 462-465.
13. Gur, I.; Fromer, N. A.; Chen, C. P.; Kanaras, A. G.; Alivisatos, A. P. *Nano Lett.* **2007**, *7*, 409-414.
14. Milliron, D. J.; Hughes, S. M.; Cui, Y.; Manna, L.; Li, J. B.; Wang, L. W.; Alivisatos, A. P. *Nature* **2004**, *430*, 190-195.
15. Coe, S.; Woo, W. K.; Bawendi, M.; Bulovic, V. *Nature* **2002**, *420*, 800-803.
16. Coe-Sullivan, S.; Woo, W. K.; Steckel, J. S.; Bawendi, M.; Bulovic, V. *Org. Electron* **2003**, *4*, 123-130.
17. Anikeeva, P. O.; Halpert, J. E.; Bawendi, M. G.; Bulovic, V. *Nano Lett.* **2007**, *7*, 2196-2200.
18. Colvin, V. L.; Schlamp, M. C.; Alivisatos, A. P. *Nature* **1994**, *370*, 354-357.

19. Konya, Z.; Puentes, V. F.; Kiricsi, I.; Zhu, J.; Alivisatos, P.; Somorjai, G. A. *Catal. Lett.* **2002**, *81*, 137-140.
20. Kim, S.; Bawendi, M. G. *J. Am. Chem. Soc.* **2003**, *125*, 14652-14653.
21. Sun, S. H.; Murray, C. B.; Weller, D.; Folks, L.; Moser, A. *Science* **2000**, *287*, 1989-1992.
22. Murray, C. B.; Norris, D. J.; Bawendi, M. G. *J. Am. Chem. Soc.* **1993**, *115*, 8706-8715.
23. Teng, X. W.; Yang, H. *J. Am. Chem. Soc.* **2003**, *125*, 14559-14563.
24. S. Han, Y. Y. K. W. P. Y. E. S. T. H. *Adv. Mater.* **2003**, *15*, 1922-1925.
25. Gutsch, A.; Muhlenweg, H.; Kramer, M. *Small* **2005**, *1*, 30-46.
26. Ago, H.; Ohshima, S.; Uchida, K.; Yumura, M. *J. Phys. Chem. B* **2001**, *105*, 10453-10456.
27. Grass, R. N.; Stark, W. J. *J. Mater. Chem.* **2006**, *16*, 1825-1830.
28. Kooi, B. J.; Palasantzas, G.; De Hosson, J. T. M. *Appl. Phys. Lett.* **2006**, *89*, 161914.
29. Basak, S.; Chen, D. and Biswas, P. *Chem. Engr. Sci.*, **2007**, *62*, 1263-1268.
30. Demetrius, S.; John, D. P.; George, K.; Athos, P.; Mountziaris, T. J. *Appl. Phys. Lett.* **2002**, *80*, 4024-4026.
31. Lian, O. Y.; Thrall, E. S.; Deshmukh, M. M.; Park, H. *Adv. Mater.* **2006**, *18*, 1437-1440.
32. Dubertret, B.; Skourides, P.; Norris, D. J.; Noireaux, V.; Brivanlou, A. H.; Libchaber, A. *Science* **2002**, *298*, 1759-1762.
33. Quinlan, F. T.; Kuther, J.; Tremel, W.; Knoll, W.; Risbud, S.; Stroeve, P. *Langmuir* **2000**, *16*, 4049-4051.
34. Destre; x, e, C.; Ghijsen, J.; Nagy, J. B. *Langmuir* **2008**.
35. Chen, D. H.; Wu, S. H. *Chem. Mater.* **2000**, *12*, 1354-1360.
36. Martin, C. R. *Chem. Mater.* **1996**, *8*, 1739-1746.
37. Martin, C. R.; Kohli, P. *Nat. Rev. Drug Discov.* **2003**, *2*, 29-37.
38. Lee, S. B.; Mitchell, D. T.; Trofin, L.; Nevanen, T. K.; Soderlund, H.; Martin, C. R. *Science* **2002**, *296*, 2198-2200.
39. Puentes, V. F.; Krishnan, K. M.; Alivisatos, A. P. *Science* **2001**, *291*, 2115-2117.

40. An, K.; Lee, N.; Park, J.; Kim, S. C.; Hwang, Y.; Park, J. G.; Kim, J. Y.; Park, J. H.; Han, M. J.; Yu, J.; Hyeon, T. *J. Am. Chem. Soc.* **2006**, *128*, 9753-9760.
41. Rogach, A. L.; Nagesha, D.; Ostrander, J. W.; Giersig, M.; Kotov, N. A. *Chem. Mater.* **2000**, *12*, 2676-2685.
42. Jana, N. R.; Gearheart, L.; Murphy, C. J. *J. Phys. Chem. B* **2001**, *105*, 4065-4067.
43. Xiong, Y.; Washio, I.; Chen, J.; Cai, H.; Li, Z. Y.; Xia, Y. *Langmuir* **2006**, *22*, 8563-8570.
44. Jin, R. C.; Cao, Y. W.; Mirkin, C. A.; Kelly, K. L.; Schatz, G. C.; Zheng, J. G. *Science* **2001**, *294*, 1901-1903.
45. Tang, Z.; Kotov, N. A.; Giersig, M. *Science* **2002**, *297*, 237-240.
46. Yin, Y.; Alivisatos, A. P. *Nature* **2005**, *437*, 664-670.
47. Peng, X. G.; Manna, L.; Yang, W. D.; Wickham, J.; Scher, E.; Kadavanich, A.; Alivisatos, A. P. *Nature* **2000**, *404*, 59-61.
48. Manna, L.; Scher, E. C.; Alivisatos, A. P. *J. Am. Chem. Soc.* **2000**, *122*, 12700-12706.
49. Lamer, V. K.; Dinegar, R. H. *J. Am. Chem. Soc.* **1950**, *72*, 4847-4854.
50. Cao, Y. C.; Wang, J. H. *J. Am. Chem. Soc.* **2004**, *126*, 14336-14337.
51. Yang, Y. A.; Wu, H. M.; Williams, K. R.; Cao, Y. C. *Angew. Chem. Int. Ed.* **2005**, *44*, 6712-6715.
52. Gou, L.; Murphy, C. J. *Chem. Mater.* **2005**, *17*, 3668-3672.
53. Wagner, C. *Z Elektrochem* **1961**, *65*, 581-591.
54. Lifshitz, I. M.; Slyozov, V. V. *J. Phys. Chem. Solids* **1961**, *19*, 35-50.
55. Lorenz Ratke; Voorhees, P. W. *Growth and Coarsening: Ostwald Ripening in Materials Processing*; Springer, 2002.
56. Park, J.; An, K. J.; Hwang, Y. S.; Park, J. G.; Noh, H. J.; Kim, J. Y.; Park, J. H.; Hwang, N. M.; Hyeon, T. *Nat. Mater.* **2004**, *3*, 891-895.
57. Wang, Z. L. *J. Phys. Chem. B* **2000**, *104*, 1153-1175.
58. Cao, Y. W.; Banin, U. *J. Am. Chem. Soc.* **2000**, *122*, 9692-9702.
59. Hines, M. A.; Guyot-Sionnest, P. *J. Phys. Chem.* **1996**, *100*, 468-471.
60. Goldstein, A. N.; Echer, C. M.; Alivisatos, A. P. *Science* **1992**, *256*, 1425-1427.

61. Kubo, R. J. . *Phys. Soc. Jap.* **1962**, *17*, 975-986.
62. Kippeny, T.; Swafford, L. A.; Rosenthal, S. J. *J. Chem. Edu.* **2002**, *79*, 1094-1100.
63. Rossetti, R.; Ellison, J. L.; Gibson, J. M.; Brus, L. E. *J. Chem. Phys.* **1984**, *80*, 4464-4469.
64. Kayanuma, Y. *Phys. Rev. B* **1988**, *38*, 9797-9805.
65. Ramaniah, L. M.; Nair, S. V. *Phys. Rev. B* **1993**, *47*, 7132.
66. Sapra, S.; Sarma, D. D. *Phys. Rev. B* **2004**, *69*, 125304.
67. Viswanatha, R.; Sapra, S.; Saha-Dasgupta, T.; Sarma, D. D. *Phys. Rev. B* **2005**, *72*, 045333.
68. Bryant, G. W.; Jaskolski, W. *J. Phys. Chem. B* **2005**, *109*, 19650-19656.
69. Link, S.; El-Sayed, M. A. *J. Phys. Chem. B* **1999**, *103*, 4212-4217.
70. Huang, S.; K. Minami; H. Sakaue; Shingubara, S.; Takahagi, T. *J. Appl. Phys.* **2002**, *92*, 7486-7490.
71. Liu, X.; Atwater, M.; Wang, J.; Huo, Q. *Coll. Surf. B. Biointer.* **2007**, *58*, 3.
72. Mie, G. *Ann. Phys.* **1908**, *25*, 377.
73. Kreibig, U.; Vollmer, M. *Optical Properties of Metal Clusters*; Springer: Berlin; New York, 1995.
74. C.N.R. Rao; P.J. Thomas; Kulkarni., G. U. *Nanocrystals: synthesis, properties and applications*; Springer: Berlin; New York, 2007.
75. Johnson, P. B.; Christy, R. W. *Phys. Rev. B* **1972**, *6*, 4370.
76. Franklin Kim, S. C. H. S. T. K. P. Y. *Angew. Chem. Int. Ed.* **2004**, *43*, 3673-3677.
77. van der Zande, B. M. I.; Koper, G. J. M.; Lekkerkerker, H. N. W. *J. Phys. Chem. B* **1999**, *103*, 5754-5760.
78. Toneguzzo, P.; Acher, O.; Viau, G.; Pierrard, A.; Fievet-Vincent, F.; Fievet, F.; Rosenman, I. *Magn. IEEE Trans.* **1999**, *35*, 3469.
79. O'Handley, R. C. *Modern Magnetic Materials: Principle and Applications*; Wiley-Interscience Publication: New York, 2000.
80. Jia, X.; Chen, D.; Jiao, X.; He, T.; Wang, H.; Jiang, W. *J. Phys. Chem. C* **2008**, *112*, 911-917.

81. Song, Q.; Zhang, Z. *J. Am. Chem. Soc.* **2004**, *126*, 6164-6168.
82. Lopez, N.; Janssens, T. V. W.; Clausen, B. S.; Xu, Y.; Mavrikakis, M.; Bligaard, T.; Norskov, J. K. *J. Catal.* **2004**, *223*, 232-235.
83. Gorin, D. J.; Sherry, B. D.; Toste, F. D. *Chem. Rev.* **2008**.
84. Begum, R. A.; Chanda, N.; Ramakrishna, T. V. V.; Sharp, P. R. *J. Am. Chem. Soc.* **2005**, *127*, 13494-13495.
85. Wang, C.; Daimon, H.; Lee, Y.; Kim, J.; Sun, S. *J. Am. Chem. Soc.* **2007**, *129*, 6974-6975.
86. Kim, S. W.; Kim, S.; Tracy, J. B.; Jasanoff, A.; Bawendi, M. G. *J. Am. Chem. Soc.* **2005**, *127*, 4556-4557.
87. Tao, A. R.; Habas, S.; Yang, P. D. *Small* **2008**, *4*, 310-325.
88. Gerberich, W. W.; Mook, W. M.; Perrey, C. R.; Carter, C. B.; Baskes, M. I.; Mukherjee, R.; Gidwani, A.; Heberlein, J.; McMurry, P. H.; Girshick, S. L. *J. Mech. Phys. Solids* **2003**, *51*, 979-992.
89. Podsiadlo, P.; Kaushik, A. K.; Arruda, E. M.; Waas, A. M.; Shim, B. S.; Xu, J.; Nandivada, H.; Pumplun, B. G.; Lahann, J.; Ramamoorthy, A.; Kotov, N. A. *Science* **2007**, *318*, 80-83.
90. Mamedov, A. A.; Kotov, N. A.; Prato, M.; Guldi, D. M.; Wicksted, J. P.; Hirsch, A. *Nat. Mater.* **2002**, *1*, 190-194.
91. Alivisatos, P. *Nat. Biotechnol.* **2004**, *22*, 47-52.
92. Medintz, I. L.; Uyeda, H. T.; Goldman, E. R.; Mattoussi, H. *Nat. Mater.* **2005**, *4*, 435-446.
93. Gao, X. H.; Cui, Y. Y.; Levenson, R. M.; Chung, L. W. K.; Nie, S. M. *Nat. Biotechnol.* **2004**, *22*, 969-976.
94. Yezhlyev, M. V.; Al-Hajj, A.; Morris, C.; Marcus, A. I.; Liu, T.; Lewis, M.; Cohen, C.; Zrazhevskiy, P.; Simons, J. W.; Rogatko, A.; Nie, S.; Gao, X.; O'Regan, R. M. *Adv. Mater.* **2007**, *19*, 3146-3151.
95. Uyeda, H. T.; Medintz, I. L.; Jaiswal, J. K.; Simon, S. M.; Mattoussi, H. *J. Am. Chem. Soc.* **2005**, *127*, 3870-3878.
96. Daniel, M. C.; Astruc, D. *Chem. Rev.* **2004**, *104*, 293-346.
97. Kuwahara, Y.; Akiyama, T.; Yamada, S. *Thin Solid Films* **2001**, *393*, 273-277.
98. Nam, J. M.; Thaxton, C. S.; Mirkin, C. A. *Science* **2003**, *301*, 1884-1886.

99. Stoeva, S. I.; Lee, J. S.; Thaxton, C. S.; Mirkin, C. A. *Angew. Chem. Int. Ed.* **2006**, *45*, 3303-3306.
100. Lee, J.-S.; Han, M.; Mirkin, C. *Angew. Chem. Int. Ed.* **2007**, *46*, 4093-4096.
101. Lee, J. S.; Ulmann, P. A.; Han, M. S.; Mirkin, C. A. *Nano Lett.* **2008**, *8*, 529-533.
102. Kneipp, K.; Kneipp, H.; Itzkan, I.; Dasari, R. R.; Feld, M. S. *Chem. Rev.* **1999**, *99*, 2957-2976.
103. Liu, Q. S.; Lu, W. G.; Ma, A. H.; Tang, J. K.; Lin, J.; Fang, J. Y. *J. Am. Chem. Soc.* **2005**, *127*, 5276-5277.
104. Steigerwald, M. L. *Abstr. Pap. Am. Chem. S* **1988**, *195*, 59.
105. Steigerwald, M. L.; Brus, L. E. *Annu. Rev. Mater. Sci.* **1989**, *19*, 471-495.
106. Steigerwald, M. L.; Sprinkle, C. R. *Organometallics* **1988**, *7*, 245-246.
107. Brennan, J. G.; Siegrist, T.; Carroll, P. J.; Stuczynski, S. M.; Brus, L. E.; Steigerwald, M. L. *J. Am. Chem. Soc.* **1989**, *111*, 4141-4143.
108. Steigerwald, M. L. *Abstr. Pap. Am. Chem. S* **1991**, *201*, 438-INOR.
109. Peng, X. G.; Wickham, J.; Alivisatos, A. P. *J. Am. Chem. Soc.* **1998**, *120*, 5343-5344.
110. Peng, Z. A.; Peng, X. G. *J. Am. Chem. Soc.* **2001**, *123*, 183-184.
111. Qu, L.; Peng, Z. A.; Peng, X. *Nano Lett.* **2001**, *1*, 333-337.
112. Eychmuller, A. *J. Phys. Chem. B* **2000**, *104*, 6514-6528.
113. Peng, X.; Schlamp, M. C.; Kadavanich, A. V.; Alivisatos, A. P. *J. Am. Chem. Soc.* **1997**, *119*, 7019-7029.
114. Talapin, D. V.; Nelson, J. H.; Shevchenko, E. V.; Aloni, S.; Sadtler, B.; Alivisatos, A. P. *Nano Lett.* **2007**, *7*, 2951-2959.
115. Brust, M.; Walker, M.; Bethell, D.; Schiffrin, D. J.; Whyman, R. *J. Chem. Soc. Chem. Comm.* **1994**, 801-802.
116. Ji, X.; Song, X.; Li, J.; Bai, Y.; Yang, W.; Peng, X. *J. Am. Chem. Soc.* **2007**, *129*, 13939-13948.
117. Jana, N. R.; Peng, X. G. *J. Am. Chem. Soc.* **2003**, *125*, 14280-14281.
118. Zheng, N.; Fan, J.; Stucky, G. D. *J. Am. Chem. Soc.* **2006**, *128*, 6550-6551.
119. N. R. Jana; Gearheart, L.; Murphy, C. J. *Adv. Mater.* **2001**, *13*, 1389-1393.

120. Gole, A.; Murphy, C. J. *Chem. Mater.* **2004**, *16*, 3633-3640.
121. Yujie Xiong, J. M. Y. Y. X. *Angew. Chem. Int. Ed.* **2007**, *46*, 790-794.
122. Sun, Y.; Xia, Y. *Science* **2002**, *298*, 2176-2179.
123. Kim, F.; Connor, S.; Song, H.; Kuykendall, T.; Yang, P. D. *Angew. Chem. Int. Ed.* **2004**, *43*, 3673-3677.
124. Song, H.; Kim, F.; Connor, S.; Somorjai, G. A.; Yang, P. D. *J. Phys. Chem. B* **2005**, *109*, 188-193.
125. Tao, A.; Sinsersuksakul, P.; Yang, P. D. *Angew. Chem. Int. Ed.* **2006**, *45*, 4597-4601.
126. Sun, S. H.; Anders, S.; Thomson, T.; Baglin, J. E. E.; Toney, M. F.; Hamann, H. F.; Murray, C. B.; Terris, B. D. *J. Phys. Chem. B* **2003**, *107*, 5419-5425.
127. Peng, S.; Wang, C.; Xie, J.; Sun, S. *J. Am. Chem. Soc.* **2006**, *128*, 10676-10677.
128. Elkins, K. E.; Vedantam, T. S.; Liu, J. P.; Zeng, H.; Sun, S.; Ding, Y.; Wang, Z. L. *Nano Lett.* **2003**, *3*, 1647-1649.
129. Nashaat Nassar, M. H. *physica status solidi (a)* **2006**, *203*, 1324-1328.
130. Sun, S.; Zeng, H.; Robinson, D. B.; Raoux, S.; Rice, P. M.; Wang, S. X.; Li, G. *J. Am. Chem. Soc.* **2004**, *126*, 273-279.
131. Redl, F. X.; Black, C. T.; Papaefthymiou, G. C.; Sandstrom, R. L.; Yin, M.; Zeng, H.; Murray, C. B.; O'Brien, S. P. *J. Am. Chem. Soc.* **2004**, *126*, 14583-14599.
132. Jana, N. R.; Chen, Y.; Peng, X. *Chem. Mater.* **2004**, *16*, 3931-3935.
133. Lee, S. M.; Jun, Y. w.; Cho, S. N.; Cheon, J. *J. Am. Chem. Soc.* **2002**, *124*, 11244-11245.
134. Williams, D. B.; Carter, C. B. *Transmission Electron Microscopy* New York, 1996.
135. Bodansky, D. *Nuclear Energy: Principles, Practices and Prospects*; 2nd ed.; Springer: New York, 2004.
136. Hutchings G. J., H. C. S., Hudson I. D. Taylor S. H. *Nature* **1996**, *384*, 341-343.
137. Zhang, Z. T.; Konduru, M.; Dai, S.; Overbury, S. H. *Chem. Comm.* **2002**, 2406-2407.
138. Ruello, P.; Petot-Ervas, G.; Petot, C. *J. Am. Ceramic Soc.* **2005**, *88*, 604-611.
139. Kan, S.; Mokari, T.; Rothenberg, E.; Banin, U. *Nat. Mater.* **2003**, *2*, 155-158.
140. O'Loughlin, E. J.; Kelly, S. D.; Cook, R. E.; Csencsits, R.; Kemner, K. M. *Environ. Sci. & Tech.* **2003**, *37*, 721-727.

141. Zubarev, E. R.; Pralle, M. U.; Sone, E. D.; Stupp, S. I. *J. Am. Chem. Soc.* **2001**, *123*, 4105-4106.
142. Wu, H. M.; Yang, Y. A.; Cao, C. Y. *J. Am. Chem. Soc.* **2006**, *accepted*.
143. Steckel, J. S.; Yen, B. K. H.; Oertel, D. C.; Bawendi, M. G. *J. Am. Chem. Soc.* **2006**, *128*, 13032-13033.
144. Wu, N.; Fu, L.; Su, M.; Aslam, M.; Wong, K. C.; Dravid, V. P. *Nano Lett.* **2004**, *4*, 383-386.
145. Lu, W. G.; Liu, Q. S.; Sun, Z. Y.; He, J. B.; Ezeolu, C. D.; Fang, J. Y. *J. Am. Chem. Soc.* **2008**, *130*, 6983-6991.
146. Rosi, N. L.; Mirkin, C. A. *Chem. Rev.* **2005**, *105*, 1547-1562.
147. Alivisatos, A. P. *Nat. Biotechnol.* **2004**, *22*, 47-52.
148. Han, M.; Gao, X.; Su, J. Z.; Nie, S. *Nat. Biotechnol.* **2001**, *19*, 631-635.
149. Xu, C.; Xu, K.; Gu, H.; Zheng, R.; Liu, H.; Zhang, X.; Guo, Z.; Xu, B. *J. Am. Chem. Soc.* **2004**, *126*, 9938-9939.
150. Yu, W. W.; Chang, E.; Falkner, J. C.; Zhang, J.; Al-Somali, A. M.; Sayes, C. M.; Johns, J.; Drezek, R.; Colvin, V. L. *J. Am. Chem. Soc.* **2007**, *129*, 2871-2879.
151. Wu, H.; Zhu, H.; Zhuang, J.; Yang, S.; Liu, C.; Cao, Y. C. *Angew. Chem. Int. Ed.* **2008**, *47*, 3730-3734.
152. Li, J. J.; Wang, Y. A.; Guo, W.; Keay, J. C.; Mishima, T. D.; Johnson, M. B.; Peng, X. *J. Am. Chem. Soc.* **2003**, *125*, 12567-12575.
153. Battaglia, D.; Blackman, B.; Peng, X. *J. Am. Chem. Soc.* **2005**, *127*, 10889-10897.
154. Xie, J.; Xu, C.; Kohler, N.; Hou, Y.; Sun, S. *Adv. Mater.* **2007**, *19*, 3163-+.
155. Wu, X. Y.; Liu, H. J.; Liu, J. Q.; Haley, K. N.; Treadway, J. A.; Larson, J. P.; Ge, N. F.; Peale, F.; Bruchez, M. P. *Nat. Biotechnol.* **2003**, *21*, 452-452.
156. Eggertson, M. J.; Craig, D. B. *Biomed. Chromatography* **1999**, *13*, 516-519.
157. Tung, C. H.; Zeng, Q.; Shah, K.; Kim, D. E.; Schellingerhout, D.; Weissleder, R. *Canc. Res.* **2004**, *64*, 1579-1583.
158. Gee, K. R.; Sun, W. C.; Bhargat, M. K.; Upson, R. H.; Klaubert, D. H.; Latham, K. A.; Haugland, R. P. *Anal. Biochem.* **1999**, *273*, 41-48.
159. Chilvers, K. F.; Perry, J. D.; James, A. L.; Reed, R. H. *J. Appl. Microbiology* **2001**, *91*, 1118-1130.

160. Komatsu, T.; Kikuchi, K.; Takakusa, H.; Hanaoka, K.; Ueno, T.; Kamiya, M.; Urano, Y.; Nagano, T. *J. Am. Chem. Soc.* **2006**, *128*, 15946-15947.
161. Moats, R. A.; Fraser, S. E.; Meade, T. J. *Angew. Chem. Int. Ed.* **1997**, *36*, 726-728.
162. Urbanczyk-Pearson, L. M.; Femia, F. J.; Smith, J.; Parigi, G.; Duimstra, J. A.; Eckermann, A. L.; Luchinat, C.; Meade, T. J. *Inorg. Chem.* **2008**, *47*, 56-68.
163. Alauddin, M. M.; Louie, A. Y.; Shahinian, A.; Meade, T. J.; Conti, P. S. *Nuclear Medicine and Biology* **2003**, *30*, 261-265.
164. Lee, J. S.; Ulmann, P. A.; Han, M. S.; Mirkin, C. A. *Nano Lett.* **2008**, *8*, 529-533.
165. Daniel, M. C.; Astruc, D. *Chem. Rev.* **2004**, *104*, 293-346.
166. Lee, J. S.; Han, M. S.; Mirkin, C. A. *Angew. Chem. Int. Ed.* **2007**, *46*, 4093-4096.
167. Figuerola, A.; Fiore, A.; Di Corato, R.; Falqui, A.; Giannini, C.; Micotti, E.; Lascialfari, A.; Corti, M.; Cingolani, R.; Pellegrino, T.; Cozzoli, P. D.; Manna, L. *J. Am. Chem. Soc.* **2008**, *130*, 1477-1487.
168. Dabbousi, B. O.; Rodriguez-Viejo, J.; Mikulec, F. V.; Heine, J. R.; Mattoussi, H.; Ober, R.; Jensen, K. F.; Bawendi, M. G. *J. Phys. Chem. B* **1997**, *101*, 9463-9475.
169. Gu, H.; Zheng, R.; Zhang, X.; Xu, B. *J. Am. Chem. Soc.* **2004**, *126*, 5664-5665.
170. Gao, J.; Zhang, B.; Gao, Y.; Pan, Y.; Zhang, X.; Xu, B. *J. Am. Chem. Soc.* **2007**, *129*, 11928-11935.
171. Kwon, K. W.; Shim, M. *J. Am. Chem. Soc.* **2005**, *127*, 10269-10275.
172. Gu, H.; Yang, Z.; Gao, J.; Chang, C. K.; Xu, B. *J. Am. Chem. Soc.* **2005**, *127*, 34-35.
173. Yu, H.; Chen, M.; Rice, P. M.; Wang, S. X.; White, R. L.; Sun, S. *Nano Lett.* **2005**, *5*, 379-382.
174. Pellegrino, T.; Fiore, A.; Carlino, E.; Giannini, C.; Cozzoli, P. D.; Ciccarella, G.; Respaud, M.; Palmirotta, L.; Cingolani, R.; Manna, L. *J. Am. Chem. Soc.* **2006**, *128*, 6690-6698.
175. Randle, V. *The role of the coincidence site lattice in grain boundary engineering*; Woodhead Publishing Limited: Cambridge, UK, 1997.
176. Cozzoli, P. D.; Pellegrino, T.; Manna, L. *Chem. Soc. Rev.* **2006**, *35*, 1195-1208.
177. Zhuang, J. Q.; Wu, H. M.; Yang, Y. A.; Cao, Y. C. *J. Am. Chem. Soc.* **2007**, *129*, 14166-14167.

178. Zhuang, J. Q.; Wu, H. M.; Yang, Y. G.; Cao, Y. C. *Angew. Chem. Int. Ed.* **2008**, *47*, 2208-2212.

BIOGRAPHICAL SKETCH

Huimeng Wu received her Bachelor of Science in Macromolecular Science and Engineering from Fudan University in 1999. She worked under the direction of Prof. Yuliang Yang doing Living Free Radical Polymerization of Styrene. Then in 2003, she got her master degree in physical chemistry, from Institute of Chemistry, Chinese academy of Sciences, under the direction of Prof. Yanlin Song and Prof. Lei Jiang doing ultrahigh density data storage by scanning tunneling microscopy (STM).

In August, 2004, she moved to Gainesville, Florida and began her Ph.D. study in chemistry department at the University of Florida. She spent four years of her graduate research working with Prof. Yunwei Cao to complete her Ph.D. study. Her research area in Prof. Cao's group includes the synthesis of high-quality NCs, surface modification of NCs and also exploring the potential bio-application of NCs.